Aerodynamic modelling and performance analysis of over-the-wing propellers

A combined numerical and experimental study

E.A.P. Marcus

Technische Universiteit Delft

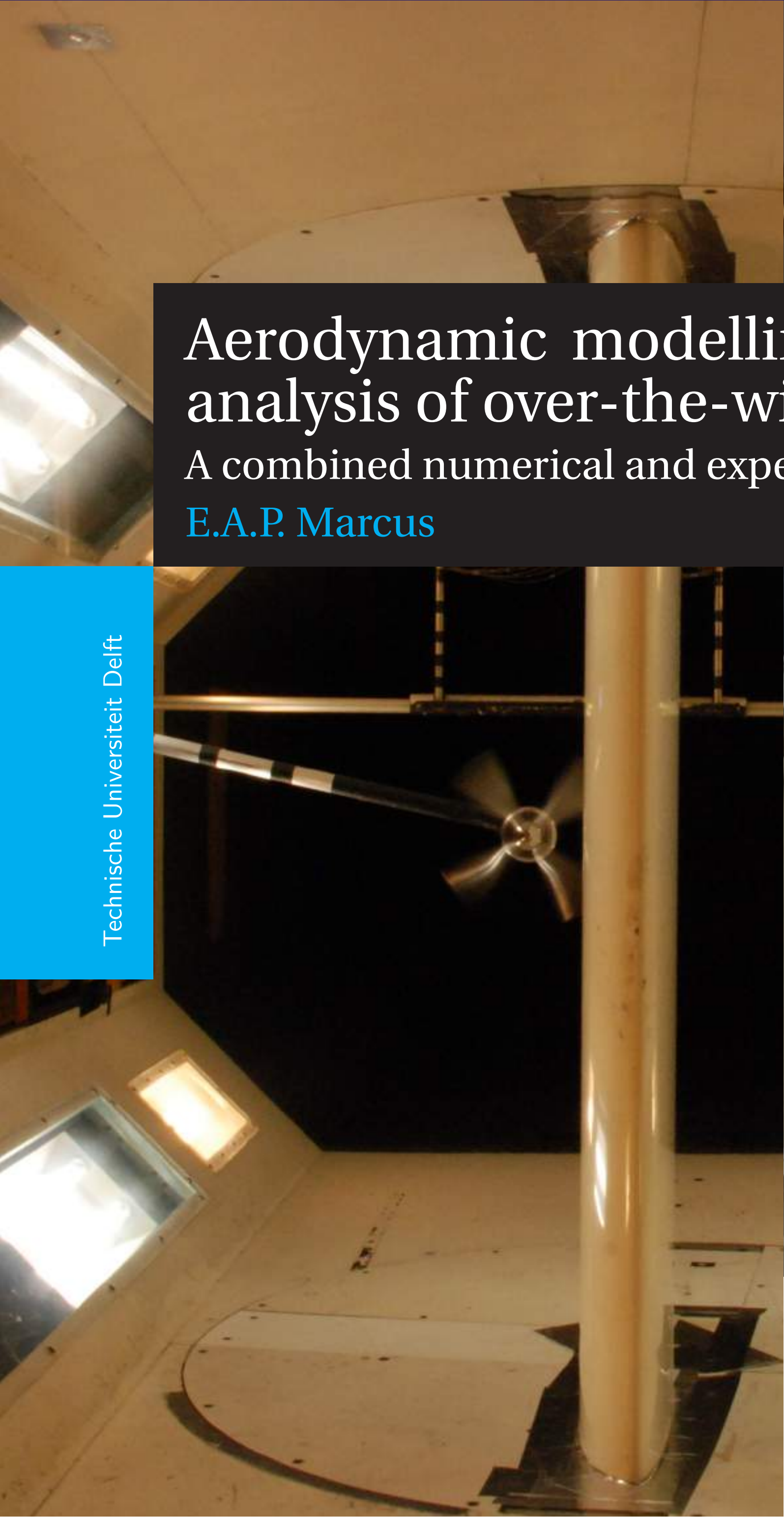

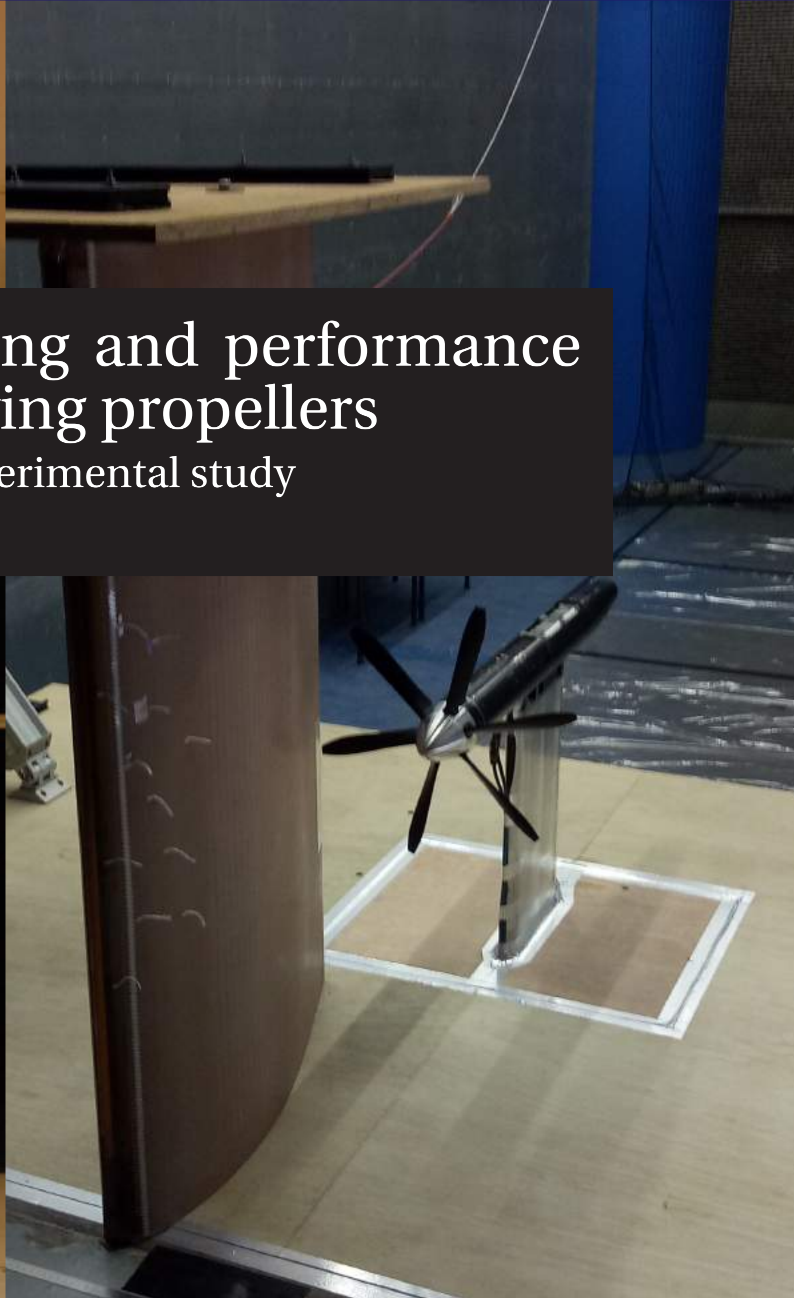

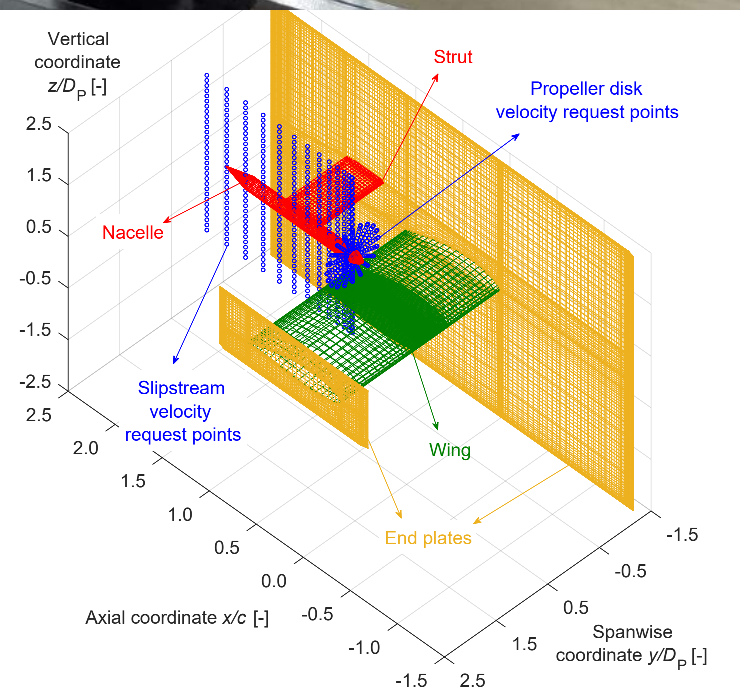

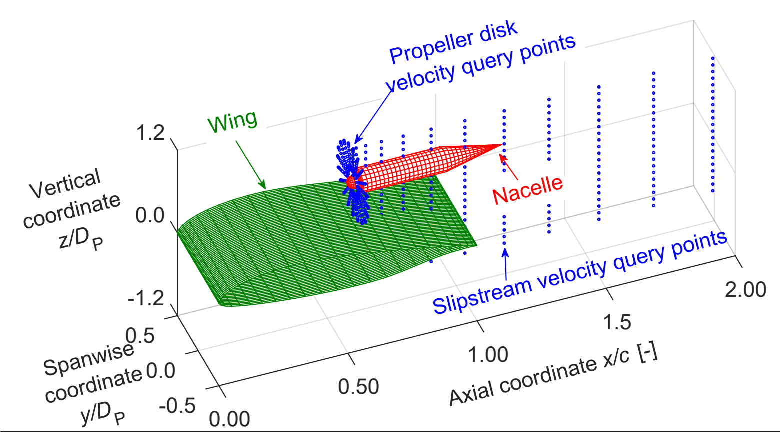

TU Delft Delft University of Technology

Challenge the future

Aerodynamic modelling and performance analysis of over-the-wing propellers

A combined numerical and experimental study

by

E.A.P. Marcus

in partial fulfillment of the requirements for the degree of

Master of Science
in Aerospace Engineering

at the Delft University of Technology.

Thesis committee:	R. de Vries M. Sc.	TU Delft, supervisor
	Prof. dr. ir. L. L. M. Veldhuis	TU Delft
	Prof. dr. ing. G. Eitelberg	TU Delft
	Dr. S. J. Hulshoff	TU Delft

Delft University of Technology

PREFACE

It is with great joy that I present this thesis to you, which I view as the crowning achievement of my studies. I think it reflects well how much I've learned during my three years in Utrecht, my board year at my student sailing organisation and my two and a half years in Delft. In terms of technical knowledge, analytical attitude, communicative skills, creativity and confidence, I have grown as a person and as a scientist, of which I am very proud.

This project was the most gargantuan I have faced so far. At the start, besides excitement, I also felt considerable uncertainty, since I felt my knowledge was limited and it would be difficult to successfully accomplish. This was all the more true because the topic was very complex and little researched. Now however, I am glad that I accepted the challenge head-first, and am very pleased with the result.

A work such as this is inconceivable to finish alone, and I would like to express my gratitude to a bunch of people. First of all my supervisor Reynard, who taught me a great deal about wind tunnels and patience. I am glad that you made so much time to discuss my work and to give me feedback and that you kept reminding me that the devil is in the details. You are already amazing at supervising, and this thesis could not have been finished like this without you!

Secondly, Akshay, who helped tirelessly during both wind tunnel campaigns and provided a lot of feedback on the conference paper we wrote. And also Tomas and Biagio, without whom we would have never managed to set up the second wind tunnel experiment and process its results. Then I would like to thank Leo Veldhuis, Georg and everyone else at the propeller meetings. Discussions (whether related to my work or not) have often been interesting and insightful, sparking my creativity and Leo gave helpful feedback on the conference paper. Furthermore, I want to thank Leo Molenwijk and Stefan for their endless help during the first wind tunnel experiment. And all wind tunnel technicians who helped during the second one. Additionally, I want to thank Jan and Arash for providing their higher-fidelity numerical results.

I would like to thank Sanne, who was never tired of reminding me that I should not work too hard, and that it's acceptable to take a break every now and then. I also want to thank my mother, for loving me unconditionally, my father, for being proud and my little brother for always being relaxed to hang out with. Finally, there have been a great deal of people who were always supportive and interested, including the ManCie, Op Dreef, my other friends, my grandmothers and the rest of my family.

I would like to dedicate this thesis to the memory of my grandfather, who graduated from what was then the TH Delft. He became an aerospace engineer more than half a century ago, and I follow in his footsteps. To anyone reading this, I hope it is of added value to your research. Or, if you're reading it for other reasons, that it is as interesting to you as it was to me. Enjoy and remember that fulfilment is part of the journey, and not only the destination.

Summary

To reduce fuel consumption, emissions and noise, the use of hybrid-electric powertrains in combination with distributed propellers in an over-the-wing configuration has been identified as a promising concept. Such a configuration has the potential to increase wing lift-to-drag ratio and high-lift capabilities, and to reduce flyover noise. For distributed propulsion concepts, it is important to quantify these effects in the early phases of the design process. However, research on the aerodynamic interaction effects of over-the-wing propellers has been limited so far. This makes the prediction of performance of such configurations difficult. Accordingly, the research objective is to analyze the aerodynamic interaction effects and quantify the performance of over-the-wing propeller systems. To achieve this objective, two wind tunnel experiments have been performed to characterize the most important aerodynamic interaction effects of a single propeller installed over-the-wing. Based on the findings, a low-fidelity numerical model was developed.

In the first wind tunnel campaign a single propeller is installed above a wing with a fowler flap. Results include surface pressure measurements on the wing and total pressure measurements in a downstream wake plane. Cruise and high-lift configurations are tested, in which the flap is retracted and deflected, respectively. The second experimental setup features an over-the-wing propeller with a rotating shaft balance, thus allowing detailed measurements of propeller thrust, torque and efficiency. In both experiments, various chordwise propeller positions are studied.

Preliminary experimental results indicated that inflow to the propeller disk was strongly non-uniform, and that the effect on the wing was mainly of potential nature. To address these findings, the numerical method couples a blade element model for the propeller, adapted for non-uniform inflow, a panel method for the wing and a vortex lattice method for the slipstream. As opposed to earlier slipstream models, wing-induced movement and deformation of the slipstream and non-uniform propeller loading effects are incorporated.

Experimental results show that the propeller decreased the wing's pressure in front of the propeller disk and increased the pressure behind it. The pressure changes increased lift and decreased pressure drag. The strength of these effects increased with increasing advance ratio, and reversed in the case of windmilling. Moreover, the nacelle was found to significantly decrease and increase lift and pressure drag, respectively. Infrared images showed that the propeller only had minor effects on wing boundary layer transition if it was installed close to the transition location. The propeller delayed or promoted transition if it was positioned slightly downstream or upstream, respectively, of the transition location.

The most important effects on the propeller are numerically shown to be a strong vertical velocity gradient for a mid-wing axial propeller position and inflow with a downward vertical component for an aft-wing axial propeller position. Both decreased thrust, torque and propulsive efficiency, although more so for mid-wing positions. The altered inflow also leads to the generation of significant side and normal forces on the propeller in mid- and aft-wing positions, respectively. The strength of effects of the wing on the propeller increased with increasing advance ratio.

The numerical tool showed that it is capable to capture the changes in the wing pressure distribution, and wing and propeller performance parameters accurately enough for the aircraft conceptual design phase. However, the effect on the wing pressure distribution is over- and underestimated for aft- and mid-wing positions respectively. Furthermore, the effect on the propeller is overestimated at low advance ratio. The tool is currently limited to cruise configurations.

To demonstrate the capabilities of the numerical tool, sensitivity analyses on the effect of axial propeller position and diameter are performed. All results show that a propeller located near 85% of the wing chord is very promising, since it significantly increases lift, and leads to small pressure drag and propulsive efficiency penalties. In the first experiment's cruise configuration, this position leads to a pressure drag increase of 2 counts, while wing lift is increased by 8%. In the first experiment's high-lift configuration, pressure drag is reduced by 3 counts, whereas lift is improved by 3%. In the second experimental setup, propeller thrust and efficiency losses in this position are 1.5% and 5.7% at the advance ratio corresponding to maximum efficiency. Additionally, at this axial location the system efficiency is maximal and it is possible to attach the propeller to the flap, allowing thrust vectoring during the aircraft's climb phase.

Besides enhancing the understanding of the experimental results, the low computational cost of the numerical model make it very suitable for design-space exploration of over-the-wing propeller configurations. It provides the wing pressure and propeller disk loading distributions, wing lift, pressure drag and pitching moment coefficients and three-component propeller forces and moments. This makes it invaluable in the conceptual design phase of over-the-wing propeller aircraft.

Contents

List of Figures

List of Tables

Nomenclature

Latin symbols

a	Axial acceleration factor at the propeller disk [-]
b	Tangential acceleration factor [-]
c	Wing chord length [m]
c_b	Blade element chord length [m]
C_{D_p}	Wing pressure drag coefficient, $\frac{D_\mathrm{press}}{\frac{1}{2}\rho_\infty V_\infty^2 S_\mathrm{ref}}$ [-]
c_l	Sectional lift coefficient [-]
C_L	Wing lift coefficient, $\frac{L}{\frac{1}{2}\rho_\infty V_\infty^2 S_\mathrm{ref}}$ [-]
c_{l_α}	Airfoil lift gradient w.r.t. angle of attack, $\frac{\partial c_l}{\partial \alpha}$ [-]
$C_{m_{c/4}}$	Wing quarter-chord pitching moment coefficient, $\frac{M_\mathrm{p}}{\frac{1}{2}\rho_\infty V_\infty^2 c S_\mathrm{ref}}$ [-]
C_N	Propeller normal force coefficient, $\frac{N}{\rho_\infty n^2 D_\mathrm{P}^4}$ [-]
C_p	Pressure coefficient, $\frac{p-p_\infty}{\frac{1}{2}\rho_\infty V_\infty^2}$ [-]
C_{p_t}	Total pressure coefficient, $\frac{p_\mathrm{t}-p_\infty}{\frac{1}{2}\rho_\infty V_\infty^2}$ [-]
C_Q	Propeller torque coefficient, $\frac{Q}{\rho_\infty n^2 D_\mathrm{P}^5}$ [-]
C_SB	Solid blockage coefficient, $(1+1.1\frac{\beta_1}{t/c})\frac{\Lambda\sigma_\mathrm{WT}}{\beta_1^3}$ [-]
C_SC	Streamline curvature coefficient, $\frac{\sigma_\mathrm{WT}}{\beta^2}$ [-]
C_T	Propeller thrust coefficient, $\frac{T}{\rho_\infty n^2 D_\mathrm{P}^4}$ [-]
C_WB	Wake blockage coefficient, $\frac{c}{4h\beta_1^2}C'_{D_p}(1+0.4M)$ [-]
C_Y	Propeller side force coefficient, $\frac{Y}{\rho_\infty n^2 D_\mathrm{P}^4}$ [-]
d	Clearance between propeller and wing [m]
d_p	Pressure drag on airfoil panel [N]
$\vec{dl}$	Direction vector of a vortex segment
D_p	Wing pressure drag [N]
D_P	Propeller diameter [m]
f	Prandtl blade end loss correction factor [-]
$\vec{g}$	Coordinate vector
$\vec{g}_\mathrm{b}$	Vector between bound vortex segment and $\vec{g}$
$\vec{g}_\mathrm{t}$	Vector between trailing vortex segment and $\vec{g}$
h	Effective wind tunnel width, i.e. wind tunnel area divided by model span [m]
J	Advance ratio, $\frac{U_\infty}{nD_\mathrm{p}}$ [-]
l_p	Lift force on airfoil panel [N]
L	Wing lift [N]
M	Mach number [-]
M_p	Quarter-chord pitching moment [N m]

LATIN SYMBOLS (CONTINUED)

M_{DD}	Drag divergence Mach number [-]
m_p	Quarter-chord pitching moment on airfoil panel [N m]
n	Propeller rotational speed [Hz]
n_{meas}	Number of measurements [-]
n_r	Number of radial disk elements [-]
n_{s}	Number of wing panels along airfoil [-]
n_y	Number of spanwise wing panels [-]
n_x	Number of axial slipstream elements [-]
n_θ	Number of azimuthal disk elements [-]
N	Propeller normal force [N]
p	Static pressure [Pa]
p_{t}	Total pressure [Pa]
P	Propeller power [W]
Q	Propeller torque [N]
r	Propeller radial coordinate [m]
R	Propeller blade radius [m]
Re	Reynolds number [-]
R_{hub}	Propeller hub radius [m]
s	Slipstream acceleration factor [-]
S_{ref}	Wing reference area, $c \cdot D_{\text{P}}$ [m^2]
t	Time [s]
	or wing thickness [m]
	or propeller blade thickness [m]
T	Propeller thrust [N]
T_C^*	Thrust coefficient, $\frac{T}{\frac{1}{2}\rho_\infty U_\infty^2 S_{\text{ref}}}$ [-]
$T_{C_{\text{DY}}}$	De Young's thrust coefficient, $\frac{8C_T}{\pi J^2}$ [-]
u	Axial induced velocity [m/s]
U	Axial velocity [m/s]
v	Spanwise induced velocity [m/s]
V	Velocity magnitude [m/s]
V_{a}	Axial blade element velocity [m/s]
V_{t}	Tangential blade element velocity [m/s]
w	Vertical induced velocity [m/s]
x	Axial coordinate [m]
x_{p}	Airfoil panel axial coordinate [m]
y	Spanwise coordinate [m]
Y	Propeller side force [N]
z	Vertical coordinate [m]

GREEK SYMBOLS

$\Delta(\;)$	Increase w.r.t. propeller-off conditions [-]
	or increase w.r.t. isolated propeller [-]
	or increase w.r.t. previous time step [-]
$\delta(\;)$	Increase w.r.t. isolated wing [-]
α	Angle of attack [deg]
β	Blade pitch angle [deg]
β_1	Mach number correction, $\sqrt{1-M^2}$ [-]
β_{75}	Blade pitch angle at 75% of the propeller radius [deg]
γ	Heat capacity ratio [-]
ϵ	Overall convergence tolerance value [-]
Γ	Circulation [$\mathrm{m^2/s}$]
δ	Flap deflection angle [deg]
η	Propeller efficiency [-]
η_{system}	Propulsive efficiency of the wing-propeller-nacelle system [-]
θ	Propeller azimuthal coordinate [rad]
κ	Airfoil shape factor related to drag divergence [rad]
Λ	Wing body-shape factor, $\frac{16}{\pi}\int_0^1 \frac{z}{c}\sqrt{(1-C_p)\left(1+(\frac{\mathrm{d}z}{\mathrm{d}x})^2\right)}\mathrm{d}\frac{x}{c}$ [-]
ρ	Density [$\mathrm{kg/m^3}$]
$\sigma(\;)$	Uncertainty [-]
σ_{e}	Effective blade solidity, $0.0356B\frac{\bar{c}_{\mathrm{b}}}{R}c_{\bar{l}_\alpha}$ [-]
σ_{WT}	Ratio between wing chord and wind tunnel height, $\frac{\pi^2 c^2}{48h^2}$ [-]
τ	Slipstream centerline angle w.r.t. freestream [deg]
τ_{s}	Fully developed slipstream centerline angle w.r.t. freestream [deg]
φ	Angle between x-axis and airfoil panel [deg]
Ω	Propeller rotational speed [rad/s]

ADDITIONAL SUB- AND SUPERSCRIPTS

‘	Uncorrected value
*	Value after previous iteration
-	Mean value
0	Propeller disk location
∞	Freestream conditions
b	Bound
eff	Effective
fit	Fitted
i	Induced
iso	Isolated
meas	Measured
P	Propeller
pot	Potential
prop. on	Propeller-on conditions
prop. off	Propeller-off conditions
ss	Slipstream
t	Trailing
tr	Boundary-layer transition
w	Wing

ABBREVIATIONS

BEM	Blade element method
VLM	Vortex lattice model

I

Background

1

INTRODUCTION

Future aviation challenges are foreseen to be mainly related to emissions, noise, fuel burn and field length [1, 2]. To meet targets set by NASA [3] and the European Commission [4], radically new aircraft designs are necessary. Hybrid-electric propulsion has received increased attention in light of reduced emission requirements [5–7], since it allows a more efficient energy conversion and transmission. Contrary to thermal engines, hybrid-electric propulsion allows an engine's size to be reduced without significantly reducing efficiency. This makes it possible to distribute thrust over a large number of engines, which is known as distributed propulsion. Provided that the engines are non-thermal, distributed propulsion configurations increase propulsive efficiency, since the effective bypass ratio increases [8]. Additionally the propulsion system can be integrated into the airframe beneficially [1], to improve aerodynamic efficiency.

The demand for lower emissions has also renewed interest in propellers, since they offer the possibility of a higher efficiency and thus lower fuel burn than turbofans. Compared to turbofan engines, propellers operate at a higher efficiency at low Mach numbers (see Figure 1.1). A possible synergistic solution is a distributed over-the-wing propeller configuration. Since thrust is shared between more propellers, their diameter can be reduced. As a result, the size of the pylon they have to be installed on and the offset between their thrust line and the plane's center of gravity are both reduced. Over-the-wing propellers present other advantages, such as an elimination of ground clearance problems and reduced flyover noise, by the shielding effect of the wing [9, 10]. Furthermore, it has been shown that wing lift-to-drag ratio can be increased in both cruise [11] and high-lift [12] conditions. Finally, the propellers can be attached to the flap, which will lead to thrust vectoring when the flap is deflected[1]. Low-speed performance can thus be enhanced, permitting a reduction of the wing area.

[1] see for example https://lilium.com/

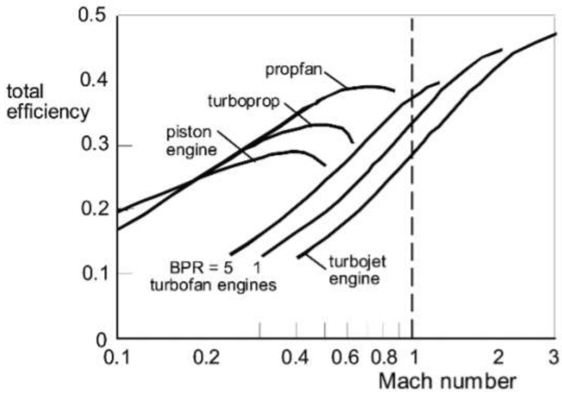

Figure 1.1: Total efficiency versus Mach number for several propellers and turbofans [13].

1.1. HISTORICAL CONTEXT

Historical examples of airplanes which have a propeller above the wing can be seen in Figure 1.2. The Dornier Do-X in Figure 1.2a was only built three times, since it sparked little commercial interest and was involved in several accidents. Figures 1.2b and c show experimental channel wing airplanes, which are specifically designed for very high lift, allowing short take-off and landing.

a) b) c)

Figure 1.2: Examples of over-the-wing propeller airplanes [14–16].

Similarly to the number of built designs, research on over-the-wing propellers has been limited [11, 12, 17–20]. In these studies, propellers have been typically sized for twin- or four-engine aircraft. Earlier research on distributed propeller configurations include for example tractor [6] and boundary-layer ingestion [8] configurations. Only one very recent study on a distribution of over-the-wing propellers could be found [21].

The limited amount of interest in over-the-wing propeller aircraft has been caused by a number of drawbacks to this configuration. The main disadvantages of propellers compared to turbofan engines are their high noise production, and their limitation in flight Mach number (see Figure 1.1), limiting their use to regional aircraft. Additionally, in an over-the-wing position, the propeller will be strongly affected by the wing. As such, the inflow will feature increased velocities and a vertical velocity gradient. This leads to a reduced propulsive efficiency [12, 18] and unsteady blade loading, thus increasing vibrations and noise production [22]. Moreover, interaction between the propeller tip vortices and the boundary layer may cause boundary layer separation [19].

These disadvantages have led aircraft manufacturers to prefer tractor propeller configurations for twin- or four-engine aircraft designs. Recently, however, interest in over-the-wing propeller systems has been renewed, since in a distributed propulsion setup, such a system is deemed more feasible. This has for example led to the design of ONERA's AMPERE airplane [23] and the Lilium Jet which was already mentioned earlier. Both can be seen in Figure 1.3.

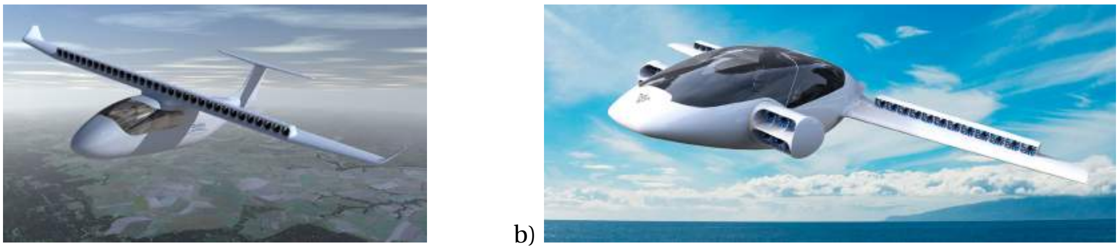

a) b)

Figure 1.3: Examples of modern aircraft employing a distributed over-the-wing propeller configuration: a) the ONERA AMPERA [24] and b) the Lilium Jet [25].

In the case of distributed-propulsion systems, propeller-wing interaction effects are even stronger in nature, and have a large impact on wing sizing [26]. Accordingly, they should be included in the first stages of the design process. This makes an over-the-wing propeller aircraft design all the more challenging, since the aerodynamic performance of the propeller and wing cannot be studied separately. Although there are low-fidelity methods which estimate propeller-wing interaction effects for tractor propeller configurations [27], none exist for over-the-wing configurations. This can be attributed to the limited application of over-the-wing systems up till today on one hand, and to the difficulty to model such systems on the other. While tractor propellers affect the dynamic pressure and angle of attack perceived by the wing [18], over-the-wing propellers affect the upper-surface pressure distribution [17], hence changing the effective airfoil shape. Modelling this effect requires a detailed understanding of the aerodynamic interaction effects.

However, existing studies on over-the-wing propellers [11, 12, 17–20, 28] are limited, and on occasions contradictory. While some authors have found moderate [12] to drastic [18] reductions in propeller efficiency, others have found an increase in propeller efficiency in some setups [11]. Analogously, most authors conclude that over-the-wing propellers reduce the drag of the wing [11, 18, 28], but for some configurations it has been found to increase [17]. Moreover, in the case of over-the-wing distributed propulsion, the ratio between the propeller diameter and the wing chord is smaller than in conventional twin- or four-engine aircraft. Therefore, the non-uniform inflow effects on the propeller will be more pronounced. Lastly, previous inquiries give no insight as to how the over-the-wing propeller can improve high-lift capabilities through thrust vectoring.

For these reasons, the purpose of this study is to develop a method capable of estimating the aerodynamic performance of over-the-wing systems. Since the dominant aerodynamic phenomena are not readily understood at this stage, the investigation will be limited to a single propeller in an over-the-wing configuration. In this way, the mutual effects between propeller and wing can be identified without the interaction between multiple propellers. Two experimental investigations are conducted which aim to clarify the aforementioned contradictions, and to assess the impact of smaller over-the-wing propellers in both cruise and high-lift conditions.

1.2. RESEARCH OBJECTIVES

The previous section has shown that over-the-wing propellers could be a promising propulsion layout for future airplanes. To explore the aerodynamic performance of these systems, the following research objective will be central to this thesis:

To analyze the aerodynamic interaction effects and quantify the performance of over-the-wing propeller systems by performing wind tunnel experiments, and by creating a tool suitable for estimating system performance in conceptual aircraft design.

The historical context has shown that in order to meet this objective, several questions must be answered. Firstly, the aerodynamic flow phenomena for over-the-wing propeller configurations are not understood in detail, leading to the following question:

1. What are the dominant aerodynamic flow phenomena for an over-the-wing propeller?
    (a) How does the propeller affect the wing pressure distribution?
    (b) In which way does the wing affect the propeller disk loading?
    (c) How does the wing deform the propeller slipstream?

Secondly, existing literature is incomplete and occasionally contradictory regarding over-the-wing propeller system performance, which creates the following research question:

2. How does the performance of over-the-wing systems compare to the isolated wing and propeller performances?
    (a) In which way does the propeller affect the wing lift, drag and pitching moment in cruise conditions?
    (b) What effects does the wing have on the propeller thrust, torque and efficiency in cruise conditions?
    (c) In which way does the propeller affect the wing lift, drag and pitching moment in high-lift conditions?
    (d) What effects does the wing have on the propeller thrust, torque and efficiency in high-lift conditions?

Existing literature is also occasionally contradictory regarding the effect of thrust setting and chordwise propeller position on system performance. Furthermore, no existing studies could be found on the effects of propeller diameter and only a limited number of studies on the effects of clearance between the propeller and wing. Accordingly, the third research question is:

4. Which parameters govern the performance of the system?

(a) How are wing and propeller performances affected by propeller thrust setting?

(b) What is the effect of chordwise propeller position?

(c) What is the effect of propeller diameter?

(d) What is the effect of clearance between propeller and wing?

Finally, there exists no numerical method to determine over-the-wing propeller system performance which is appropriate for the aircraft conceptual design phase. The last research question is thus:

5. How can the performance of over-the-wing propellers be determined in a preliminary design phase?

   (a) What are computationally effective ways to model the propeller, its slipstream and the wing?

   (b) In which way can the propeller and wing flow fields be coupled?

1.3. THESIS OUTLINE

An overview of the thesis structure will now be given. Chapter 2 discusses the relevant aerodynamic interaction effects between wing and propeller described in existing literature, relevant for over-the-wing configurations. Furthermore, it briefly explains the other benefits and drawbacks of such a configuration, mainly related to noise and airframe integration.

The methodology is laid out in Part II. Chapter 3 describes the two wind tunnel experiments that have been performed. The first experiment allows a detailed investigation of the effect of the propeller on the wing and qualitative information on the wing's effect on the propeller loading and slipstream. In the second setup the forces on the propeller can be measured, to determine the effect of the wing on the propeller quantitatively. The key findings are formalized by the development of a numerical model in Chapter 4. The model is capable of estimating propeller and wing performance without excessive computational costs.

The experimental and numerical results are highlighted in Part III. It begins with a discussion on cruise configuration performance in Chapter 5, in which the numerical model is also validated. Then, Chapter 6 shows the experimental results in high-lift configurations. The applicability of the numerical model is highlighted in Chapter 7, where it is used to perform sensitivity analyses. Finally, Chapter 8 consists of the conclusions and recommendations.

2

THEORY AND LITERATURE ON OVER-THE-WING PROPELLERS

In this chapter, a basic understanding of the aerodynamic interaction effects concerning over-the-wing propellers will be established by reviewing open literature. First, the necessary propeller aerodynamics will be explained. Then, the primary aerodynamic interaction effects are identified. Thirdly, the relevant aerodynamic effects of the propeller on the wing will be described, followed by the effects of the wing on the propeller. The knowledge gaps will be identified, which serve as goals for the rest of the thesis. Furthermore, other benefits and drawbacks of over-the-wing propellers, mainly related to engine integration and noise are briefly discussed.

2.1. ISOLATED PROPELLER AERODYNAMICS

To discuss over-the-wing propeller interaction effects, the aerodynamics of an isolated propeller will briefly be explained[1]. To determine the effects of an over-the-wing propeller on the wing, the propeller slipstream will first be characterized, with simplified momentum theory [30]. This theory represents the propeller by an infinitely thin disk imparting momentum onto the fluid. The flow is considered inviscid and incompressible and it assumes a low, uniform disk loading. While simple, it provides valuable insights into propeller slipstream effects.

An illustration of slipstream effects in this theory is contained in figure 2.1. Since the propeller accelerates the flow, the slipstream must contract to satisfy mass flow continuity, as shown in Figure 2.1a. Figure 2.1b depicts qualitatively how the air is gradually accelerated. The total pressure increases discontinuously at the propeller disk since the propeller increases the momentum of the flow, as shown in Figure 2.1c. Figure 2.1d shows how the static pressure changes. As the air is sped up, the static pressure decreases, both in front of and behind the propeller disk. At the disk itself, a discontinuity exists because of the total pressure increase.

An important operational setting of propellers is the advance ratio $J = \frac{U_\infty}{nD_\mathrm{P}}$, the ratio of freestream versus rotational velocity. High and low advance ratios correspond to slow and fast rotation, respectively. A propeller with diameter D_P at an angle of attack α_P is illustrated in Figure 2.2a. It delivers a thrust T and a torque Q. If the inflow to the propeller disk is non-uniform or at an angle of attack, normal and side forces N and Y are also acting on it [18]. The propeller's power is equal to $P = 2\pi Q$, and its efficiency is [13]:

$$\eta = \frac{TU_\infty}{2\pi Q}. \tag{2.1}$$

Figures 2.2A to C show blade section diagrams for different advance ratios. Assuming the propeller rotational speed is maintained, the advance ratio can be increased by increasing the flow velocity. At a low advance ratio (Figure 2.2A), the blade section encounters a high tangential velocity, but a low freestream velocity, leading to a high angle of attack. Both the thrust and torque are large. Optimal efficiency is achieved at an intermediate advance ratio (Figure 2.2B), leading to moderate angle of attack, thrust and torque. If the advance ratio is increased further (Figure 2.2C), the angle of attack decreases further, leading to small thrust, but considerable torque.

[1] For a more extensive review of propeller aerodynamics, see for example Wald [29].

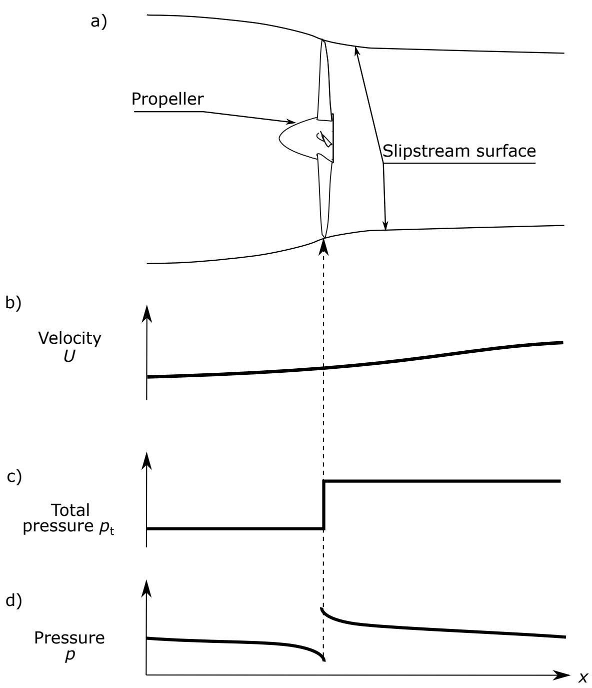

Figure 2.1: Illustration of actuator disk theory: flow speed, static and total pressure change across an actuator disk, adapted from McCormick [31].

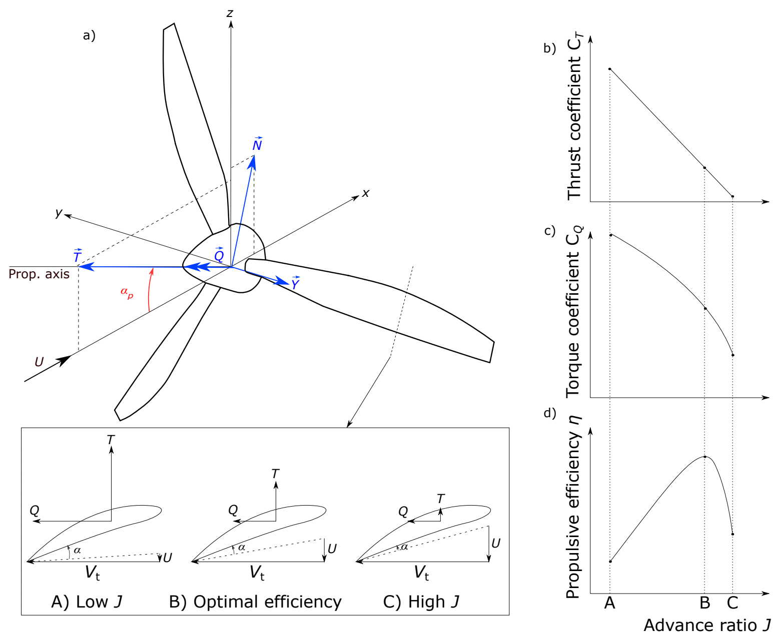

Figure 2.2: (a) A propeller with illustrations of the forces on it, generic blade section at (A) low, (B) intermediate and (C) high advance ratio and (b) thrust, (c) torque and (d) efficiency versus advance ratio (partly adapted from Torenbeek [13]).

It is often more insightful to express thrust and torque non-dimensionally as $C_T = \frac{T}{\rho n^2 D_P^4}$ and $C_Q = \frac{Q}{\rho n^2 D_P^5}$. The general behaviour of these coefficients and the efficiency versus advance ratio is shown in Figures 2.2b-d, with the operational points in Figures 2.2A-C indicated. The thrust decreases linearly with advance ratio, whereas the torque decreases quasi-parabolically. This leads to an efficiency that increases until a maximum at point B, after which it rapidly decreases.

2.2. AERODYNAMIC INTERACTION EFFECTS

In this section, the primary aerodynamic interaction effects between a wing and an over-the-wing propeller, illustrated in Figure 2.3, are explained. The propeller's primary effect on the wing is caused by the slipstream. This is illustrated in Figure 2.3a. The slipstream of a propeller producing thrust is contracting, leading to two regions on the wing surface. In Figure 2.3a, region I is washed by the propeller slipstream, while above region II, the slipstream surface diverges from the wing surface.

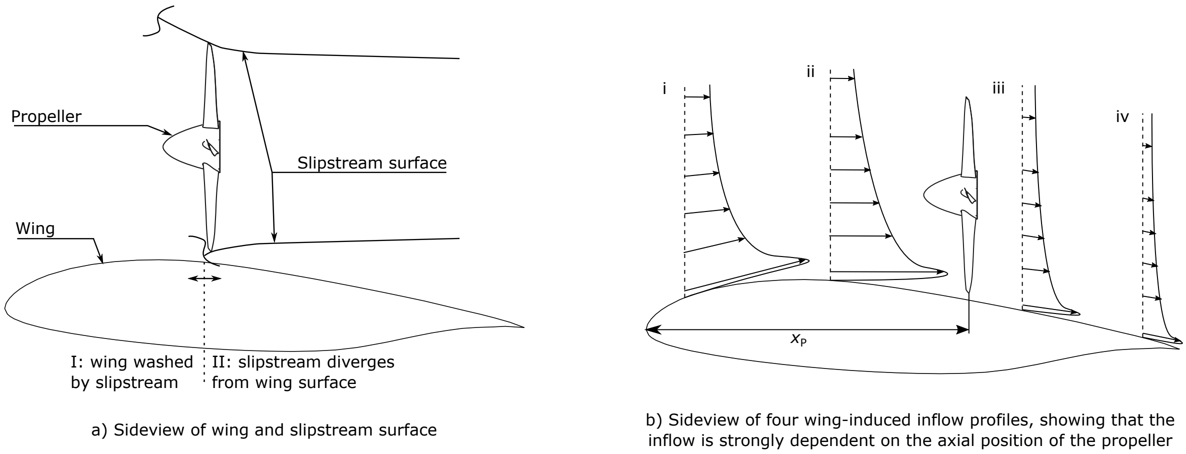

Figure 2.3: Generic sketches of the primary over-the-wing-propeller aerodynamic interaction effects.

The wing primarily affects an over-the-wing propeller by altering the inflow velocities at the propeller disk. This is illustrated in Figure 2.3b, in which generic wing-induced velocity profiles are sketched at four possible over-the-wing axial propeller positions. For steady, inviscid, incompressible flow, the local flow velocity is equal to $V = U_\infty \sqrt{1 - C_p}$ at the wing surface. Accordingly, wing-induced velocities are highest at the wing suction peak, near the leading edge. Moving aft, wing-induced velocities decrease, as in Figures 2.3i to iv. Wing-induced velocities increase from null at the wing surface to their maximum close to it, in the wing boundary layer. Furthermore, they are aligned with the wing surface close to it. The resulting vertical velocity component due to the wing contours was found earlier by Luijendijk [32]. Since very far away from the wing, wing-induced velocities must be zero and aligned with the freestream, their magnitude and angle to the freestream decrease further away from the wing. The consequences for propeller and wing performance and a more detailed explanation of the interaction effects are discussed in the next sections.

2.3. PROPELLER AERODYNAMIC EFFECTS ON THE WING

From actuator disk theory, two effects of the propeller on the wing for an over-the-wing installation can be deduced [33]. Firstly, the contraction of the slipstream causes increased flow angles of attack, as illustrated in Figure 2.4. This effect diminishes further away from the slipstream, since far away from the propeller, streamlines are aligned with the freestream. Secondly, since the slipstream is contracting, if angle of attack of wing and propeller are aligned, the wing is washed by the slipstream in front of the propeller disk. This part of the wing will encounter increased flow velocities and a decreased static pressure.

As a result, in front of and behind the propeller, the wing pressure distribution shows increased suction and pressure, respectively [11, 18, 20, 28][2]. This is shown in Figure 2.5. The increased suction in front of the propeller and increased effective wing angle of attack increase the wing's lift. Furthermore, the forces produced by the suction in front of and pressure behind the propeller may have forward-facing components, reducing the wing's pressure drag. The lift increase and drag decrease are stronger with higher thrust [18].

[2] The same effect can be seen for a propeller in close proximity to a wall [34].

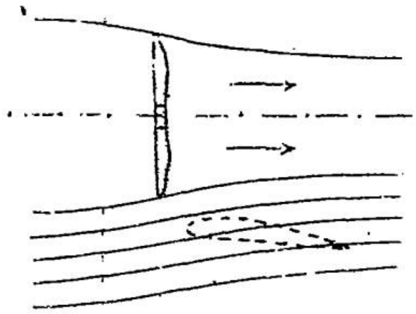

Figure 2.4: The propeller streamlines alter the effective angle of attack at the wing [33].

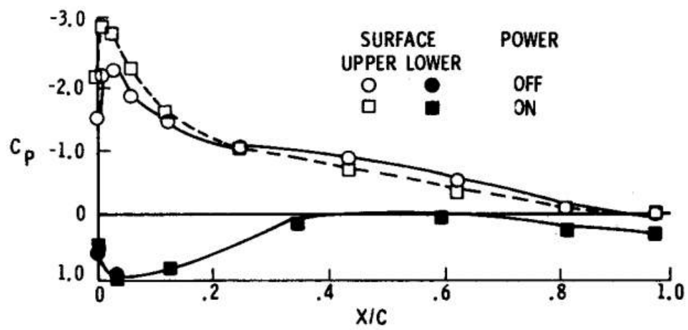

Figure 2.5: Effect of an over-the-wing propeller on the wing pressure distribution, power-on (squares) and power-off (circles) [11].

Previous studies [11, 17, 18, 28] agree on the drag being decreased most with the propeller positioned approximately above the thickest part of the wing. In this case, the decreased pressure in front of the propeller disk and increased pressure behind it have the highest forward-facing component. Concerning other effects of axial propeller position, reports are contradictory. While Johnson and White [11] have measured decreased drag for any over-the-wing position, other studies [17, 18, 35] find increased drag for propeller positions near the wing trailing edge. Moreover, several studies [17, 28, 35] find a higher lift increase for aft-wing propeller positions, whereas Veldhuis [18] finds the highest lift increase for a mid-wing position.

Additionally, the propeller changes the spanwise distribution of lift and drag. Figure 2.6 shows that with respect to the clean wing, the lift increase and drag decrease are strongest at the propeller axis and spanwise symmetrically around it for an over-the-wing configuration. On the other hand, a propeller in tractor configuration[3] strongly distorts the lift distribution which requires changing the wing's twist distribution to prevent a significant increase in induced drag [36]. This spanwise distortion can also be seen in Figure 2.6 for a configuration with the flap deflected. This causes increased drag in tractor configuration, since the wing is immersed in the slipstream, which causes suction on the flap's aft-facing top surface. In cruise configurations, tractor propellers can also decrease wing drag [18]. However, the lift distribution is more non-elliptical in a tractor than in an over-wing configuration, leading to a higher induced drag. Furthermore, the lift increase is higher for the tractor than over-wing configuration. This is a result of the lower propeller thrust, which will be explained in the next section.

Little is known about how these effects add up for a distributed, over-the-wing propeller system. Research on distributed over-the-wing turbofans [37, 38] and tractor propeller configurations [26, 39] indicate that there is a potential for high gains in aerodynamic efficiency. The possibility to substantially increase the wing's lift is especially beneficial to low-speed performance and may allow a reduction in wing area, which will lead to better cruise performance. Recent research [21] shows that in distributed propulsion applications, over-the-wing propellers have a similar effect on the wing pressure distribution, lift and drag as single over-the-wing propellers. However, the effects are stronger, since the propellers affect more than the wing span interval that they cover. Additionally, there are interaction effects between propellers, such as alteration of

[3] I.e., a propeller positioned upstream of the wing.

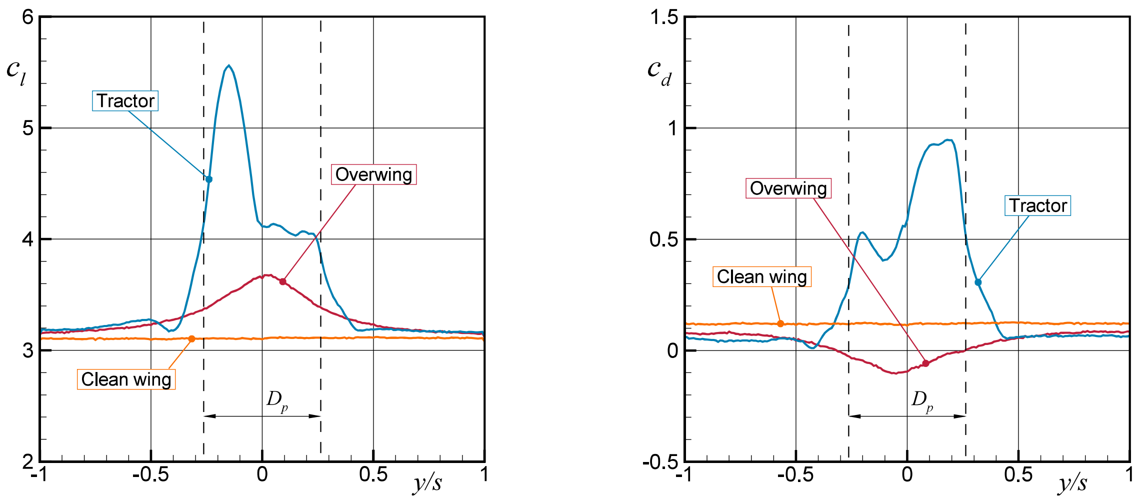

Figure 2.6: Spanwise lift (left) and drag (right) distributions of tractor and over-the-wing propeller high-lift configurations. Results are from CFD by Müller et al. [20].

the propeller inflow by other propellers and propeller slipstreams interacting. Remarkably, a negative wing drag was found for a wide range of axial propeller positions.

Müller et al.[20] show that the effect of an over-the-wing propeller on the wing pressure distribution is dominantly potential in nature. In their numerical setup, only if the boundary layer is penetrated by the propeller, significant viscous interactions are present. Even so, the increased suction in front of the propeller is expected to slightly delay boundary layer transition if the propeller is behind the isolated-wing transition location, similarly to pusher propeller configurations[4] [40] and over-wing nacelles [38].

CFD simulations [19, 21] indicate that the interaction between propeller blade tip vortices and the wing boundary layer may cause boundary layer separation. A propeller above a wall similarly showed separation at a high propeller thrust setting [34]. Note that in all instances of flow separation, the propeller blades penetrated the boundary layer.

2.4. WING AERODYNAMIC EFFECTS ON THE PROPELLER

The primary effect of the wing on the propeller is an altered inflow velocity profile, which has been shown in Figure 2.3b. An example of the resulting thrust distribution for a mid-wing position leading to a vertical inflow gradient can be seen in Figure 2.7a. Wing-induced velocities decrease towards the top side of the propeller disk, leading to more thrust being generated at the top side. Secondly, the propeller may receive inflow at an angle of attack. Figure 2.8 shows that this increases and decreases the loading on the down- and up-going blades respectively, for positive angle of attack. The effect on the thrust distribution can be seen in Figure 2.7b, which shows that the propeller generates more thrust at the down- than at the up-going blade side. Similar loading distributions are found for distributed over-the-wing propellers [21].

The altered propeller disk inflow significantly changes propeller performance. Firstly, the increase in propeller disk inflow velocities causes an increase in effective advance ratio. Figures 2.2b and c indicate that this will lead to decreases in thrust and torque. According to Figure 2.2d, the propeller efficiency increases or decreases, for a propeller operating between points A and B or B and C, respectively. Secondly, pusher propeller experiments indicate that the non-uniform nature of the vertical velocity gradient generally leads to a decreased efficiency [42]. Thirdly, the angle of attack slightly increases thrust, torque and efficiency [41], more so for lower propeller advance ratios.

As a combination of these effects, compared to an isolated propeller, thrust and efficiency decreases have been found experimentally for over-the-wing propellers [12, 18, 33, 35] and Johnson and White's climb configuration [11]. However, in a cruise configuration, Johnson and White [11] found an increased propeller efficiency. In this case, the wing-induced velocities may have strongly changed the effective advance ratio towards the point for optimal efficiency.

[4] I.e., a propeller positioned downstream of the wing.

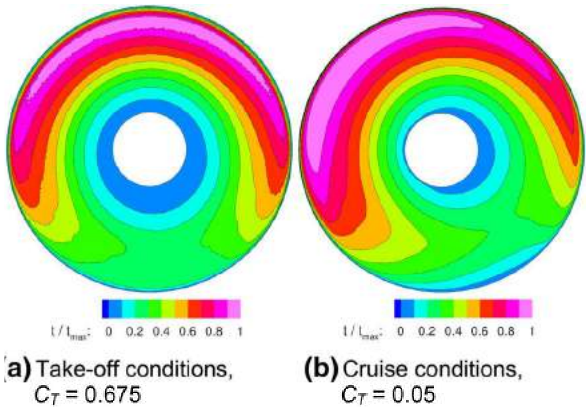

Figure 2.7: Over-the-wing propeller thrust distributions according to CFD by Müller et al.[12] with the wing at (a) zero and (b) positive angle of attack.

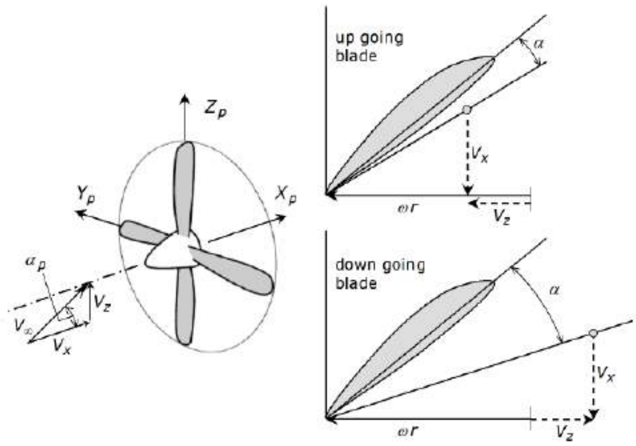

Figure 2.8: Up- and down-going blade section diagrams for a propeller at an angle of attack [41].

Furthermore, the loading distributions affect the forces on the propeller in the disk plane. Figure 2.9 presents the in-plane forces for three loading distributions. In the case of uniform loading (Figure 2.9a), the normal and side force components dN and dY on the blades are balanced, leading to the overall in-plane forces being zero.

For an over-the-wing propeller positioned mid-wing, a vertical gradient in the inflow velocities is expected. This gradient, shown in Figure 2.9a, leads to the generation of a side force. Since the propeller loading is lower close the wing, the disk-plane force on the propeller blade is stronger at the top of the propeller rotation than at it the bottom. This leads to a negative or positive side force for right- or left-hand rotation, respectively.

On the other hand, if the propeller is positioned near the wing trailing edge, the inflow is expected to have a negative angle of attack. This inflow, shown in Figure 2.9c, causes a normal force. As explained, a negative angle of attack causes a higher loading on the up-going blade, leading to a downward normal force, whereas a positive angle of attack produces an upward normal force.

Secondary aerodynamic effects of the wing on an over-the-wing propeller include the movement of the slipstream by wing-induced velocities and an earlier onset of compressibility effects. Since no research has been found on over-the-wing propeller slipstream characteristics, they will be investigated experimentally in this thesis.

Regarding the earlier onset of compressibility effects, towards their tips, propellers experience significantly higher Mach numbers than freestream, since the addition of freestream and rotational velocities leads to a higher effective velocity. Correspondingly, shock waves, wave drag and drag divergence on propeller blades are encountered at early freestream Mach numbers, limiting propeller aircraft flight speeds. Above the

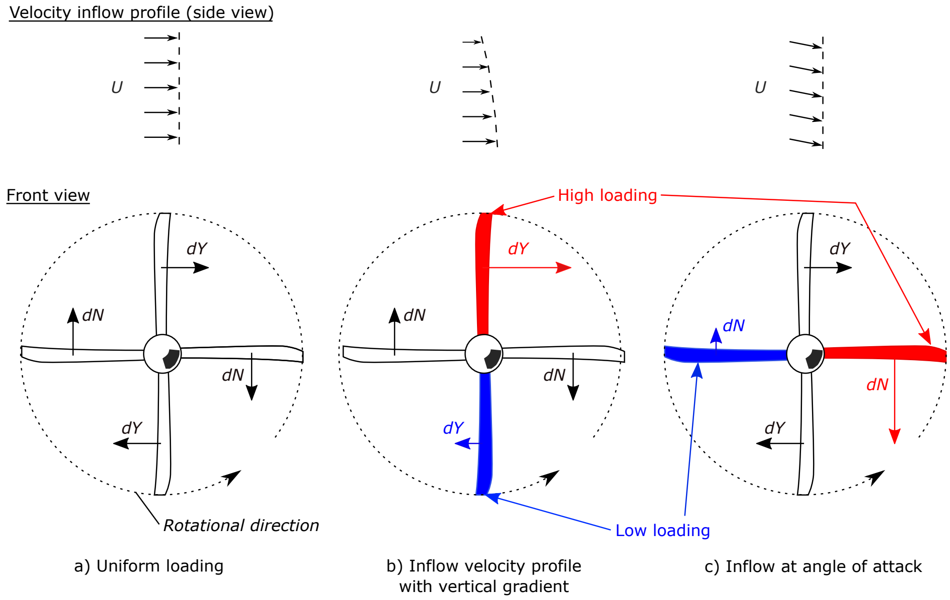

Figure 2.9: In-plane forces on the propeller for three loading distributions.

wing, flow speeds are even higher, leading to an even lower flight speed limit for over-the-wing propeller aircraft. As an example, CFD investigations by Müller et al. [35] show that the performance of a propeller above a channel wing deteriorates faster with increasing Mach number than a tractor propeller. To avoid supersonic inflow, this research was limited to $M = 0.6$, while the tractor reference operated at a Mach number of 0.74. Note that this is an extreme case, since channel wings generally create higher supervelocities above the wing than straight wings.

2.5. ADDITIONAL OVER-THE-WING PROPELLER CONSIDERATIONS

Next to the discussed aerodynamic effects, another important aspect over-the-wing propellers is their production of noise. Most importantly, due to the shielding effects of the wing, flyover noise can be reduced [9, 10, 35]. However, the unsteady propeller blade loading causes increased noise production [22]. Moreover, the interaction between propeller tip vortices and the wing surface leads to structure-borne noise, which increases the noise in the cabin [9]. The same study showed that this problem may be overcome by installing porous liners in the wing, under the passing location of the blades.

Installing propellers over the wing reduces ground clearance challenges, but presents other problems. Firstly, pylons to mount the nacelle on are required. Research on over-the-wing turbofan engines [43–46] indicates that the over-the-wing installation generally decreases the lift-to-drag ratio, which can negate the aerodynamic benefits for the wing. Nonetheless, recent developments in numerical modelling have shown that, in the case of turbofan engines, optimisation of the installation may lead to an overall aerodynamic efficiency equal to [47] or higher than [48, 49] for a conventional engine position. Recent research [50] has however shown that such an optimisation is onerous in the transonic flight regime, due to the interaction with shockwaves. Near the wing leading edge, nacelles increase the strength of the wing's shock wave, leading to increased wave drag. On the contrary, near the wing trailing edge, nacelles reduce the wing's shock wave strength by increasing the back pressure, leading to decreased drag and lift.

Finally, an over-the-wing installation is less compact than a tractor configuration, leading to a higher weight [12], although part of the weight increase shown in this paper may be due to the channel wing. Further research on these other considerations is outside the scope of this thesis, but is highly recommended in the future. The reduction in flyover noise, installation challenges and possible weight increase may be of high importance when considering an distributed over-the-wing propeller configuration.

II

METHODOLOGY

3

EXPERIMENTAL APPROACH

3.1. EXPERIMENT 1

The first wind tunnel experiment was carried out in the closed-section, low turbulence tunnel at the Delft University of Technology. In this experiment, the effect of an over-the-wing propeller on the wing pressure distribution and wing performance was studied, in cruise and high-lift configurations. Furthermore, this setup allows a qualitative investigation of the effect of the wing on the propeller loading and slipstream deformation. A cross-section of the tunnel is shown in Appendix C. This wind tunnel has a maximum velocity of 120 m/s and freestream turbulence limited to a level of 0.02% for velocities below 40 m/s [51].

3.1.1. MODEL DESCRIPTION

In order to simulate an over-the-wing propeller configuration, a propeller was positioned on the suction side of a wing mounted vertically in the wind-tunnel test section, as depicted in Figures 3.1, 3.2 and 3.3. The wing spanned the full height of the test section and was placed on a turntable, which could be rotated to change the angle of attack. It featured a chord of 0.6 m and an NLF-MOD22B airfoil designed at Delft University of Technology for low speed applications [52], with a maximum thickness-to-chord ratio of 0.17 at 35% chord. The airfoil and its coordinates can be found in Appendix A. A fowler flap of 30% chord length is attached. The main dimensions of the experimental model are indicated in Figure 3.1. As can be seen in Figure 3.2, vortex generators were placed on the suction and pressure sides of the wing, next to the wind tunnel wall junction, to prevent flow separation observed in earlier experiments [53].

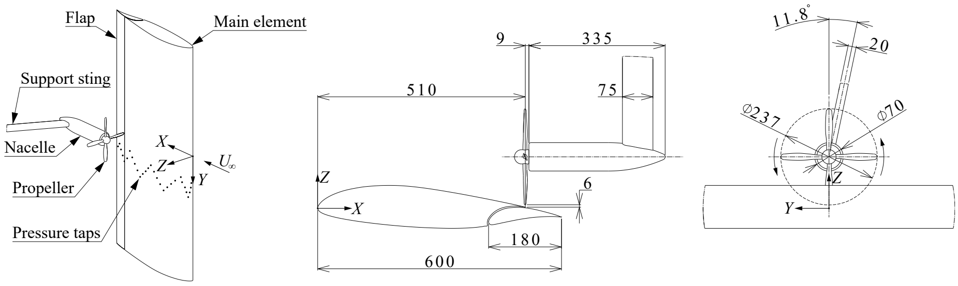

Figure 3.1: Isometric (left), top (middle) and front (right) views of the setup of Experiment 1, including component designation, coordinate system and direction of rotation of the propeller. All dimensions are in mm.

The four-bladed propeller model has a diameter of $D_P = 0.237$ m ($D_P/c = 0.395$), a blade chord of 7.8% of the propeller diameter, and a pitch angle of 23° at 75% of the propeller radius. The propeller is a scaled version of the Hamilton Standard 6101 model used in the DHC-2 Beaver airplane. More information on the propeller geometry can be found in Appendix B. The propeller was driven by a 7.5 hp three-phase induction motor housed in a nacelle of 0.07 m diameter, positioned by means of a support sting which could be traversed along all three axes, by the mechanism shown in Figure 3.2. The support sting was installed under a small inclination angle as depicted in Figure 3.1, in order to position the propeller axis at the spanwise position of the pressure ports (see Section 3.1.2) when the traverse mechanism was set at its neutral position along the y-axis.

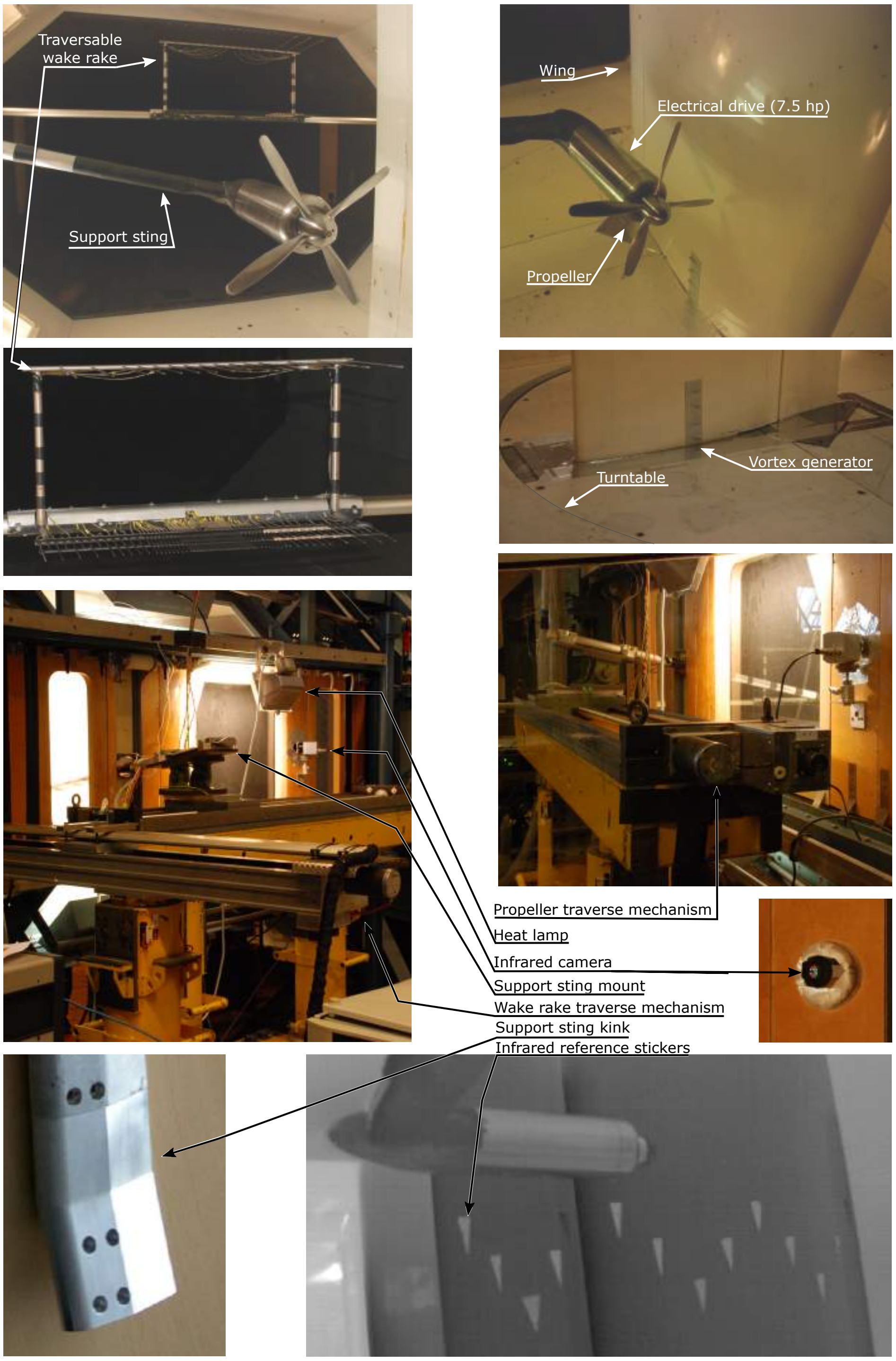

Figure 3.2: Photos of Experiment 1, with components indicated.

3.1.2. MEASUREMENT TECHNIQUES

In the experiment two main variables were measured: the pressure distribution on the wing surface and the total pressure distribution in a wake plane (a (y, z)-plane downstream of the model). The former was measured in order to quantify the effect of the propeller on the wing's pressure distribution, lift, and pressure drag, while the latter provided qualitative information regarding the time-average loading on the propeller disk and the displacement of the slipstream and wing wake.

Additionally, an Optris PI640 infrared camera was installed during all measurements to observe the boundary layer transition location, as shown in Figure 3.2. Since the wing cooled due to the wind tunnel flow, it was heated with a heat lamp until an infrared photo was taken, to keep the transition visible. The infrared images were related to chordwise locations by making a reference image with stickers at pressure port locations each time the camera position was changed.

Figure 3.3 shows schematic cross-sections of the setup. A front view of the propeller-wing setup is depicted in Figure 3.3a. In order to obtain the surface pressure distribution, the wing model featured 54 static pressure ports on the main element and 27 on the flap, distributed over the pressure and suction sides. The ports were located along a zigzag path extending over a spanwise interval of 100 mm, as indicated in Figure 3.1. As a spanwise reference position, the propeller was aligned with the middle of the pressure taps. For each configuration, the propeller was traversed in spanwise direction to resolve the wing pressure distribution, covering a span of $1.5D_\mathrm{P}$.

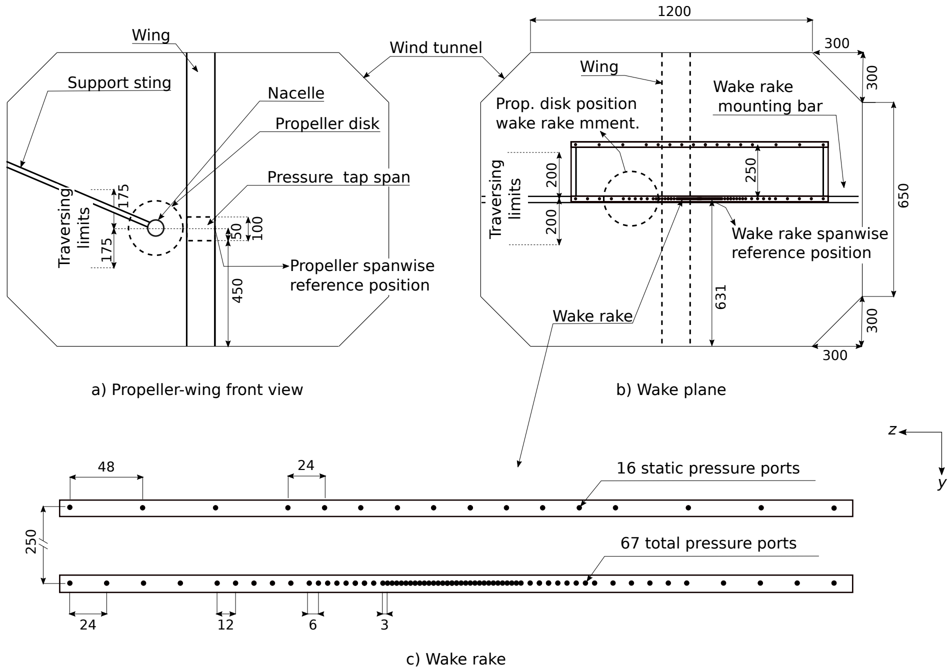

Figure 3.3: Experiment 1 cross sections (this cross section does not include the kink in the sting that was used in Configurations 5 and 6, which is explained in Section 3.1.3) and dimensions of the wake rake. All dimensions are in mm.

Wake plane pressure measurements were performed with a horizontal wake rake located 1.25 chord-lengths downstream of the wing trailing edge, which is shown in Figure 3.3b. The wake rake probe locations can be seen in Figure 3.3c. The full span of the rake was $2.1D_\mathrm{P}$, which was insufficient to capture the propeller slipstream and wing wake with acceptable resolution in a single traverse along the y-axis. Accordingly, for each measurement configuration the wake rake was traversed along the wing span twice, centering the rake once around the propeller slipstream and once around the wing wake. Each traverse covered a spanwise interval of $1.7D_\mathrm{P}$, centered around the vertical position of the propeller axis. The traversing system is pointed out in Figure 3.2. Note that the traversing limits of the propeller and wake rake make it impossible to capture the whole static pressure field. Relative to the wind tunnel floor, the highest spanwise position of the propeller is 675 mm, while the lowest spanwise position of the static pressure probes is 681 mm. The only way to remedy this, would have been to change the support sting inclination for every tested configuration, which was not possible due to time constraints.

3.1.3. TEST CONDITIONS

The wing was set to an angle of attack which was representative of cruise conditions ($C_L \approx 0.5$) and referenced in earlier experiments [52], $\alpha_w = 2.08°$. To simulate high-lift conditions, the maximum possible flap deflection of $\delta = 23°$ was selected, which was limited by the geometry of the support sting. For the selected deflection angle, the values of flap gap and overlap (defined in Figure 3.4) were selected to be of 3.9% and 3.5% chord length respectively, based on earlier reports [52].

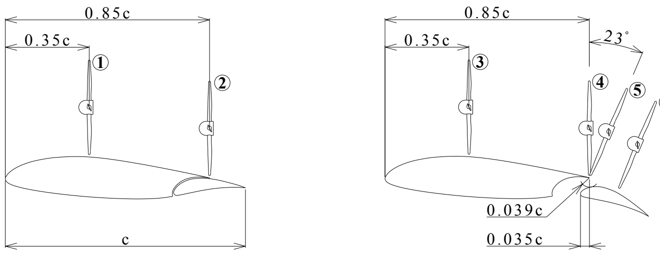

Figure 3.4: Side view of the six configurations analyzed in Experiment 1, separated into flap nested (left) and flap deflected (right) cases.

Figure 3.4 shows the chosen configurations. For the cruise conditions (flap nested), two axial propeller positions were evaluated: the location of maximum airfoil thickness (Configuration 1, at 35% chord) and the trailing edge of the main element (Configuration 2, at 85% chord). These locations were selected based on the observations of earlier studies [11, 17, 18], which indicate that the axial position of maximum wing drag reduction and lift increase are close to the thickest point and the trailing edge respectively. However, the trailing edge of the flap was not considered due to the structural complications that would arise in real applications and the potential reduction of noise shielding effects. The separation between the propeller blade tips and wing surface was chosen as low as possible[1], since the drag reduction has been found to be larger for smaller clearances [11]. The propeller axis was aligned with the freestream direction for simplicity.

For the high-lift conditions (flap deflected), two additional propeller positions were evaluated. The first one features a propeller that is located at 85% chord in cruise conditions (Configuration 2) but is rotated 23° around the main element's trailing edge when the flap is deflected (Configuration 5). The second one corresponds to the position that the propeller would have attained if it were physically connected to the flap (Configuration 6). To rotate the propeller in the (x, z)-plane, a kink was attached to the support sting, which is shown in Figure 3.2.

A summary of the tested parameters is given in Table 3.1. Advance ratios of 0.7, 0.8 and 0.9 were selected for the current experiment, based on isolated propeller data obtained in earlier experiments [54]. These values correspond to isolated-propeller thrust coefficients of 0.12, 0.10 and 0.06, respectively. Configuration 6 was not measured at advance ratio 0.8 due to time constraints. The isolated propeller thrust measurements were performed at a wing-chord based Reynolds number of 1.65 million, and thus this Reynolds number was selected for the test campaign, corresponding to a free-stream velocity of approximately 41 m/s. For every setup, a measurement was also taken with the propeller removed and replaced by a dummy hub for reference. Additionally, measurements were taken of only the wing.

Table 3.1: Summary of Experiment 1 test conditions.

Parameter	Test values
Diameter-to-chord ratio D_P/c	0.395
Wing angle of attack α_w	2.08°
Flap deflection δ	0°, 23°
Propeller positions	See Figure 3.4.
Propeller tip clearance d/c	0.01
Propeller advance ratio J	0.7, 0.8, 0.9
Reynolds number Re	$1.65 \cdot 10^6$

The used Reynolds number is realistic for a transport aircraft, but the Mach number is approximately 0.12, whereas real aircraft generally operate at Mach numbers higher than 0.5. This was however not possible in this experiment, since the torque on the propeller would have exceeded the power that the motor could

[1] For safety reasons, this was considered to be 6 mm, i.e. 1% chord.

deliver and the wind tunnel was limited to a maximum Mach number of 0.36. Furthermore, the absence of significant compressibility effects allows a more fundamental investigation of the potential and viscous flow effects. To extend the validity of the results, experiments at a higher Mach number should be executed.

3.1.4. DATA PROCESSING

The measured pressures on the wing were used to compute the wing pressure coefficient $C_p = \frac{p-p_\infty}{0.5\rho U_\infty^2}$. Trailing edge pressures were extrapolated based on the two most-aft upper surface pressure measurements. By integrating the pressure distributions, wing lift and pressure drag were obtained. Note that for the computation of these coefficients the reference area considered spans one propeller diameter, i.e. forces are evaluated over an area of $S_{\mathrm{ref}} = c \cdot D_{\mathrm{P}}$, and not over the entire wing.

To compute the wing performance coefficients, the wing is first divided into panels. Pressures are interpolated onto each panel midpoint. An example is shown in Figure 3.5. If the angle in the (x,z)-plane between the panel and the freestream direction is φ, the lift is the z-component of the pressure force on the panel, i.e. $l_p = (p - p_\infty)\cos\varphi\,\mathrm{d}s$, and the pressure drag the x-component, i.e. $d_p = (p - p_\infty)\sin\varphi\,\mathrm{d}s$. The panel's quarter-chord pitching moment is equal to $m_p = -(p - p_\infty)\cos\varphi(x_{\mathrm{p}} - c/4)\,\mathrm{d}s$ for panel x-coordinate x_{p}. The forces and the moment are converted to sectional coefficients by dividing them by the dynamic pressure and their area and integrated to find the total coefficient on the wing. As an example, the total lift coefficient is equal to $C_L = \int_{S_{\mathrm{ref}}} \frac{(p-p_\infty)\cos\varphi\,\mathrm{d}s}{0.5\rho U_\infty^2 S_{\mathrm{ref}}}$. Drag and quarter-chord pitching moment coefficients are computed similarly. Lift, pressure drag and pitching moment coefficients were corrected for streamline curvature, wake blockage, and wing blockage [55]—but not for slipstream blockage, since the propeller disk area represents only 2% of the cross-sectional area of the wind tunnel. A detailed explanation of wind tunnel corrections is given in Appendix D.

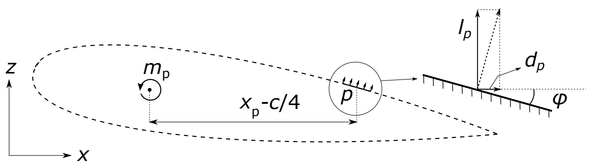

Figure 3.5: Side view of a generic airfoil panel, with the forces caused by the pressure on it indicated.

The wake plane pressure measurements were first converted to total pressure coefficients $C_{p_{\mathrm{t}}} = \frac{p_{\mathrm{t}}-p_\infty}{0.5\rho U_\infty^2}$. Since the two wake rake traverses overlapped, an interpolation was made in the overlap region. The wake plane pressure measurements could not be used to compute the net thrust $T - D$, because static pressure measurements were needed to do this [56]. These were not available for the full wake plane, as explained in Section 3.1.2. The wake plane measurements will thus only be used qualitatively to deduce the effect of the wing on the propeller and to assess the numerical modelling of the slipstream deformation.

3.1.5. REPEATABILITY

Error sources in Experiment 1 are the precision of the pressure scanners, pressure loss in tubes leading to the scanners, propeller or wake rake positioning errors and data processing errors. Firstly, the used ESP pressure scanners have an accuracy of 0.01%, leading to a negligible error. The pressure loss in tubes is also considered to be small. The traversing systems used to position the wake rake have an accuracy of 0.01 mm. It was however observed that the propeller and wake rake shaked slightly after moving them. To prevent this from influencing the measurements, a pause of ten seconds was introduced before any measurement. Lastly, data processing errors, such as error propagation in wind tunnel correction and integration or interpolation of data, are also considered to be small compared to the positioning error.

Figure 3.6 presents a measurement series on the wing with the same setup on different days. It can be seen that there is good agreement: the difference between the measurements is generally within 0.5% of the freestream dynamic pressure. The largest differences (approximately 1.5% of the freestream dynamic pressure) can be seen at the main element leading edge, where there is a steep pressure gradient. Other measurements showed similar differences when repeated.

To estimate the repeatability error in the calculation of the wing lift and drag coefficients, several measurements repeated (some on different days) were used to calculate them twice. Examples of the relative errors between repeated measurements, i.e. $\sigma C = |1 - C_1/C_2|$ for $C = C_L, C_{D_p}$ and $C_{m_{c/4}}$ are shown in Table 3.2. The

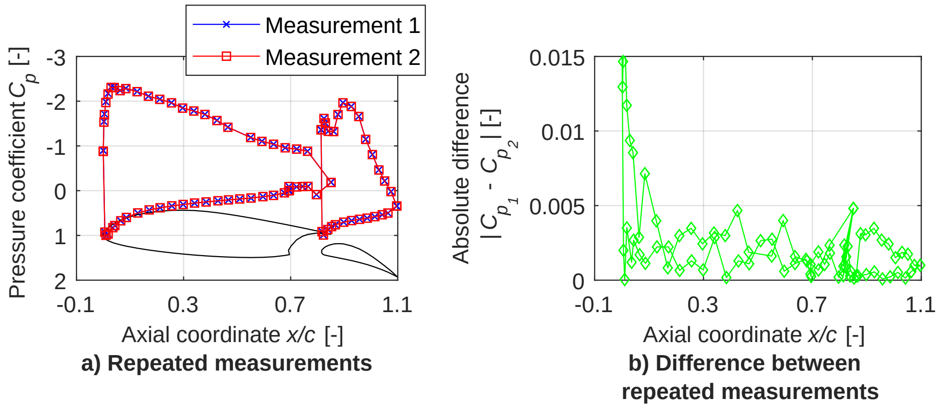

Figure 3.6: Repeated measurements of the wing pressures and their absolute difference in Experiment 1, Configuration 3 at $J = 0.7$.

Table 3.2: Relative errors in computed lift, pressure drag and pitching moment coefficients between repeated measurements.

Configuration	**Lift coefficient** $\sigma C_L = \lvert 1 - \frac{C_{L_2}}{C_{L_1}} \rvert [-]$	**Press. drag coefficient** $\sigma C_{D_p} = \lvert 1 - \frac{C_{D_{p1}}}{C_{D_{p2}}} \rvert$ [-]	**Pitching moment coefficient** $\sigma C_{m_{c/4}} = \lvert 1 - \frac{C_{m_{c/4_1}}}{C_{m_{c/4_2}}} \rvert$ [-]
1, J =0.9	0.2%	0.2%	0.1%
2, J =0.7	0.2%	2%	1%
3, J =0.7	0.2%	0.8%	0.1%
4, Prop. off	0.2%	0.01%	0.01%
5, J =0.8	0.01%	0.2%	0.01%
6, J =0.8	0.1%	0.4%	0.01%

absolute differences in lift, pressure drag and pitching moment coefficients are of the orders $1 \cdot 10^{-3}$, $1 \cdot 10^{-4}$ and $1 \cdot 10^{-4}$, respectively. This leads to relative errors of 0.01% to 0.2%, 0.01% to 2% and 0.01% to 1%, respectively. No dependence of the error on advance ratio was found, but the errors in Configuration 2 were found to be significantly larger than in other configurations. It is unclear what the reason for this is.

Figure 3.7 shows a comparison of pressure distributions in the wake plane downstream. It contains measurements on different days for Configuration 5 at two advance ratios. Generally, the differences, shown in Figure 3.7c, are small, within 5% of the freestream dynamic pressure. In the areas with steep pressure gradients, however, differences become larger, up to 10% of the freestream dynamic pressure at the edges of the slipstream. Figures 3.7d, 3.7e and 3.7f, demonstrate that the measurement errors at the slipstream edges become larger when the advance ratio is decreased, due to the steeper pressure gradients. In this case, the absolute difference between the measurements becomes up to 20% of the freestream dynamic pressure at the slipstream edge. Similar errors were observed for other Configurations.

It should be noted that while the differences in the wake plane measurements appear to be very large, they are primarily caused by differences in the location of the slipstream or wing wake. The movement of the slipstream location may have two causes. Firstly, in the first measurements, the wake rake center was closer to the propeller slipstream, while it was closer to the wing wake in the second measurements. This causes the resolutions in these areas to be different. This may indicate that during the second measurement, the experimental resolution was insufficient to precisely resolve the slipstream edge. Secondly, wake rake locations may have been slightly different in both measurements, due to the shaking of the wake rake.

3.2. EXPERIMENT 2

Expiriment 2 was performed in the Open Jet Facility at the Delft University of Technology. The propeller in this experiment contains a rotating shaft balance, allowing a quantitative analysis of propeller performance, which was not possible in Experiment 1. This is used to quantitatively determine the effect of the wing on propeller thrust, torque and efficiency. Furthermore, the effect of axial propeller position and clearance to the wing on propeller performance is assessed. Appendix C contains a cross section of this wind tunnel. This open-section wind tunnel can produce a maximum flow velocity of 35 m/s.

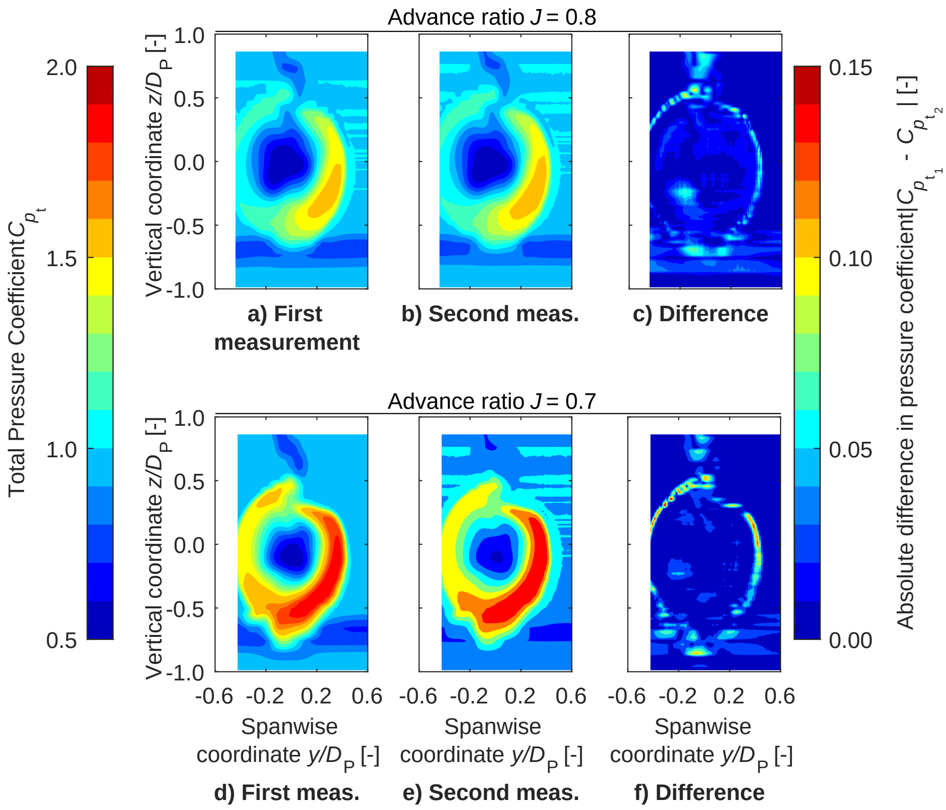

Figure 3.7: Repeated measurements in the wake plane and their absolute difference in Experiment 1, in Configuration 5.

3.2.1. MODEL DESCRIPTION, MEASUREMENT TECHNIQUES AND DATA PROCESSING

Similarly to Experiment 1, in Experiment 2 a propeller is positioned on the suction side of a wing placed vertically in a wind tunnel test section. The wing, with a span of 1.25 m, was placed vertically on the test section, as shown in Figures 3.8 and 3.9. At the top end of the wing, a flat plate was installed to reduce wing end effects. The plate was too small to fully remove them, but structural concerns made it impossible to make it larger. The wing's airfoil coordinates can be found in Appendix A. Its chord was equal to 0.74 m and its maximum thickness-to-chord ratio was 0.18 at 35% chord. Zigzag tape was placed along the complete wing span to trip the wing upper surface boundary layer, which was confirmed to be fully turbulent with an inflow microphone.

The propeller used in this experiment was a six-bladed scale version of the Fokker F50 Dowty-Rotol propeller. It has a diameter of D_P= 0.406 m (D_P/c = 0.550) and a pitch angle of 30° at 70% of the propeller radius. Details on the propeller geometry can be found in Appendix B. Its nacelle has a diameter of 0.08 m and houses an air motor, delivering up to 60 hp, and was positioned on a strut attached to the floor plate. The propeller hub houses a rotating shaft balance, allowing a direct measurement of three-component forces and moments on the propeller, on which more information can be found in [57]. Furthermore, a pitot tube was used to obtain propeller-off measurements (see Figure 3.8), to characterize the flowfield around wing and nacelle. The results of Experiment 2 are limited to propeller thrust, torque and propulsive efficiencies. Results were extracted from the measurement data files by a programming routine written by Sinnige [58].

As explained in Section 2.4, the non-uniform inflow to the propeller disk above the wing leads to in-plane forces on the propeller. The rotating shaft balance also measures the forces in the disk plane. These measurements were made in the rotating reference frame. To find the in-plane forces, the measured components must thus be transformed to a stationary reference frame. During the processing of the data, it was observed that there was a delay in time between the measurement itself and the recorded measurement time. This delay increased in length with decreasing advance ratio, and made it impossible to determine the azimuthal position of the propeller at the measurement time. To characterize the delay, propeller-off measurements

Figure 3.8: Photos of the setup of Experiment 2, with components indicated.

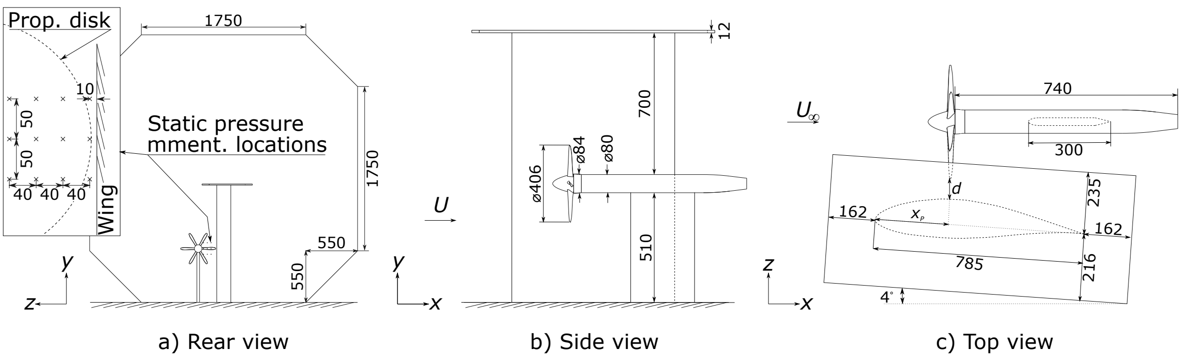

Figure 3.9: Rear, side and top views of Experiment 2, with static pressure measurement locations indicated. All dimensions are in mm.

would have to be performed, which was not possible in the limited time that the wind tunnel was available. Accordingly, in-plane force results will be limited to the numerical simulations.

3.2.2. TEST CONDITIONS

The limited span of the wing was expected to significantly reduce its lift coefficient due to wing tip effects at the top plate. Accordingly, the angle of attack was chosen higher than in Experiment 1, $\alpha_\mathrm{W} = 4°$. According to an XFOIL simulation, the 2D sectional lift coefficient at this angle of attack is $C_L = 0.95$. The panel code simulations which will be presented later, confirmed that there were significant wing tip effects, leading to a lift coefficient of $C_L = 0.61$ on the wing reference area under the propeller. Since the wing had no flap, only cruise configurations were tested, with the axial propeller position at 35%, 60% and 85% chord. The propeller was placed at three clearances: d/c = 1%, 5% and 10%. All three clearances were tested for $x_\mathrm{P}/c = 0.35$ and 0.85, but only 1% and 10% chord for $x_\mathrm{P}/c = 0.60$ due to time constraints.

A summary of the tested parameters is given in Table 3.3. The propeller performance at a clearance of 1% chord was measured at advance ratios 0.4 to 1.2 (corresponding to isolated-propeller thrust coefficients of 0.35 to 0.06), with steps of 0.1. At 5 and 10% chord clearance, advance ratios of 0.6, 0.8 and 1.0 were tested. The experiments were performed at a wind tunnel velocity of 20 m/s, since isolated propeller performance results were available at this velocity. This velocity lead to a Mach number of approximately 0.06, which is not comparable to real aircraft, but a realistic Mach number was not attainable, considering the maximum wind tunnel velocity. The chord-based Reynolds number at this velocity was 0.60 million, which is representative of transport aircraft. Pressure measurements with the propeller blades taken off, in the 35% chord position, were also made, using the Pitot tube. These measurements will be used to validate the panel simulation for this experiment, their locations are indicated in Figure 3.9a.

Table 3.3: Summary of Experiment 2 test conditions.

Parameter	**Test values**
Diameter-to-chord ratio D_P/c	0.550
Wing angle of attack α_W	4°
Flap deflection δ	0°
Axial propeller position x_P/c	0.35, 0.60, 0.85
Propeller tip clearance d/c	0.01, 0.05, 0.10
Propeller advance ratio J	0.4 to 1.2
Reynolds number Re	$0.60{\cdot}10^6$

3.2.3. REPEATABILITY

The two main error sources in Experiment 2 are an error associated with the calibration of the rotating shaft balance and an error related to the positioning of the wing. Firstly, the calibration of the rotating shaft balance leads to an error in the force measurements. This calibration error is of the order of 0.2 N for the thrust and torque [57].

Secondly, there is a random error, mainly caused by the positioning of the wing. The wing was attached to the floor by two bolts. After attaching the wing to the floor, the wing's trailing edge was aligned with gravity with an alignment laser. Subsequently, the top plate was attached with two bolts. The positioning error is affected by the positioning of the bolt locations, play in the bolts, and torsion of the wing. The bolt location error and play is estimated to lead to a positioning error of approximately 1 mm. Torsion may lead to an extra positioning error of up to approximately 1 mm at the wing's top end. The wing angle of attack is affected most if the bottom plate front and aft holes are displaced in opposite direction, and the top plate holes in the same direction as their bottom plate counterparts. In this case, at the top plate, the front hole is displaced 1 mm, and the aft hole 1 mm in the opposite direction. The front and aft hole are spaced 294 mm axially, so this leads to a maximum angle of attack error of $\sigma\alpha = 0.4°$ and $\sigma\alpha = 0.8°$, at bottom and top wing end, respectively. The error in propeller clearance is maximal if bottom plate front and aft holes are displaced in the same direction, and at the top plate in the same direction as their bottom plate counterpart. In this case, all holes are displaced in the same direction, 1 and 2 mm on bottom and top plate, respectively. The wing span is 1.25 m, so in this case, the error in the clearance at the spanwise location of the propeller axis is approximately $\sigma d = 1.4$ mm, i.e. 0.2% of the wing chord.

After completing the test matrix, all measurements were repeated in random order, thus including repositioning of the wing. As an example of the repeatability error resulting from the wing positioning, Figure 3.10 presents propulsive efficiency scatters with a best fit as a function of advance ratio for three axial propeller positions.

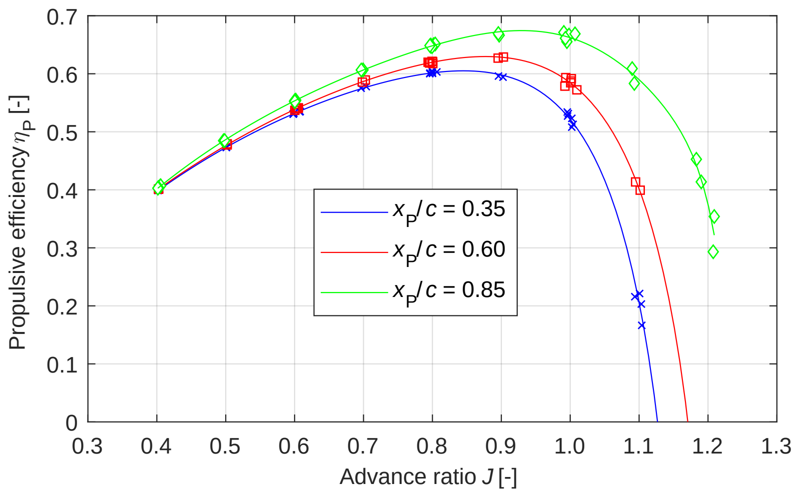

Figure 3.10: Propulsive efficiency scatters versus advance ratio with best fits, found experimentally in Experiment 2, for three axial propeller positions at clearance $d/c = 0.01$.

It can be seen that there are uncertainties in both the advance ratio and the efficiency. Since the advance ratio is set, its error is independent, and it can be characterized by its standard deviation to the mean advance ratio $\bar{J}$, i.e. for n_{meas} measurements:

$$\sigma J = \sqrt{\frac{\sum_i (\bar{J} - J_{\text{meas}_i})^2}{n_{\text{meas}} - 1}}. \tag{3.1}$$

On the other hand, to calculate the errors in thrust, torque and efficiency, it should be noted that they are dependent on the advance ratio. Their errors are thus better represented by its standard deviation to the fitted value, i.e.:

$$\sigma C = \sqrt{\frac{\sum_i (C_{\text{fit}_i} - C_{\text{meas}_i})^2}{n_{\text{meas}} - 1}} \qquad \text{for } C = C_T, C_Q \text{ and } \eta. \tag{3.2}$$

These errors are tabulated for several advance ratios in different configurations in Table 3.4. Generally, errors can be seen to increase with increasing advance ratio. This is a result of minor fluctuations in experimental conditions having an increasingly large effect as the advance ratio increases. Since thrust and torque decrease, but their errors increase with increasing advance ratio, the relative errors in thrust and torque are also increasingly large with increasing advance ratio. The propulsive efficiency is sensitive to this, which leads to increasingly large uncertainties in efficiency as advance ratio increases.

Table 3.4: Errors in Experiment 2 corresponding to the measurements in Figure 3.10.

Configuration	**Advance ratio** σJ [-]	**Thrust** σT [-]	**Torque** σQ [-]	**Efficiency** $\sigma\eta$ [-]
$x_P/c = 0.85$, $J = 0.4$	0.0019	0.0001	0.00003	0.0004
$x_P/c = 0.35$, $J = 0.8$	0.0037	0.0007	0.00015	0.0015
$x_P/c = 0.60$, $J = 1.0$	0.0063	0.0014	0.00011	0.0073
$x_P/c = 0.35$, $J = 1.1$	0.0046	0.0019	0.00016	0.0231
$x_P/c = 0.85$, $J = 1.2$	0.0129	0.0029	0.00020	0.0293

4
Numerical approach

To evaluate the performance over-the-wing propellers in a conceptual design phase, a tool that rapidly accounts for the most important interaction effects is necessary. The aim of the tool is to determine the lift and pressure drag of the wing, as well as propeller thrust and torque. Preliminary results of the experimental study demonstrated that over-the-wing propellers feature significant two-way interactions. Most importantly, the flow above the wing and inflow into the propeller disk are accelerated and changed in direction, which cannot be neglected. Even to model the two-way interaction in the simplest way, an iterative procedure is required due to the close proximity of propeller and wing. Previous studies have shown that the interaction effects are predominantly of potential nature with the flap retracted [11], and thus an inviscid formulation is selected. Furthermore, to reduce computational requirements, it is hypothesized that the unsteady loading on the propeller blades can be represented by means of a steady non-uniform loading distribution on the propeller disk and slipstream. The validity of this hypothesis will be discussed when comparing the results to those of the experimental study.

The numerical model contains three components: the propeller, its slipstream and the wing. A flow diagram of the solver with illustrations of its components is shown in Figure 4.1. A Panel Method is used to represent the wing. The propeller loading can be calculated with a Blade Element Model (BEM). The velocities induced by the wing, obtained from the panel method, are used as input for the modified BEM, from which the time-average distribution of circulation across the propeller disk is obtained. Subsequently, the slipstream is modelled by a vortex lattice model (VLM). Once the circulation distribution and position of the slipstream are known, the velocities induced by the slipstream on the wing are computed, and the system is solved iteratively. After each iteration, the wing- and propeller-induced velocities are compared to their value in the previous iteration. Convergence is attained if their root-mean-square difference is within a requested tolerance.

Aside from developing the solver architecture, the BEM and slipstream VLM are improved compared to earlier projects [18, 27]. These examples assume axisymmetric loading and/or neglect deformation of the slipstream due to wing-induced velocities, which is concluded to be inaccurate for tractor propellers. These effects are even stronger for over-the-wing propellers, due to the close proximity of the propeller to the pronounced velocity field above the wing, and are thus accounted for in the numerical tool. The following sections discuss the panel method, BEM and VLM and the accuracy of the BEM and panel method by comparing their results to wind tunnel data. The accuracy of the complete, coupled model is addressed in Chapter 5, where it is discussed in tandem with the wind tunnel results.

4.1. Panel method

A panel method is suitable for inviscid, incompressible flow around arbitrary shapes. Accordingly, it does not predict friction drag or other boundary layer effects. Albeit relatively complex compared to a vortex lattice method, a panel method was preferred to correctly capture the wing thickness effect. This is especially important due to the close proximity between propeller and wing. More information on panel methods for incompressible flow is given by Katz and Plotkin [59].

To model the wing and nacelle, the existing Fortran-based panel code, FASD (Flow Analysis using Singularity Distributions) [60], is used. This program divides geometries into rectangular panels, on which a source

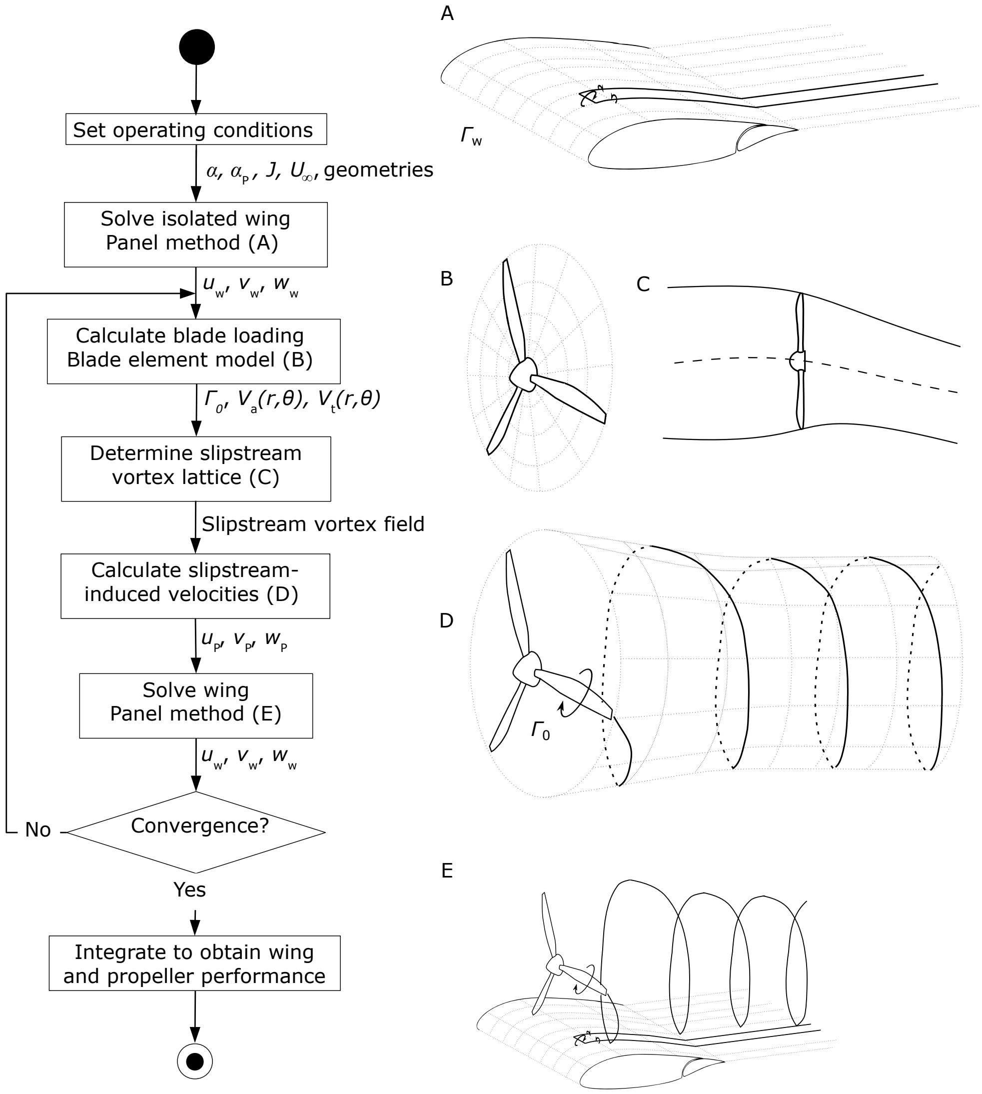

Figure 4.1: Left: flow diagram of the over-the-wing propeller numerical tool. Right: schematic representation of the elements which comprise the numerical model.

and sink are placed. The source and sink strengths are found by setting approppriate boundary conditions, such as tangent flow at body surfaces and no flow inside them. At any desired points, flow properties such as the pressure or velocity can then be requested. As an example of the general setup of the panel method Figure 4.2 illustrates the Experiment 1 simulation panel geometry limited to the spanwise region occupied by the propeller. Velocities are sampled in the propeller disk and vertical slipstream planes, which are used in the BEM and slipstream model respectively.

Aside from the specification of the geometries, which will be discussed in more detail in the following sections, input of the panel method includes the propeller-induced velocities and solver parameters. The propeller-induced velocities are considered by adding them to the freestream velocity. The far wake direction was set in line with the wing angle of attack. The panel method can find the singularity strengths iteratively, or by a direct inversion method. In general, the iterative solution method was faster and thus preferred. The Mach number was set to 0, since the flow speeds in both experiments can be considered to be incompressible at $M = 0.12$ and $M = 0.06$. In the subsequent sections the panel geometries of both experimental simulations are discussed in more detail.

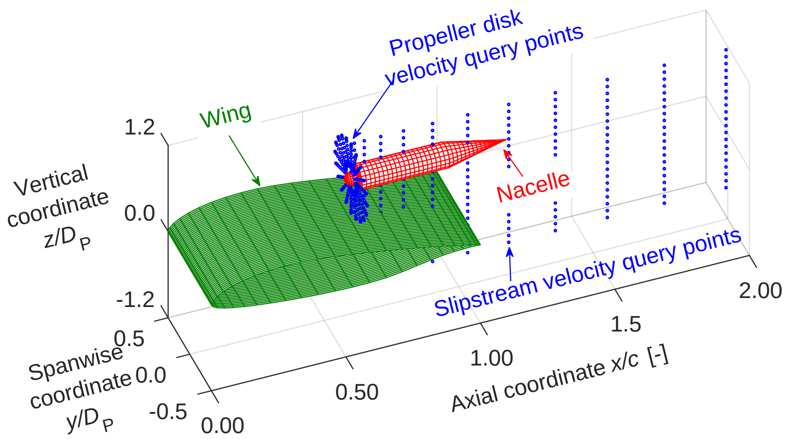

Figure 4.2: Geometric representation of the wing segment located under the propeller disk (green) and nacelle (red) modelled in the panel method, indicating the propeller disk and $y = 0$ slipstream planes where velocities are requested.

4.1.1. GEOMETRIC MODEL OF EXPERIMENT 1

Preliminary results of Experiment 1 showed that the presence of the nacelle had a noticeable effect on wing performance. However, internal memory limitations[1] in the program prevented the simulation of the complete wind-tunnel setup. Thus, the simulation of Experiment 1 was simplified and represented by means of a single nacelle situated above a high aspect ratio, rectangular wing. Figure 4.3 shows the full panel geometry of the simulation of Experiment 1. This simulation features an airfoil with double cosine spacing, i.e. dense paneling at leading and trailing edges. Furthermore, in spanwise direction, the reference area under the propeller and wing ends feature uniform and cosine spacings, respectively. The reference area is most densely paneled, with increasing panel size towards the wing tips. For the nacelle, uniform panel density is used (this can be seen better in Figure 4.2). The velocity query points at the propeller disk correspond to the blade element disk coordinates. The slipstream velocity query points are uniformly spaced in the z-direction, and cosine-distributed axially, to improve the resolution of the slipstream plane velocities near the wing and propeller disk.

4.1.2. GEOMETRIC MODEL OF EXPERIMENT 2

Figure 4.4 presents the panel model used to simulate the Experiment 2 numerically. It is necessary to model the nacelle, since it is expected to have a considerable effect on the flow field. Again, it is impossible to model the full wind tunnel geometry, but in this case simplifying to a rectangular wing is incorrect, since there are significant wing tip effects. Accordingly, the wing and top plate are modelled, as well as a floor plate. The floor plate extends 1.35 chord-lengths in axial direction in front of and aft of the leading and the trailing edges of the wing, respectively. It extends 1.35 chord-lengths above and below the wing leading edge in z-direction. The wing, nacelle and velocity request planes feature similar panel distributions to the simulation of Experiment 1. Panels on the strut were spaced in a cosine distribution in y-direction, with denser panelling near the nacelle and walls. In x-direction, the strut employed a double cosine distributions, i.e. denser at its leading and trailing edges.

The geometry was slightly adapted from the experimental setup, since panels normal to the flow at the nacelle and at the end plates prevented convergence. In these locations, fairings were applied. Furthermore, the top end plate was rotated together with the wing in the experiment, but this also prevented solver convergence. This is presumably caused by flow that would have separated in reality. Accordingly, in the simulations, the top end plate was aligned with the flow.

4.1.3. VALIDATION OF THE PANEL METHOD

Isolated wing pressure distributions are shown in Figure 4.5, as measured in Experiment 1 and simulated in the panel method. With the flap retracted, the panel method shows good agreement with the wind tunnel results. However, when it is deflected, the panel method presents unrealistic results in the cove of the main element, even if the kink on the lower side of the airfoil is smoothed (NLF-MOD22A, see Figure A.1). This is

[1]The internal memory limitations were resolved at a later stage, allowing the larger number of panels in the simulation of Experiment 2.

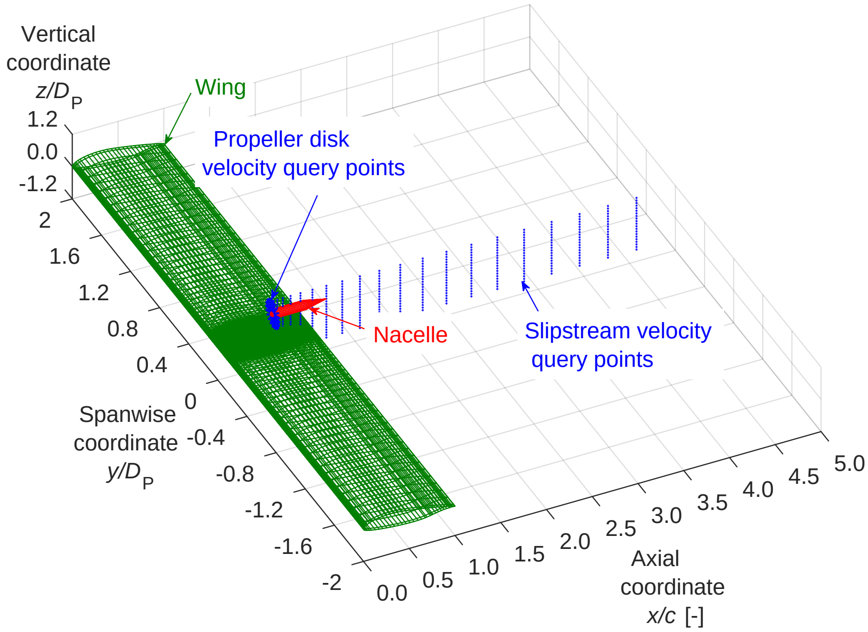

Figure 4.3: Full view of the geometric representation in the simulation of Experiment 1, with components indicated.

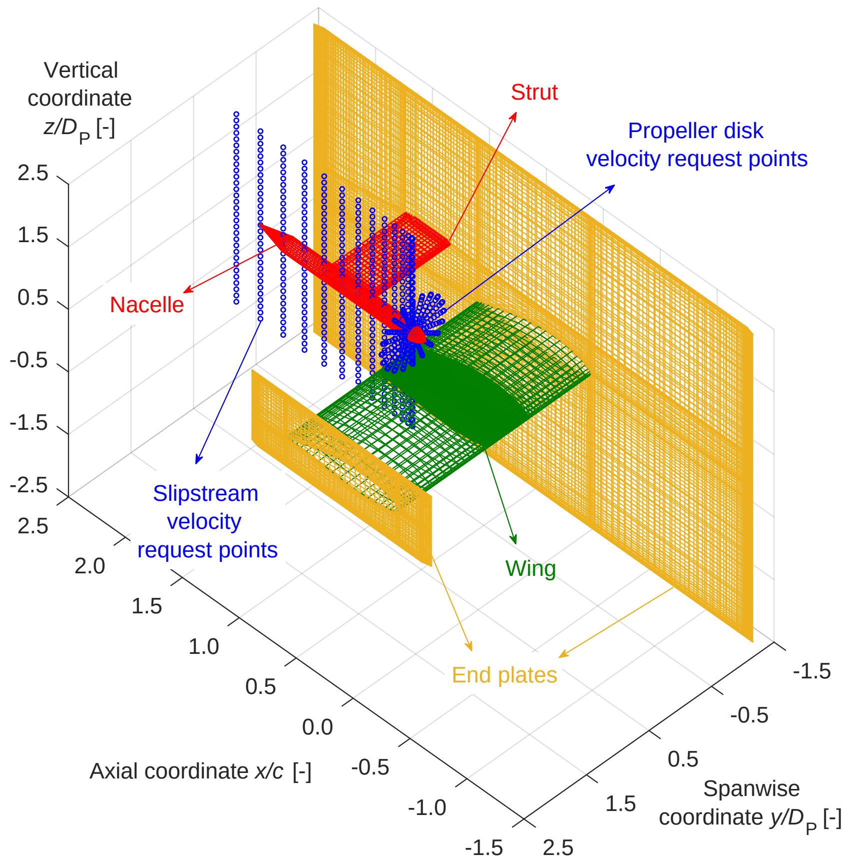

Figure 4.4: The geometric representation in the simulation of Experiment 2, with components indicated. Note that as opposed to convention, the flow is coming from the right in this figure to present a better view.

due to the incapability of panel methods to model regions with significant viscous effects or recirculation. To obtain some numerical results on a high-lift configuration, an attempt was made to simulate the NLR-7301 airfoil with flap, which has limited viscous effects [61]. However, the panel method did not converge at the main element trailing edge, supposedly due to the strong flow interaction there. Accordingly, the results for the high-lift configuration will be limited to Experiment 1.

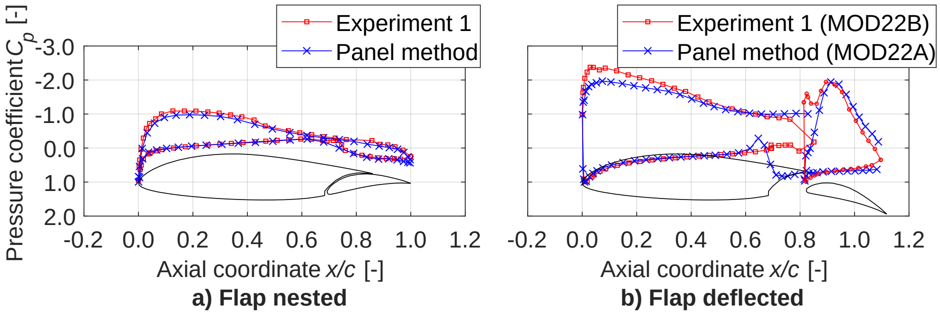

Figure 4.5: Isolated wing pressure distributions in Experiment 1, found experimentally and numerically.

Figure 4.6 presents the static pressures at the locations in Experiment 2 indicated in Figure 3.9a, as found experimentally and numerically. Agreement is acceptable, although FASD underestimates the pressure coefficient for all but one point. This is a result of the omission of the boundary layer, which generally has a decambering effect, leading to a lower effective angle of attack [18].

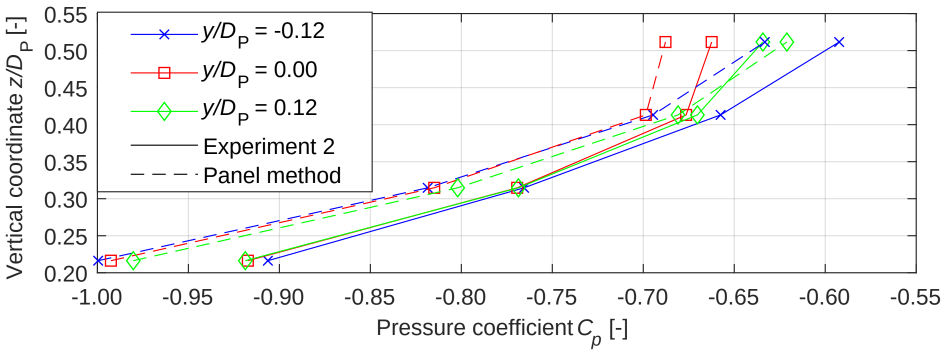

Figure 4.6: Static pressure samples at three spanwise locations y/D_P in Experiment 2, found experimentally and numerically.

4.2. BLADE ELEMENT METHOD

A blade element method is a rapid computational scheme to determine the forces on a propeller, which divides the propeller disk into elements. On each element, the local blade velocities are computed and used to find the blade element loading. The disk is assumed to be continuous and interaction between blades is neglected, which is also done in this method. Traditional blade element methods divide the propeller disk into only radial elements. Since the inflow is non-uniform, the BEM was adapted to also divide the disk into azimuthal elements.

Figure 4.7 illustrates the method that was developed taking account of the non-uniform wing-induced velocity distribution at the propeller disk. First, the propeller blade is divided into n_r radial elements. Each element is defined by its chord length c_b, geometric pitch angle β, radial coordinate r, radial length dr and airfoil shape. Figure 4.7a shows an example of such a radial element. Subsequently, the propeller disk is simplified to be continuous, and also divided into n_θ azimuthal elements, which is shown in Figure 4.7b, with a blade element at coordinates (r_0, θ_0) indicated.

To determine the blade element loading, its velocity diagram will be constructed to determine its angle of attack. Figure 4.7c presents the blade element in the stream coordinate system. Note that the propeller is rotated around the y-axis at an angle of attack α_P. The inflow to the blade element consists of the freestream plus wing-induced velocities, which are generally dependent on the blade element's position, i.e. the inflow vector is $(U_\infty + u_\mathrm{w}, v_\mathrm{w}, w_\mathrm{w})$ in the stream coordinate system. To determine the blade angle of attack, this vector must be transformed to find the axial and tangential velocities in the blade element disk coordinate system. In Figure 4.7d, the velocities in the (x,z)-plane are decomposed onto the propeller disk. The sketched velocities are equal to:

$$V_{\mathrm{t},1} = (U_\infty + u_\mathrm{w})\sin\alpha_\mathrm{P} + w_\mathrm{w}\cos\alpha_\mathrm{P}, \tag{4.1}$$

$$V_{\mathrm{a},1} = (U_\infty + u_\mathrm{w})\cos\alpha_\mathrm{P} - w_\mathrm{w}\sin\alpha_\mathrm{P}. \tag{4.2}$$

$V_{\mathrm{a},1}$ is the axial inflow velocity that was sought, but $V_{\mathrm{t},1}$ is further decomposed in Figure 4.7e. Only the drawn tangential velocity $V_{\mathrm{t},2}$ is of interest, which is equal to:

$$V_{\mathrm{t},2} = v_\mathrm{w}\cos(\theta - \frac{\pi}{2}) - V_{\mathrm{t},1}\cos(\pi - \theta) \tag{4.3}$$

$$= -v_\mathrm{w}\sin\alpha_\mathrm{P} + \Big((U_\infty + u_\mathrm{w})\sin\alpha_\mathrm{P} + w_\mathrm{w}\cos\alpha_\mathrm{P}\Big)\cos\theta. \tag{4.4}$$

To the axial and tangential inflow velocities $V_{\mathrm{a},1}$ and $V_{\mathrm{t},2}$, the rotational velocity and propeller-induced axial and tangential velocities $V_{\mathrm{a,i}}$ and $V_{\mathrm{t,i}}$, respectively, should be added. This leads to the velocity diagram depicted in Figure 4.7f. Summing all mentioned tangential and axial velocities leads to the effective velocity as seen by the blade element, V_eff. Usually, the propeller-induced velocities are expressed as axial and tangential acceleration factors, a and b, respectively. This leads to the following axial and tangential blade velocities:

$$V_\mathrm{a} = \Big(\Big(U_\infty + u_\mathrm{w}(r_0,\theta_0)\Big)\cos(\alpha_\mathrm{p}) - w_\mathrm{w}(r_0,\theta_0)\sin(\alpha_\mathrm{p})\Big)(1+a), \tag{4.5}$$

$$V_\mathrm{t} = \Big(\Omega r_0 + \Big(U_\infty + u_\mathrm{w}(r_0,\theta_0)\Big)\sin(\alpha_\mathrm{p}) - w_\mathrm{w}(r_0,\theta_0)\cos(\alpha_\mathrm{p}) - v_\mathrm{w}(r_0,\theta_0)\sin(\theta_0)\Big)(1-b). \tag{4.6}$$

Note that the acceleration factors a and b are unknown as of yet. It will be shown how to compute them iteratively. The blade element has a geometric pitch angle β, and the inflow angle with respect to the disk plane can be seen to be $\phi = \arctan\frac{V_\mathrm{a}}{V_\mathrm{t}}$, leading to an effective angle of attack $\alpha = \beta - \phi$.

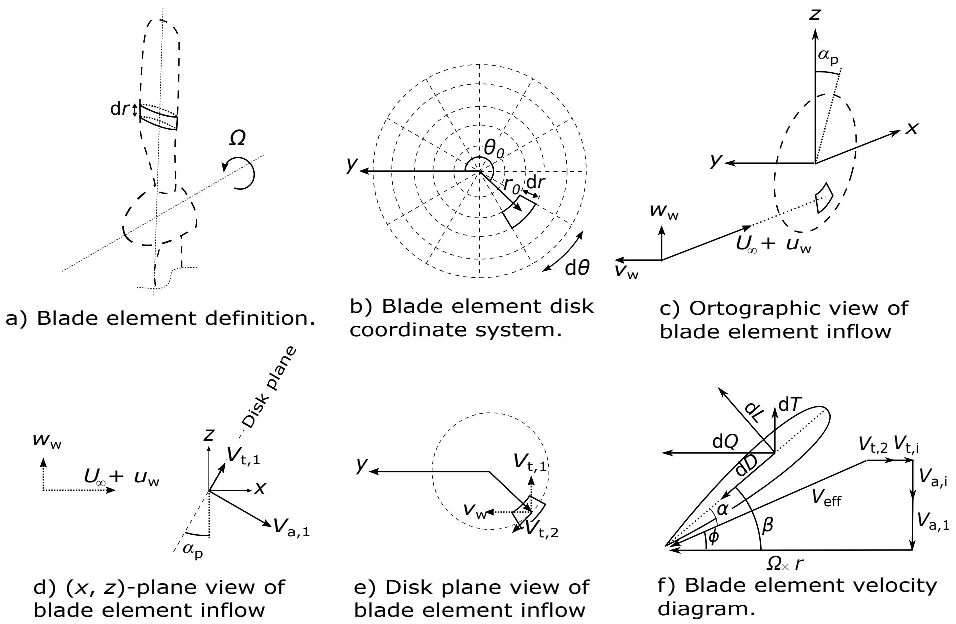

Figure 4.7: Determination of the blade element velocity diagram.

Using two-dimensional airfoil polars corresponding to the blade element, the lift and drag forces dL and dD acting on it can be found. The polars are created using XFOIL using the blade geometry [62]. The lift and drag coefficients are then corrected for three-dimensional [63] and compressibility [64] (valid up to Mach number 0.9) effects, and hub and tip loss factors [65] are applied. A detailed explanation of these corrections can be found in Appendix E. For a propeller, it is more convenient to project these forces onto the propeller plane and axis, leading to a thrust dT and torque dQ:

$$\begin{aligned} \mathrm{d}T &= \mathrm{d}L \cos\phi - \mathrm{d}D \sin\phi, && (4.7) \\ \mathrm{d}Q &= r(\mathrm{d}L \sin\phi + \mathrm{d}D \cos\phi). && (4.8) \end{aligned}$$

Considering conservation of axial and angular momentum, these forces can be related to the acceleration factors a and b [65]:

$$\begin{aligned} a &= \frac{\mathrm{d}T}{4\pi r \rho U_\infty^2 (1+a)\,\mathrm{d}r\,\mathrm{d}\theta}, && (4.9) \\ b &= \frac{\mathrm{d}Q}{4\pi r^3 \rho U_\infty (1+a)\, 2\pi n\,\mathrm{d}r\,\mathrm{d}\theta}. && (4.10) \end{aligned}$$

a and b can be determined iteratively. First, an initial value must be chosen. Subsequently, by evaluating Equations 4.5 through 4.11 the thrust and torque on the blade element can be found. The chosen values can be inconsistent with the results of Equation 4.9. If so, a new iteration is started, where typically the new values are taken as a mean of the input and output values to smooth the iteration.

After convergence, the total thrust and torque on the propeller can be found by a summation over all blade elements:

$$T = \int B\,\mathrm{d}r\,\mathrm{d}\theta\,(\mathrm{d}L\cos\phi - \mathrm{d}D\sin\phi) \tag{4.11}$$

$$Q = \int B\,r\,\mathrm{d}r\,\mathrm{d}\theta\,(\mathrm{d}L\sin\phi + \mathrm{d}D\cos\phi) \tag{4.12}$$

in which B is the number of blades. The propeller power is equal to $P = 2\pi Q$, its efficiency is:

$$\eta = \frac{TU_\infty}{2\pi Q}. \tag{4.13}$$

If desired, the normal and side forces can be found by relating them to the torque and integrating them:

$$N = \int \frac{\mathrm{d}Q}{r}\cos\theta = \int\int B\,dr\,\cos\theta\,d\theta\,(\mathrm{d}L\sin\phi + \mathrm{d}D\cos\phi) \tag{4.14}$$

$$Y = \int \frac{\mathrm{d}Q}{r}\sin\theta = \int\int B\,dr\,\sin\theta\,d\theta\,(\mathrm{d}L\sin\phi + \mathrm{d}D\cos\phi) \tag{4.15}$$

The BEM-computed axial and tangential acceleration factors and circulation distribution at the propeller disk are given as input to the slipstream VLM. Furthermore, propeller performance parameters are returned as output once the numerical method has terminated its iterations.

4.2.1. MODELLING AND VALIDATION OF ISOLATED PROPELLERS

Three propellers were modelled in this thesis: the Beaver DHC-2 and XPROP propellers used in Experiment 1 and Experiment 2, respectively, and a propeller used in experiments by McLemore [66]. The first two propellers were modelled to simulate the corresponding experiments numerically, whereas McLemore's propeller will be used to validate the BEM for propellers at an angle of attack. Propeller blade section lift and drag polars were created using XFOIL [62]. The blade chord, pitch and thickness distributions for the three propellers can be found in Figure B.1.

The section data of the Beaver propeller can be found in Appendix B. The polars are based on a constant NACA 64A416 blade section at a Reynolds number of $2\cdot10^5$, chosen to achieve agreement with experimental results. Note that the blade root is of cylindrical shape. Accordingly, near the blade root, lift and drag coefficients were interpolated between the NACA polar and the lift and drag of a cylinder at $Re = 2\cdot10^5$, namely $C_L = 0$ and $C_D \approx 1$ [67]. Figure 4.8 presents the radial total-pressure distribution and the thrust coefficient versus advance ratio curve of the uninstalled propeller, as found in earlier experiments [54], and as computed

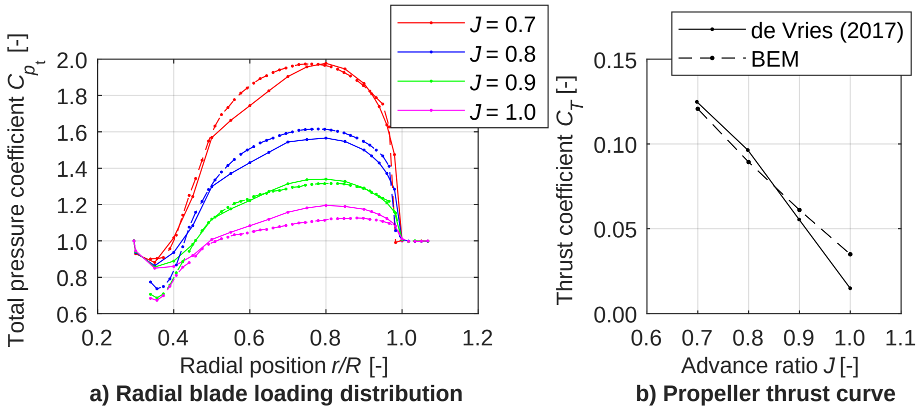

Figure 4.8: Radial blade loading distribution and thrust coefficient versus advance ratio of the isolated Beaver propeller. Results obtained from earlier experiments [54] are compared to those computed using the BEM.

by the BEM. The BEM slightly underpredicts thrust at low advance ratio, and overestimates it at high advance ratio, due to Reynolds number effects which are not modelled.

Appendix B contains the XPROP blade sections and their lift and drag polars. These are based on the ARA-D and -A sections, at a Reynolds number of $5 \cdot 10^4$, chosen to achieve agreement with experimental results. The results of the BEM are shown in Figure 4.9 and compared to the findings of Experiment 2. At low advance ratio, thrust estimation is in good agreement, while torque and propulsive efficiency are slightly over- and underestimated, respectively, by the BEM. At high advance ratio, thrust is significantly and torque is slightly overestimated. This leads to a sizeable disagreement in the estimated propeller efficiency at high advance ratio. Similarly to the Beaver propeller modelling, this is due to Reynolds number effects which were not modelled.

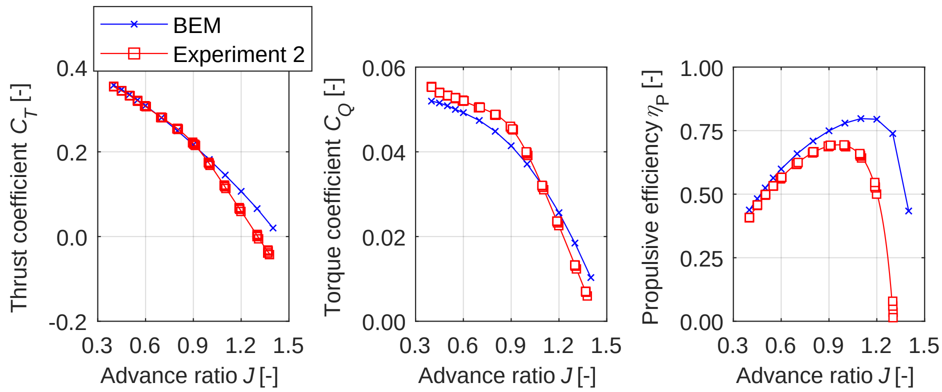

Figure 4.9: Thrust and torque coefficients and propulsive efficiency of the isolated XPROP propeller. Experiment 2 results are compared to those computed using the BEM.

The final propeller that was modelled was used to validate the BEM for propellers at angle of attack. For this reason, a propeller used by McLemore [66] during an extensive experimental study concerning the propeller performance at angle of attack, was chosen. The section data of this propeller are shown in Appendix B. Note that the blade section polars have a limited angle of attack range, since they have a sharp leading-edge stall, which was not possible to capture accurately using XFOIL. For moderate advance ratio, this does not present any problems, but it was not possible to model the propeller at very low or high advance ratios.

Figure 4.10 contains the thrust and normal force coefficients of the propeller at an angle of attack of 15° as a function of advance ratio. Results are according to McLemore's experiments and the BEM simulation. For both the propeller thrust and normal force, the qualitative agreement is good, but at low advance ratio, thrust is overestimated for both pitch settings. Furthermore, the normal force for all advance ratios and the thrust at high advance ratio are underestimated at the higher pitch setting. This is however caused by the limited

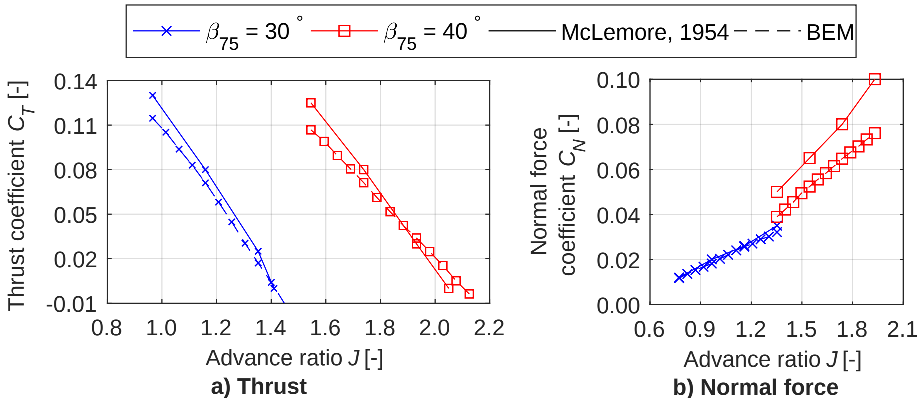

Figure 4.10: Thrust and normal coefficients for a propeller at an angle of attack of 15°, according to McLemore [66] and the BEM simulations, at two blade pitch settings.

blade section polars and Reynolds number effects, and there is no reason to assume that the angle of attack method modelled by the BEM is erroneous.

4.3. SLIPSTREAM VORTEX LATTICE

The propeller blade can be represented as a lifting line, whose trailing vortex system is constituted of a distribution of horseshoe vortices with a circulation strength equal to the one determined with the BEM. This leads to a helical lifting line sheet behind the propeller blade. Vorticity is largely concentrated at the blade root and tip [68], leading to root and tip vortices as illustrated in Figure 4.11. For a uniformly loaded propeller, averaged over the propeller blade positions in a full propeller rotation, this leads to an axisymmetrical cylindrical vorticity surface, with a vortex line at its center.

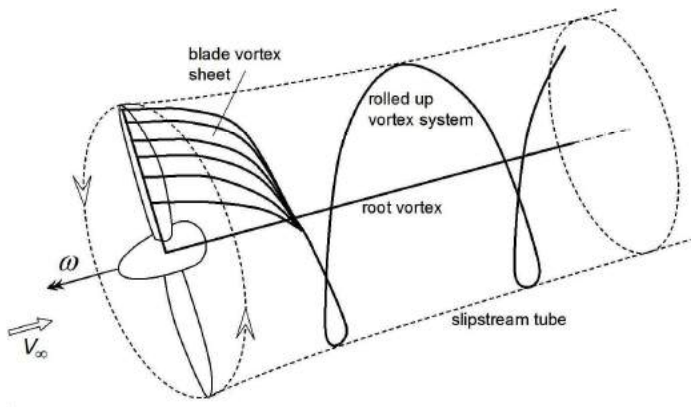

Figure 4.11: Illustration of the vortex system behind a uniformly loaded propeller, reproduced from Veldhuis [18].

For tractor propellers, wing-induced velocities at the propeller disk are limited, and it is acceptable to consider the slipstream surface to be axisymmetric, although earlier studies conclude that this does limit the applicability and accuracy of the numerical model [18, 27]. For over-the-wing propellers, the strong non-uniform inflow does not allow the simplification of an axisymmetric slipstream surface to be made. Furthermore, the non-uniform inflow will cause the blade circulation to depend not only on its radial, but also azimuthal position. Accordingly, the circulation changes as a function of time and vortices must be shed in the blade wake to satisfy Kelvin's circulation theorem.

In the propeller blade reference frame the unsteady loading will lead to periodic, time-dependent vortex shedding. However, in an intertial reference frame, assuming a continuous propeller disk, this leads to a steady, spatially-periodic distribution of shed vortices. The geometry of this distribution is determined by assuming the slipstream to be a quasi-cylindrical tube which is deformed due to contraction and the presence of a wing-induced flow field. During the geometry generation, slipstream deformation due to the radial variation in propeller axial acceleration factor and wing-induced velocities will be accounted for.

It should be noted that this method of representing the slipstream leads to two inconsistencies. Firstly fixing both the vortex circulation strengths and their geometric distribution, flow tangency at the outer slipstream boundary may be violated. This inconsistency can only by avoided by a free wake model, which was not chosen in order to limit computational cost. Additionally, the propeller-induced velocities at the propeller disk as calculated by the BEM may not match what the slipstream VLM would predict. It is not possible to quantify this discrepancy, since the use of vortex singularities in the VLM does not allow a meaningful calculation of velocities in the disk plane. It is however expected that this inconsistency is minor, since the bound vortex segments in the disk planes will cause the strongest velocities in this plane, and their strengths were determined by the BEM.

Furthermore, the interaction between the slipstream and the nacelle is not fully modelled. Although the induced velocities provided by the panel method include nacelle-induced velocities that are accounted for in the geometric construction of the slipstream, other interaction effects are not modelled. For example, the slipstream surface can intersect the nacelle, and viscous interaction of the slipstream close to the nacelle surface is omitted.

The generation of the slipstream geometry is shown in Figure 4.12. Consider a generic helical vortex line trailing a blade element, as sketched in Figure 4.12a. Figure 4.12c illustrates the determination of the circulation strengths of this vortex line. The bound vortex on the blade element is located on the blade and has a circulation Γ_0, as determined by the BEM. If Δt is the time step of a series of time intervals, then the j-th horseshoe vortex in the wake of the propeller blade will have been shed an time $j\Delta t$ earlier. At this time intant, the blade element had angular coordinate $\theta_0 + j\Omega\Delta t$ and a corresponding circulation $\Gamma_j = \Gamma(r_0, \theta_0 + j\Omega\Delta t)$. Since Kelvin's theorem demands that vorticity must be conserved, when a new bound vortex is created, the blade element must shed a vortex with equal strength, but opposite direction in its wake, so $\Gamma_j = \Gamma(r, \theta_0 + j\Omega\Delta t) - \Gamma_{j-1}$ for $j > 0$.

The position vector of this wake vortex can be determined iteratively, as depicted in Figure 4.12d. The position of vector of the vortex with index j (for $j > 0$) is equal to the position vector of the horseshoe vortex with index $j-1$ and coordinates $(x_{j-1}, y_{j-1}, z_{j-1})$, plus:

1. the axial slipstream displacement in the interval Δt, $\Delta x = V_\mathrm{a}\dfrac{1+s}{1+a}\Delta t$,
2. the slipstream deflection due to a propeller angle of attack, Δz,
3. the azimuthal displacement of the slipstream helix, $\Delta\theta = \dfrac{V_\mathrm{t}}{r}\Delta t$,
4. the slipstream contraction, Δr,
5. the wing-induced movement, $(\Delta x_\mathrm{w}, \Delta z_\mathrm{w}) = \Big(u_\mathrm{w}(x_{j-1}, z_{j-1}), w_\mathrm{w}(x_{j-1}, z_{j-1})\Big)\Delta t$[2],

The contraction Δr and acceleration factor, s, are determined following the method of Rwigema [65]. The deflection due to a propeller angle of attack is found with empirical relations by de Young [69]. The used equations can be found in Appendix F. The axial and tangential velocities V_a and V_t are supplied by the BEM, whereas the wing-induced velocity field is given as output by the panel method.

Starting at the bound vortex, the vortex locations and strengths can be determined sequentially until the desired number of axial slipstream elements is reached. Doing this for all radial blade elements leads to the slipstream vortex lattice shown in Figure 4.12b. The resulting vortex lattice can be regarded as a combination of formerly bound[3] and tangential vortex segments, respectively $\Gamma_{\mathrm{b}ji}$ and $\Gamma_{\mathrm{t}ji}$. The indexes i and j refer to the radial and axial segment number, respectively. It was already demonstrated that the bound vortex strengths are equal to:

$$\Gamma_{\mathrm{b}ji} = \begin{cases} \Gamma(r_i, \theta_0), & \text{if } j = 0, \\ \Gamma(r_i, \theta_0 + j\Omega\Delta t) - \Gamma_{\mathrm{b}(j-1)i}, & \text{if } j > 0. \end{cases} \tag{4.16}$$

To determine the trailing segment vortex strengths, Figure 4.12e shows how the vortex lattice is built up from horseshoe vortices. The trailing segments of the horseshoe vortices extend to infinity, since Helmholtz'

[2]The spanwise variation and spanwise wing-induced velocities were found to be small, and as such it was chosen to neglect them.
[3]Technically, the radial vortices are not bound, but shed, but they will be referred to as bound for simplicity's sake.

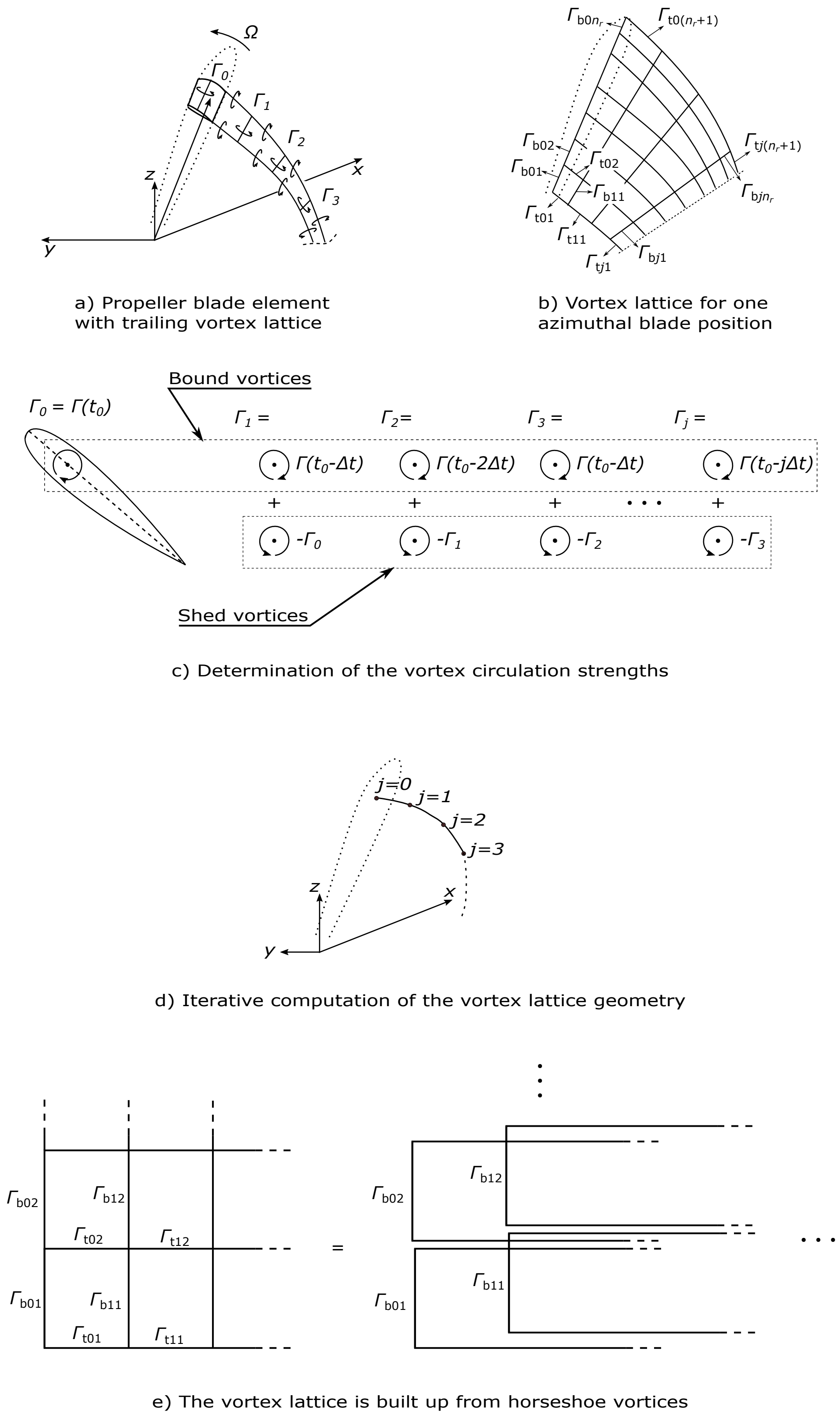

Figure 4.12: Illustrations concerning the generation of the slipstream vortex lattice.

theorem states that vortices cannot end in a fluid. Accordingly, the tangential segment strengths are a summation of horseshoe vortex ends (i) adjoining in radial direction and (ii) lying on top of each other in axial direction. As a result, for $j = 0$:

$$\Gamma_{\mathrm{t}0i} = \begin{cases} -\Gamma_{\mathrm{b}01}, & \text{if } i = 1, \\ \Gamma_{\mathrm{b}jn_r}, & \text{if } i = n_r + 1, \\ \Gamma_{\mathrm{b}ji} - \Gamma_{\mathrm{b}j(i-1)}, & \text{otherwise.} \end{cases} \tag{4.17}$$

Subsequently, the tangential vortex segments strengths for $j > 0$ can be computed:

$$\Gamma_{\mathrm{t}ji} = \begin{cases} \Gamma_{\mathrm{t}(j-1)i} - \Gamma_{\mathrm{b}j1}, & \text{if } i = 1, \\ \Gamma_{\mathrm{t}(j-1)i} + \Gamma_{\mathrm{b}jn_r}, & \text{if } i = n_r + 1, \\ \Gamma_{\mathrm{t}(j-1)i} + \Gamma_{\mathrm{b}ji} - \Gamma_{\mathrm{b}j(i-1)}, & \text{otherwise.} \end{cases} \tag{4.18}$$

After constructing this vortex lattice for all azimuthal blade element positions, n_θ quasi-helicoidal vortex surfaces have been created. The propeller-induced velocities at the wing can then be computed with Biot-Savart's law. The propeller-induced velocities $\vec{V}_{\mathrm{P},i}$ at a point with location vector $\vec{g}$ equal:

$$\vec{V}_{\mathrm{P},i} = \sum_{j=0}^{n_x} \sum_{k=1}^{n_\theta} \left(\sum_{i=1}^{n_r} \frac{\Gamma_{\mathrm{b}ijk}}{4\pi} \frac{\vec{dl}_{\mathrm{b}ijk} \times (\vec{g} - \vec{g}_{\mathrm{b}ijk})}{|\vec{g} - \vec{g}_{\mathrm{b}ijk}|^3} + \sum_{i=1}^{n_r+1} \frac{\Gamma_{\mathrm{t}ijk}}{4\pi} \frac{\vec{dl}_{\mathrm{t}ijk} \times (\vec{g} - \vec{g}_{\mathrm{t}ijk})}{|\vec{g} - \vec{g}_{\mathrm{t}ijk}|^3} \right). \tag{4.19}$$

This a summation over all bound and tangential vortex segments, numbering n_x in axial direction, n_θ azimuthally and n_r or $n_r + 1$, respectively, in radial direction. Radial and tangential vortex segments are defined by their strength Γ_b and Γ_t, direction vector $\vec{dl}_\mathrm{b}$ and $\vec{dl}_\mathrm{t}$ and position $\vec{g}_\mathrm{b}$ and $\vec{g}_\mathrm{t}$, respectively. The found velocities are then used as input for FASD to capture the influence of the propeller on the wing. This is done by adding them as a velocity increment on each panel.

4.4. LIMITATIONS OF THE NUMERICAL MODEL

Four aspects of the numerical method limit its applicability. Firstly, the BEM compressibility model is limited to propeller blade Mach numbers of up to 0.9. Secondly, the accuracy and scope of the BEM is strongly dependent on accurate blade section polars and their angle of attack range. Thirdly, the inviscid nature of the panel method does not allow the modelling of wings where significant viscous effects are present, such as the high-lift configuration depicted in Figure 4.5b, or the aft-facing surface on the top plate in Experiment 2. Lastly, the use of discrete vortices to represent the slipstream prohibits any meaningful determination of induced velocities inside the slipstream. This prevents convergence for propeller positions near the leading edge, for which the slipstream geometry intersects with the wing surface. Implementing Rankine vortices, in which velocities linearly decrease to zero within a viscous vortex core [70] could solve this, numerically. It is however unknown how the slipstream is deformed very close to the wing, and any interaction with the boundary layer would be neglected.

4.5. SOLVER ARCHITECTURE AND CONVERGENCE

Discretisation of the wing, slipstream, and propeller disk also have an important effect on the results. A convergence study is shown in Figure 4.13. In this figure, the lift coefficient of a simulation is compared to the converged lift coefficient $C_{L_\mathrm{converged}}$. The wing lift coefficient has converged within 0.1% for 10 radial blade/slipstream elements n_r, 20 azimuthal blade/slipstream elements n_θ, 200 axial slipstream elements n_x, and modelling of the slipstream up to 2.5 chord-lengths behind the propeller disk. The number of chord- and spanwise wing panels were limited to $n_\mathrm{s} = 50$ and n_y 125 respectively (note that Figure 4.13 shows only the spanwise convergence for the panels on the reference area), for which the wing lift coefficient had converged to within 1%. For future studies, a higher panel density is recommended. With this number of panel and slipstream elements, the numerical tool typically requires three to four iterations. It finishes a complete simulation in approximately ten minutes using a single core on a personal laptop.

Figure 4.14 presents an N^2-diagram of the numerical solver architecture. Along the diagonal, the solver functions are placed. Input is given vertically, while output is distributed horizontally. At the top, a list of the user input is given. The solver contains three functions. Firstly, the panel method is run for the isolated wing, to obtain the isolated wing pressure distribution and performance parameters. Subsequently, the panel method for the wing and nacelle is run, starting the iterative process. Again, the wing pressure distribution and performance parameters are stored, to obtain the installation effects. The output wing-induced velocities at the propeller disk and slipstream planes are given as output to the BEM and slipstream VLM, respectively. The BEM is then executed, to obtain the propeller performance parameters and disk loading distribution. Additionally, the propeller disk axial and tangential acceleration factor and circulation distributions are computed and given as input to the slipstream VLM. Lastly, the propeller-induced velocities at the wing are determined by the VLM, and a new iteration is started by giving these as input to the panel method.

This loop is iterated until convergence is attained. Convergence of the numerical method is based on (i) wing-induced velocities at the propeller disk $\boldsymbol{u}_{\mathrm{w_i}}$, $\boldsymbol{v}_{\mathrm{w_i}}$ and $\boldsymbol{w}_{\mathrm{w_i}}$ and (ii) propeller-induced velocities at the wing $\boldsymbol{u}_{\mathrm{P_i}}$, $\boldsymbol{v}_{\mathrm{P_i}}$ and $\boldsymbol{w}_{\mathrm{P_i}}$. If the average, root-mean-square difference between their values after the latest and penultimate iteration (designated by '*') is within a user-set tolerance ϵ, i.e. if:

$$\sqrt{\frac{\sum\left(\boldsymbol{a}_{\mathrm{w_i}}-\boldsymbol{a}^*_{\mathrm{w_i}}\right)^2}{n_r n_\theta}} < \epsilon, \text{ for } \boldsymbol{a}=\{\boldsymbol{u},\boldsymbol{v},\boldsymbol{w}\} \text{ and} \tag{4.20}$$

$$\sqrt{\frac{\sum\left(\boldsymbol{a}_{\mathrm{P_i}}-\boldsymbol{a}^*_{\mathrm{P_i}}\right)^2}{n_{\mathrm{s}} n_y}} < \epsilon, \text{ for } \boldsymbol{a}=\{\boldsymbol{u},\boldsymbol{v},\boldsymbol{w}\}, \tag{4.21}$$

then the iterations are terminated. n_{s} and n_y are the number of points specified along the airfoil and span, respectively, where propeller-induced velocities are calculated. The solver was programmed in MATLAB; the resulting code can be found in Appendix G.

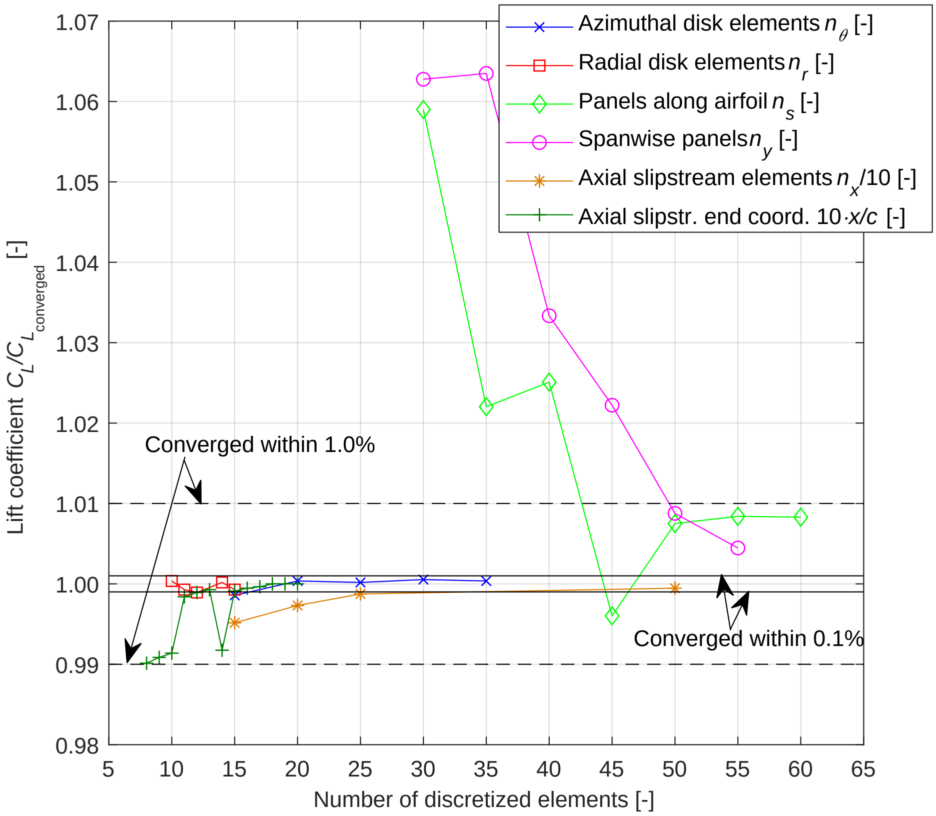

Figure 4.13: Numerical tool discretisation element convergence study.

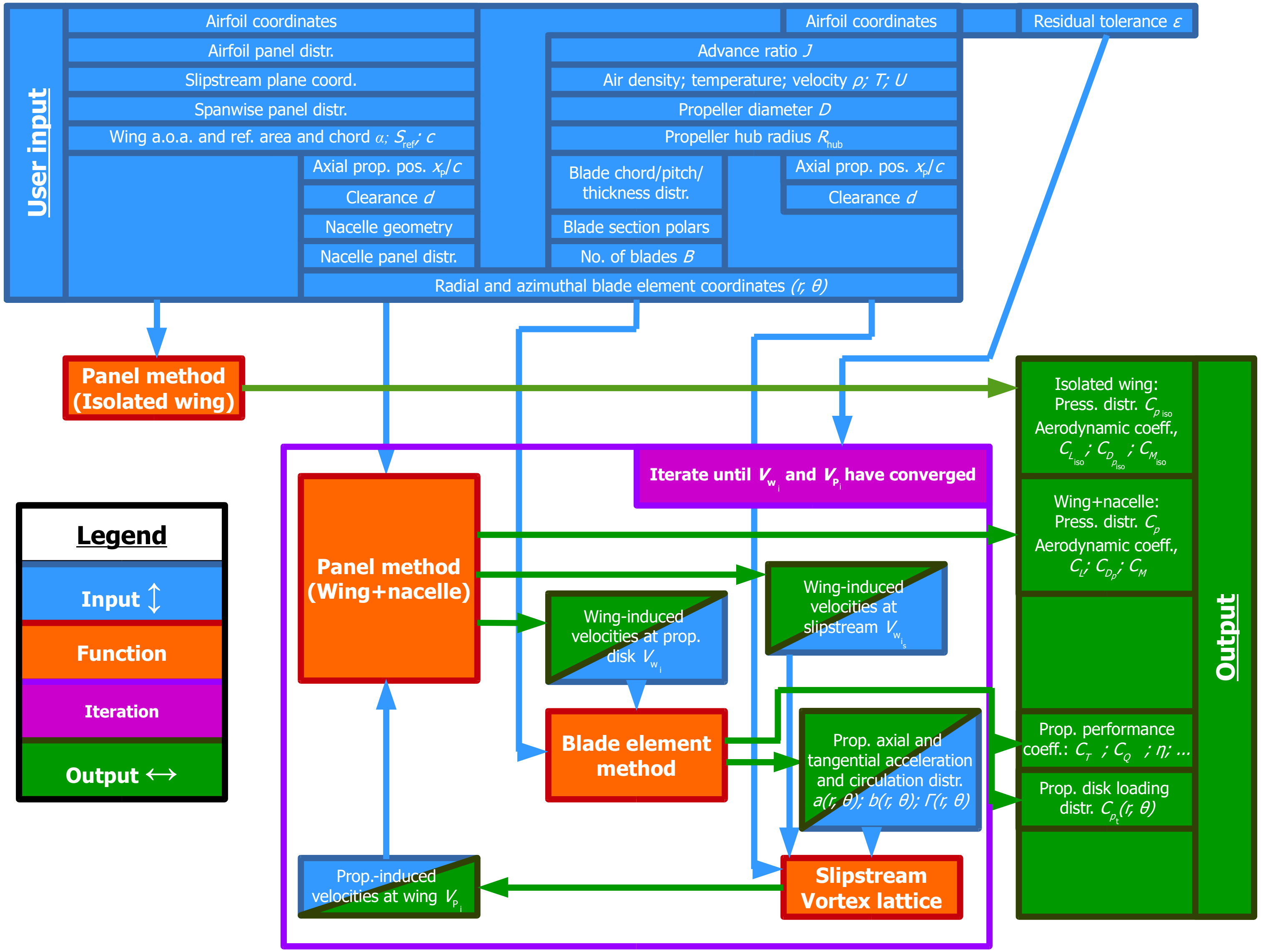

Figure 4.14: N^2-diagram of the numerical solver architecture.

III

Results

5

Performance in cruise conditions and numerical validation

In this chapter, the cruise configuration results are shown. In these configurations, the flap is nested for a moderate lift coefficient ($C_L \approx 0.5$), and the performance of the wing should be optimized in terms of lift-to-drag ratio. The first objective is to study the aerodynamic interaction effects. Secondly, it will be assessed if the numerical model is capturing them correctly. To begin with, the nacelle effects on the wing are shown. Subsequently, the propeller effects on the wing are presented and lastly the wing effects on the propeller.

5.1. Nacelle effects on the wing

The propeller effects can be divided into pressure changes due to the presence of the nacelle (δC_p) and the propeller (ΔC_p). First, the effect of the nacelle and its installation will be shown. Figure 5.1 presents the pressure coefficient difference between the propeller-off and isolated-wing measurements, i.e. $\delta C_p = C_{p_{\text{prop. off}}} - C_{p_{\text{iso}}}$, in the cruise configurations of Experiment 1. The flow goes from left to right, and the spanwise coordinate $y/D_{\text{P}} = 0$ corresponds to the location of the propeller axis.

On the wing upper surface, pressures are increased and decreased, upstream and downstream of the propeller disk location, respectively. This is a result of the flow expanding around the nacelle. In Figure 5.1a, it can be seen that the region of increased pressure extends to the wing leading edge, while the pressure decreases most approximately $0.1 \cdot c$ aft of the propeller disk location. Figure 5.1c shows that the pressure differences are smaller in Configuration 2, but that a larger region of the wing is affected by the upstream pressure increase. Effects of the nacelle on the wing lower surface are negligible in both configurations. Figures 5.1b and d show that in the numerical simulation, the installation effect is weaker than in Experiment 1. This can be attributed to the absence of the sting in the numerical model. Moreover, as opposed to the flow being confined between the wind tunnel walls, it is able to fully expand.

Table 5.1 presents the isolated wing and propeller-off lift, drag and pitching moment coefficients for the cruise configurations of Experiment 1. The nacelle blockage effect generally led to additional pressure drag in both configurations, given that the nacelle is above the rearwards-facing part of the wing surface. For the nacelle position near the trailing edge (Configuration 2), most of the wing is ahead of the nacelle, leading to increased pressures and, accordingly, decreased lift. Any pressure increase forward and aft of quarter-chord led to a pitching moment increase and decrease, respectively. In Configuration 1, this led to decreased pitching moments, while in Configuration 2 the pitching moment was increased. In the numerical simulations, these effects were also observed, but less pronounced, due to the absence of the support sting. Furthermore, the numerical simulation overestimates all isolated wing aerodynamic coefficients, since it omits of the decambering effect of the boundary layer.

5.2. Propeller effects on the wing

In this section, the propeller effects on the wing, in cruise conditions, are demonstrated. The effects of the propeller on the wing pressure distribution, and subsequently on wing boundary layer transition are first presented. Afterwards, the effect of the propeller on the wing performance coefficients, i.e. lift, pressure drag and pitching moment, are shown.

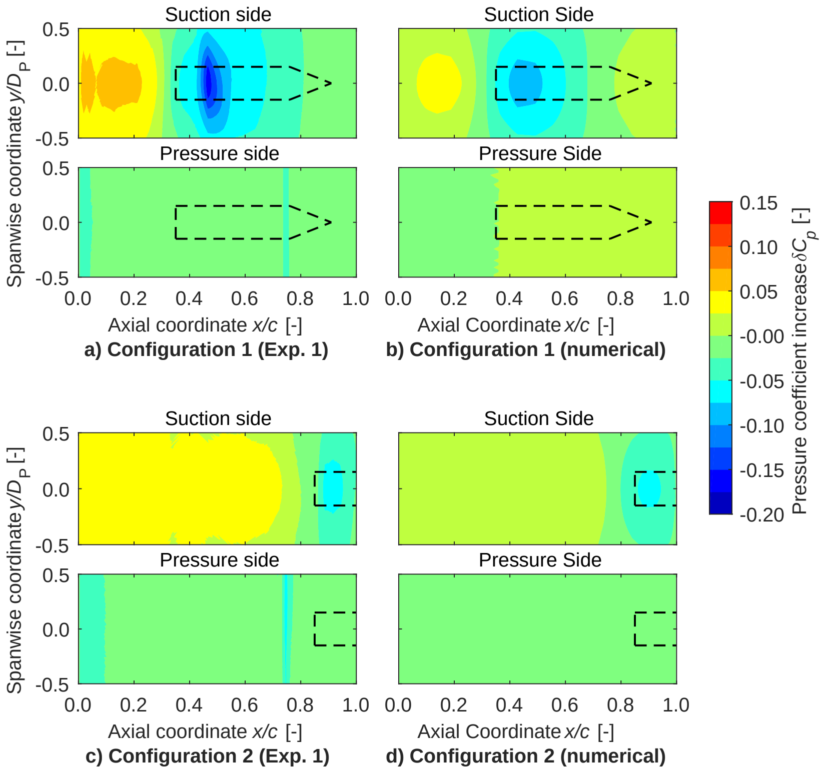

Figure 5.1: Wing pressure coefficient increase due to the presence of the nacelle, in the cruise configurations of Experiment 1. Dashed lines indicate the projection of the nacelle onto the wing surface.

Table 5.1: Propeller-off and isolated wing performance coefficients, in the cruise configurations of Experiment 1.

Configuration	**Experimental**			**Numerical**		
(propeller off)	C_L	C_{D_p}	$C_{m_{c/4}}$	C_L	C_{D_p}	$C_{m_{c/4}}$
Iso. wing	0.47	0.006	-0.061	0.50	0.007	-0.064
1	0.47	0.013	-0.069	0.51	0.011	-0.069
2	0.44	0.008	-0.058	0.50	0.008	-0.067

5.2.1. PROPELLER EFFECTS ON THE WING PRESSURE DISTRIBUTION

The pressure coefficient difference between the propeller-on and propeller-off measurements, i.e. $\Delta C_p = C_{p,\text{prop. on}} - C_{p,\text{prop. off}}$ will be used to demonstrate the effect of the propeller on the pressure distribution over the wing surface. Figure 2.3a presents a generic side-view of the wing and the slipstream surface, used for explanations. Figure 5.2 presents this for Configurations 1 and 2 (flap nested) at advance ratio $J = 0.7$. In Figure 5.2 the flow goes from left to right, and the spanwise coordinate $y/D_\text{P} = 0$ corresponds to the location of the propeller axis.

Figure 5.2 shows that, on the suction side, pressure was reduced in front of the propeller and increased behind it for both configurations, which agrees with earlier research [11, 18, 28]. This is a result of the propeller-induced velocity component at the wing surface shown in Figure 5.3. Ahead of the propeller, the flow is accelerated, since there the wing surface (region I in Figure 2.3a) is washed by the slipstream. Behind the propeller disk (region II in Figure 2.3a), flow is decelerated, since the contracting slipstream surface diverges from the wing surface. Note that that the pressure decrease in front of the propeller disk is symmetric with respect to $y/D_\text{P} = 0$, whereas the pressure increase behind the disk shows some asymmetry in both configurations. The pressure increase is slightly stronger at the down-going blade side. This may be a result of the swirl velocities, which have a downward component at the down-going blade side, increasing the pressure on the wing surface.

In the experimental results of Configuration 1 (Figures 5.2a), a secondary pressure increase can be seen on the suction side at $x_p/c = 0.9$. This effect was also present in the numerical simulations, though less pronounced, and can be attributed to a variation in slipstream-vortex strength near the wing due to the non-

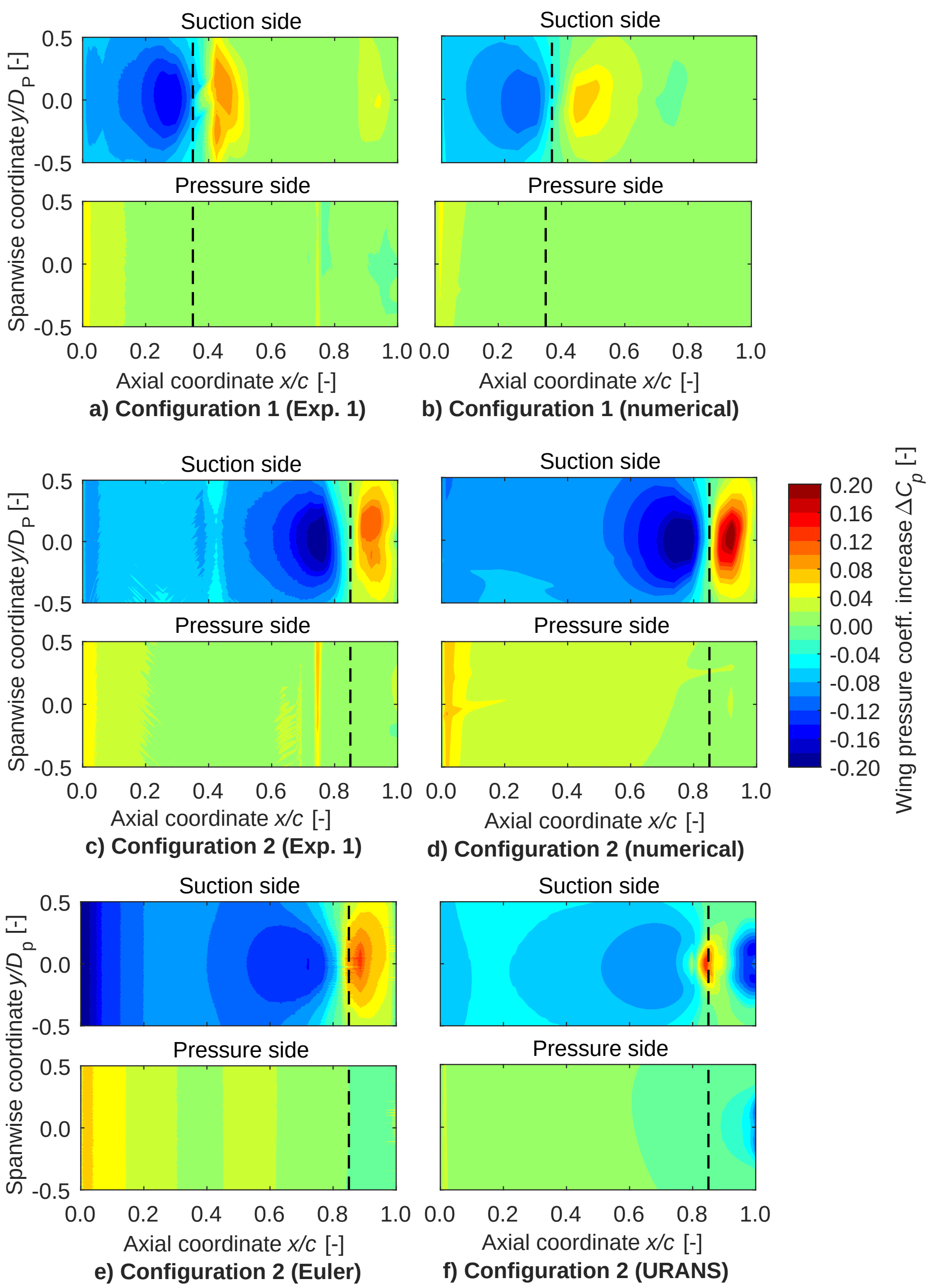

Figure 5.2: Wing pressure distributions, in the cruise configurations of Experiment 1 at advance ratio $J = 0.7$. Dashed lines indicate the projection of the propeller disk onto the wing surface.

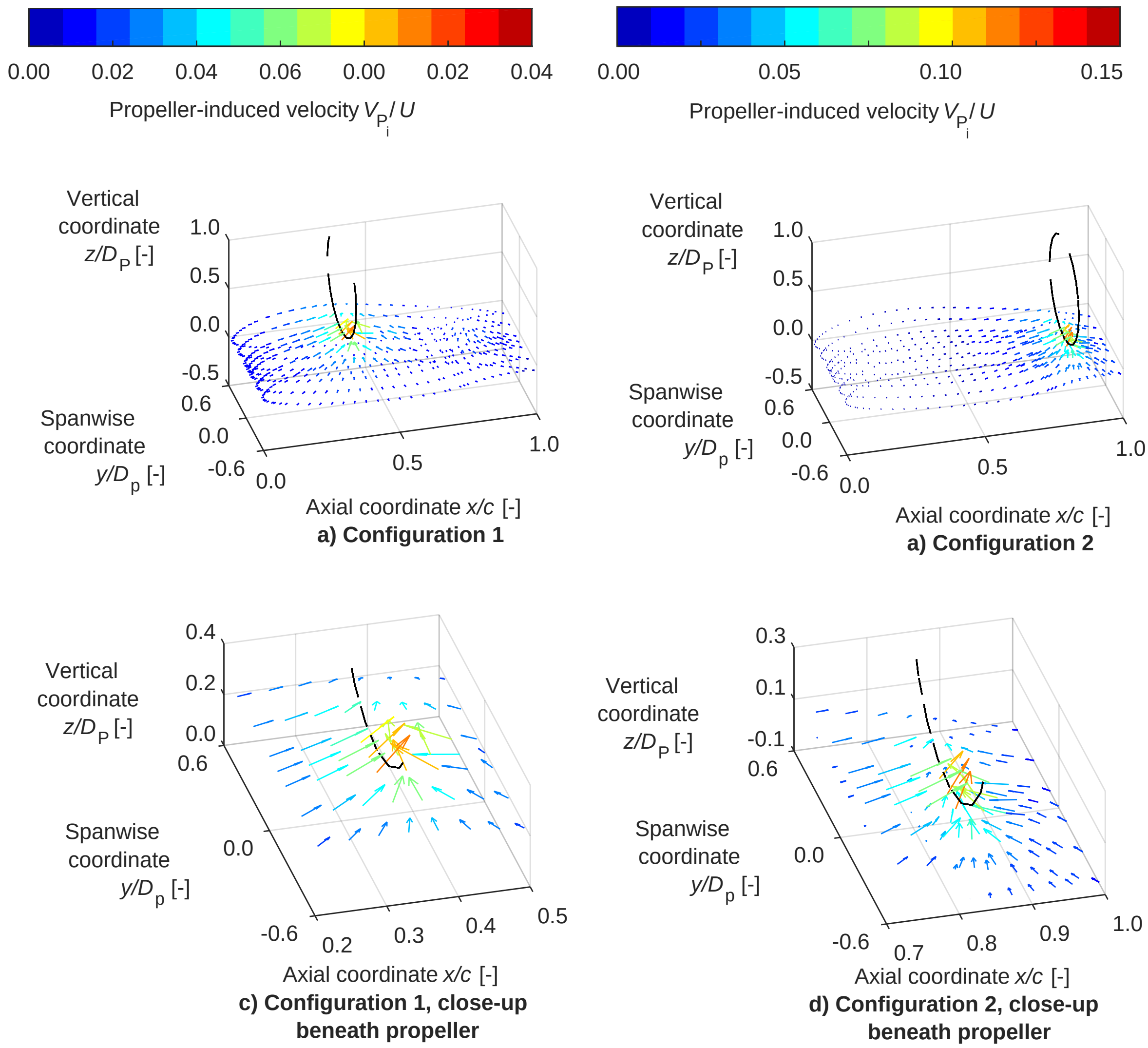

Figure 5.3: Numerically found vector plots of the propeller-induced velocities at the wing surface in Experiment 1, at advance ratio $J = 0.7$. Colours indicate the velocity magnitude, the propeller disk is shown in black. Note that each configuration has its own colour scale.

uniform propeller loading. On the pressure side, meanwhile, the first noticeable pressure change is a minor increase in pressure coefficient near the flap slot, due to the increased pressure behind the propeller disk which is propagated through the slot. This effect is absent in the numerical model, which did not include the slot. The second pressure change that can be seen on the pressure side is a minor increase of pressure at the wing's leading edge. Figure 5.3 shows that this is caused by the propeller inducing velocities which have a direction upward vertically and downstream axially at this location.

Suction side results at advance ratios $J = 0.8$ and $J = 0.9$ are shown in Figure 5.4[1]. They confirmed that the effects were similar, but that the magnitude of the pressure differences diminished with increasing advance ratio, and that the pressure increase at the lower surface leading edge was not present at higher advance ratio. More pronounced pressure effects of the propeller on the wing are observed for Configuration 2 than for Configuration 1. This is a consequence of the higher effective advance ratio in Configuration 1, since the wing-induced velocities were higher at 35% chord than at the main element's trailing edge (see Figure 4.5). In Configuration 1, at $J = 0.9$ pressures were increased ahead of the propeller disk, contrary to Figure 5.2. This is a result of local windmilling of the propeller close to the wing surface due to strong wing-induced inflow velocities.

[1]The changes in pressure coefficient on the pressure side of the wing surface are negligible and these results are thus omitted.

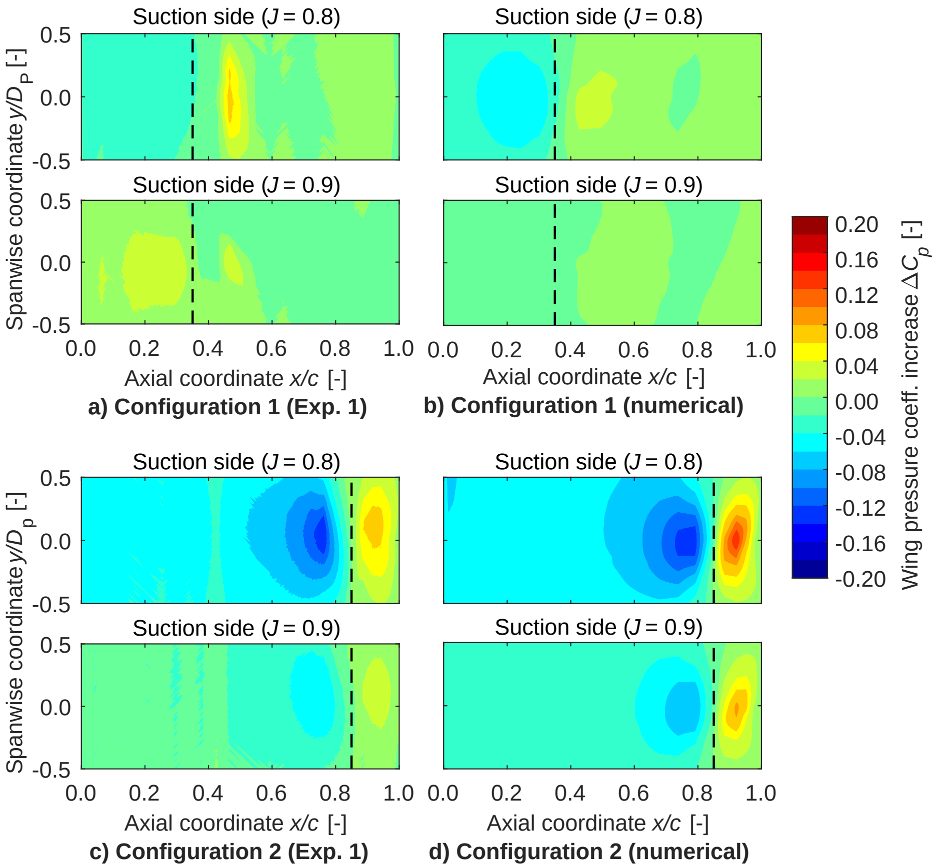

Figure 5.4: Wing suction side pressure distributions, in the cruise configurations of Experiment 1 at $J = 0.8$ and 0.9. Dashed lines indicate the projection of the propeller disk onto the wing surface. Note that as opposed to Figure 5.2, only suction side results are shown.

The trends observed in the experimental results are captured with sufficient confidence by the numerical model. The location of the pressure decrease in front of the propeller disk is captured well by by the numerical model. The location of the pressure increase behind the propeller disk is correctly modelled in Configuration 2, but in Configuration 1, its location is slightly too far aft at $J = 0.7$. At $J = 0.8$, it has a smaller span than in the experimental results, and at $J = 0.9$ it is barely discernable. The magnitudes of the pressure changes are slightly underestimated and in Configuration 1 at $J = 0.7$ and overestimated in Configuration 2 at all advance ratios. At $J = 0.8$ in Configuration 1, the numerical model incorrectly shows a pressure decrease in front of the propeller disk, whereas the experimental results show little effect in this location. At $J = 0.9$ in Configuration 1, the slight pressure increase in front of the propeller disk that is found experimentally, is not found by the numerical simulation. The pressure increase at the lower surface leading edge at $J = 0.7$ is predicted correctly in Configuration 1, but overestimated in strength in Configuration 2. At $J = 0.8$ and 0.9, it is absent, as in the experimental results. The modelling errors in the numerical simulation are a result of the simplification of steady non-uniform loading and the omission of interaction effects between the nacelle and the slipstream. Furthermore the overestimation of propeller loading at high advance ratio by the BEM (see Figure 4.8) is causing the propeller effects to be overestimated in Configuration 1 at $J = 0.8$ and 0.9.

To benchmark the accuracy of the numerical solver, it was compared to two higher-fidelity methods. Firstly, Figure 5.2e presents a CFD Euler simulation by Khajehzadeh [71]. Since the Euler equations are adiabatic, viscous effects were neglected, but the solution did account for compressible and rotational flow. The propeller was modelled as an actuator disk. Secondly, Figure 5.2f shows the results of an Unsteady Reynolds-Averaged Navier-stokes (URANS) solution by Fischer [21]. The propeller blades were modelled as lifting lines, which were added as source terms to the RANS equations. The simulation was then advanced in time, leading to a new propeller position, for which the flow field is subsequently solved. This process is repeated until the propeller has performed a full rotation.

Overall, the numerical model in this thesis performs remarkably well, compared to the Euler and URANS simulations. It captures the suction in front of the propeller disk best. Furthermore, on a personal laptop, typically it finishes in 10 minutes, whereas the Euler simulation takes 6 hours and the URANS is run on a computing cluster. On the other hand, the pressure increase behind the propeller disk is quantitatively better modelled by the Euler simulations, and the URANS simulation has the benefit of providing viscous drag results and is applicable to high-lift configurations.

5.2.2. PROPELLER EFFECTS ON WING BOUNDARY LAYER TRANSITION

The pressure distributions were nearly symmetric with respect to $y/D_P = 0$, coinciding with the observations of Müller et al.[20], who conclude that the effect of the propeller on the wing is dominantly potential and not significantly affected by the swirl in the propeller slipstream. This claim was further assessed by analysing the infrared images. These showed that, for the aft-mounted position (Configuration 2), the boundary-layer transition location was not noticably affected by the propeller.

For Configuration 1, on the other hand, local changes in transition location were observed. These observations are shown in Figure 5.5. In the propeller-off case of Configuration 1 (Figure 5.5a), the transition location moved aft due to the favourable pressure gradient change generated by the nacelle. However, with the propeller operating ahead of the transition line (Figure 5.5), the transition location moved forward, similarly to a tractor propeller [40]. There are two reasons for this. Firstly, an adverse pressure gradient is generated in the vicinity of the propeller disk, as visible in Figure 5.2. Secondly, the interaction between the tip vortices and the boundary layer introduces instabilities in the flow [19, 40]. Additional studies are required to quantify the relative impact of these effects, but the infrared images show that the propeller only has an impact on boundary layer transition if it is installed close to or ahead of the transition location. The choice of an inviscid method to numerically model the wing is thus reasonable.

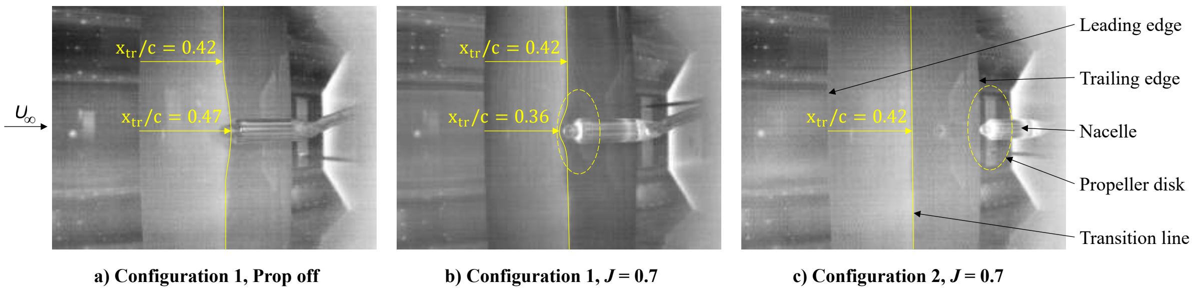

Figure 5.5: Infrared images showing the effect of the propeller on boundary layer transition in Experiment 1 (in cruise conditions).

5.2.3. PROPELLER EFFECTS ON WING PERFORMANCE

To separate the effect of the propeller on the wing, Figure 5.6 shows the lift, drag and pitching moment coefficients as a difference between propeller-off and propeller-on conditions. Evidently, wing lift increased with decreasing advance ratio (increased thrust). This can be attributed to the region of low pressure generated in front of the propeller, which became stronger with increasing propeller thrust. In Configuration 1, the measurements of Experiment 1 at $J = 0.9$ present a lower lift coefficient than with the propeller off. This can be attributed to local windmilling of the propeller close to the wing surface as discussed in the previous section.

Regarding the pressure drag of the wing, it can be seen that for Configuration 1 pressure drag decreases with decreasing advance ratio. This is due to increased suction ahead of the propeller, which leads to a lift increase forward of the thickest point of the wing. In Configuration 2, it appears the overall pressure variations upstream and downstream of the thickest point follow similar trends, leading to an approximately constant pressure drag. The effect of the propeller on the wing's pitching moment increased with decreasing advance ratio. In Configuration 1, the increased suction forward of quarter-chord and the increased pressure aft of $0.35{\cdot}c$ increased the pitching moment. In Configuration 2, the change in pitching moment was dominated by the increased suction between quarter-chord and $0.85{\cdot}c$, which decreased the pitching moment. The found trends agree with earlier studies [11, 17, 18]. Furthermore, similarly to Cooper et al. [17] and Veldhuis [18], but unlike Johnson and White [11], a pressure drag increase is found for an axial propeller position near the wing trailing edge.

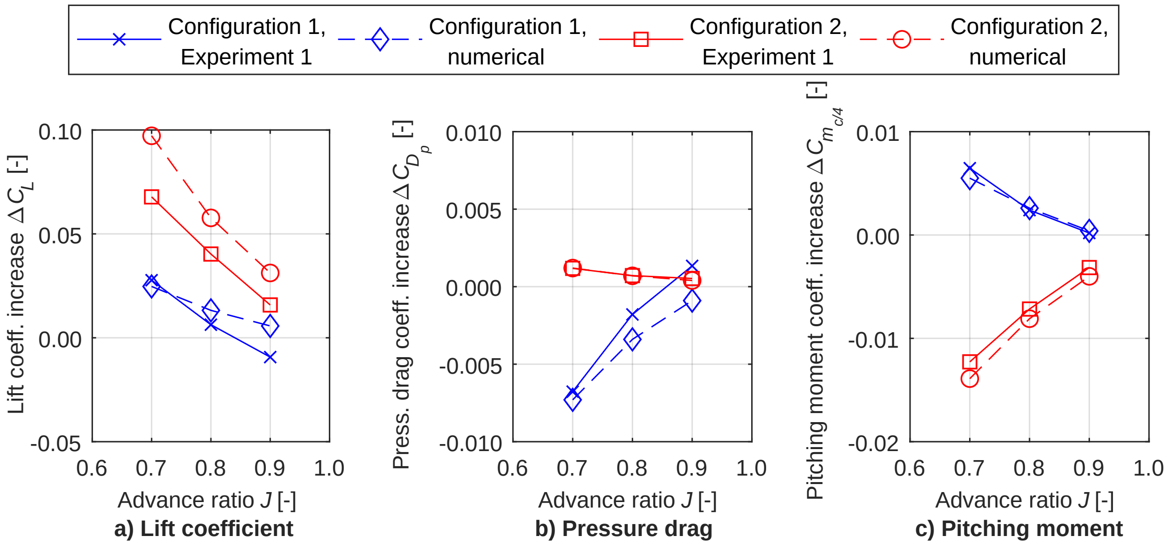

Figure 5.6: Wing lift, pressure drag and pitching moment increase with respect to propeller-off conditions, in Experiment 1 (in cruise conditions), as a function of advance ratio.

The numerical tool is in qualitative agreement in both Configurations, for all three wing performance coefficients. Furthermore, its results are numerically accurate in Configuration 1 at low advance ratio. The pitching moment coefficient change is predicted numerically accurate in both configurations at all advance ratios. However, the numerical tool overestimates the lift in Configuration 2, at all advance ratios. This can be attributed to the overestimation of change in pressure distribution shown in Figure 5.2, caused by the simplification of steady non-uniform loading and omission of nacelle-slipstream interaction effects. Additionally, in Configuration 1 accuracies in lift and pressure drag decrease with increasing advance ratio. This is caused by the overestimation of blade loading by the BEM at high advance ratios (see Figure 4.8). Overall, the numerical tool's accuracy regarding the effect of the propeller on wing performance is certainly adequate for the aircraft conceptual design phase.

5.3. WING EFFECTS ON THE PROPELLER

In this section, the wing effects on the propeller, in cruise conditions, are demonstrated. First, the slipstream geometry in the numerical method is analyzed to determine the effects of the wing in terms of slipstream deformation. Subsequently, the effect of the wing on propeller loading is discussed. Thirdly, the propeller performance parameters, i.e. thrust, torque and efficiency, in an over-the-wing configuration are presented and finally the in-plane forces on the propeller are shown.

5.3.1. WING EFFECTS ON THE PROPELLER SLIPSTREAM

To better understand the aerodynamic interaction effects involving the slipstream deformation, Figure 5.7 presents the vortex lattice geometry for Configuration 1. The vortex lattice surface starts as an idealized helicoidal surface, like the model illustrated in Figure 4.11. However, closely behind the propeller disk, the propeller radial loading variation starts to deform the surface. At the hub and tip, propeller-induced velocities are very low, and the slipstream surface travels at approximately freestream velocity. Due to the stronger propeller-induced velocities at mid-blade sections, the slipstream travels faster towards the middle of its radius, leading to a radial deformation.

Additionally, the wing-induced velocities lead to three discernible deformations of the slipstream. Firstly, the wing accelerates the flow axially, and correspondingly the slipstream. Secondly, this axial acceleration is stronger near the wing surface, leading to shearing of the slipstream, i.e. the bottom of the slipstream moves downstream faster than its top. Thirdly, wing-induced velocities are generally aligned with the wing surface, leading to downward movement of the slipstream. This effect is also stronger closer to the wing, leading to stretching of the slipstream in vertical direction.

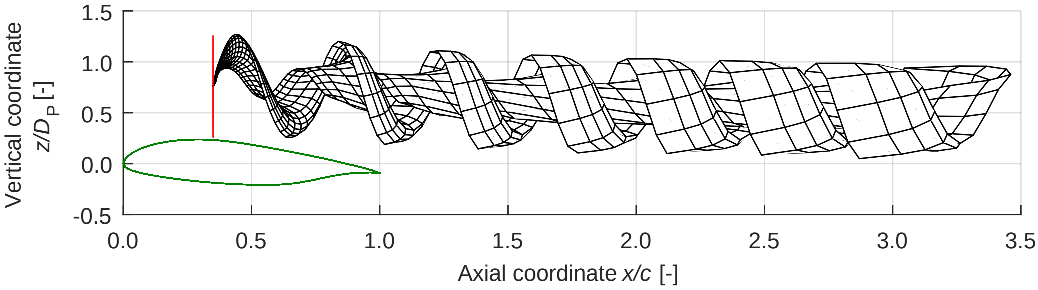

Figure 5.7: Side view of the slipstream vortex lattice for one blade position in Configuration 1 at $J = 0.7$, as found by numerical simulation. Propeller disk and wing, respectively red and green, are shown for reference.

5.3.2. WING EFFECTS ON PROPELLER LOADING

Experiment 1 wake-plane and numerical disk-plane total pressure distributions and numerical circulation distributions, in the cruise configurations, are shown in Figure 5.8. Results at advance ratios 0.8 and 0.9 can be found in Figure 5.9. By comparing Figures 5.8a and 5.8d to 5.8b and 5.8e respectively, it can be seen how the highly-loaded region in the wake plane has turned clockwise due to the propeller-induced swirl, and has increased in magnitude and concentrated over a smaller region due to contraction. In the wake plane (Figures 5.8b and 5.8e), the increased total pressure in the propeller slipstream and decreased total pressure in the wake of the support sting, nacelle and wing can be clearly distinguished. At higher advance ratio, the effects are similar, but the pressure in the slipstream is lower, while the wakes are larger.

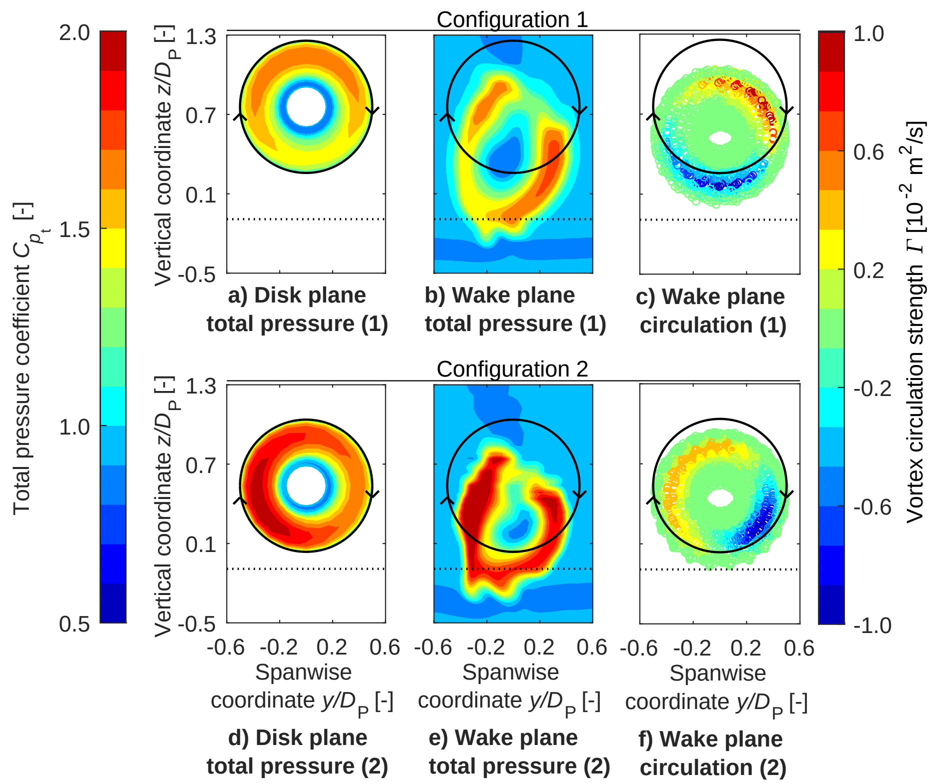

Figure 5.8: Disk (numerical) and wake plane (experimental) total pressure and wake plane circulation (numerical) distributions in the cruise configurations of Experiment 1, at advance ratio $J = 0.7$. Continuous and dotted lines indicate projections of propeller disk and wing trailing edge, respectively.

Due to the downwash of the wing, the propeller slipstream is deformed and displaced in vertical direction. To assess whether the numerical model captures these effects correctly, Figures 5.8c and 5.8f contain the wake

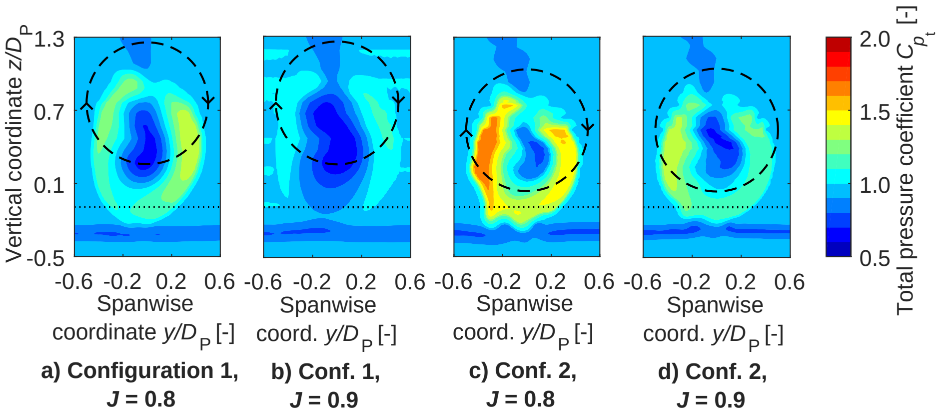

Figure 5.9: Wake plane total pressure distributions as measured in the cruise configurations of Experiment 1 at $J = 0.8$ and 0.9. Dashed and dotted lines in the wake plane indicate projections of propeller disk and wing trailing edge, respectively.

plane circulation distributions[2]. It can be seen that in both cruise configurations, the downward movement and vertical stretching of the slipstream is underestimated. This can be partly explained by the absence of the nacelle and sting wakes in the numerical model. In the experiment, the nacelle and sting wakes lead to an axial velocity deficit inside the slipstream, which is not present in the numerical model. As a result, the slipstream is travelling downstream faster in the simulation than in the experiment. The wing-induced velocities are thus relatively lower, leading to less downward movement of the slipstream. Furthermore, it can be seen that the swirl is computed appropriately, since the experimental light and heavy loading regions are in the same location as the positive and negative circulation regions, respectively.

To explain the propeller loading distributions, Figure 5.10 depicts the wing-and-nacelle-induced velocity component in the Experiment 1 configurations. Three important effects can be seen. Firstly, the wing-induced velocity component has a significant axial component. As a result, less thrust is generated for a given advance ratio than in the isolated propeller case in both cruise configurations. This is confirmed by comparing the total pressure distributions in Figures 5.8a and c to the isolated propeller values in Figure 4.8. The thrust reduction is more pronounced in Configuration 1, since on the forward part of the airfoil the velocity increase generated by the wing is higher, and thus the effective advance ratio of the propeller is increased more than in Configuration 2. Figure 5.9b indicates that at high advance ratio in Configuration 2, the propeller is partially windmilling.

Secondly, the non-uniform inflow conditions lead to azimuthal loading variations in both configurations. In Configuration 1, the strong vertical velocity gradient above the wing is the main source of non-uniform disk loading. This leads to a low disk loading near the wing, where inflow velocities are highest. In Configuration 2, however, the wing-and-nacelle-induced velocities have a negative z-component, generating the highest loads on the upward-going blade, which experiences a higher angle of attack. From this it can be concluded that, while the effect of the propeller on the wing pressure distribution is symmetric with respect to $y/D_P = 0$, the effect of the wing on propeller loading is asymmetric in Configuration 2, but symmetric in Configuration 1.

Lastly, at the inner blade sections, a significant flow component directed radially outward can be distinguished. This is caused by the propeller hub, around which the flow expands. Since the flow is in radial direction, it does not directly change the propeller loading. However, it may result in a radially outward movement of the boundary layer, resulting in mid-blade sections being more prone to stall [72]. This is not modelled, which may be an explanation of the numerically overestimated mid-blade loading in Figure 4.8 at high advance ratio.

5.3.3. WING EFFECTS ON PROPELLER PERFORMANCE

To determine the effects of the wing on propeller performance, its thrust and torque coefficients and efficiency in Experiment 2 and its simulation will be discussed. Isolated propeller results were already discussed in Section 4.2.1, whereas in this section the primary concern is the effect of the wing on the propeller. Accordingly, Figure 5.11 presents these coefficients versus advance ratio as a difference between the isolated

[2]It is not possible to obtain the wake plane total pressure distribution in the numerical simulation, since inside the slipstream, propeller-induced velocities cannot be meaningfully computed.

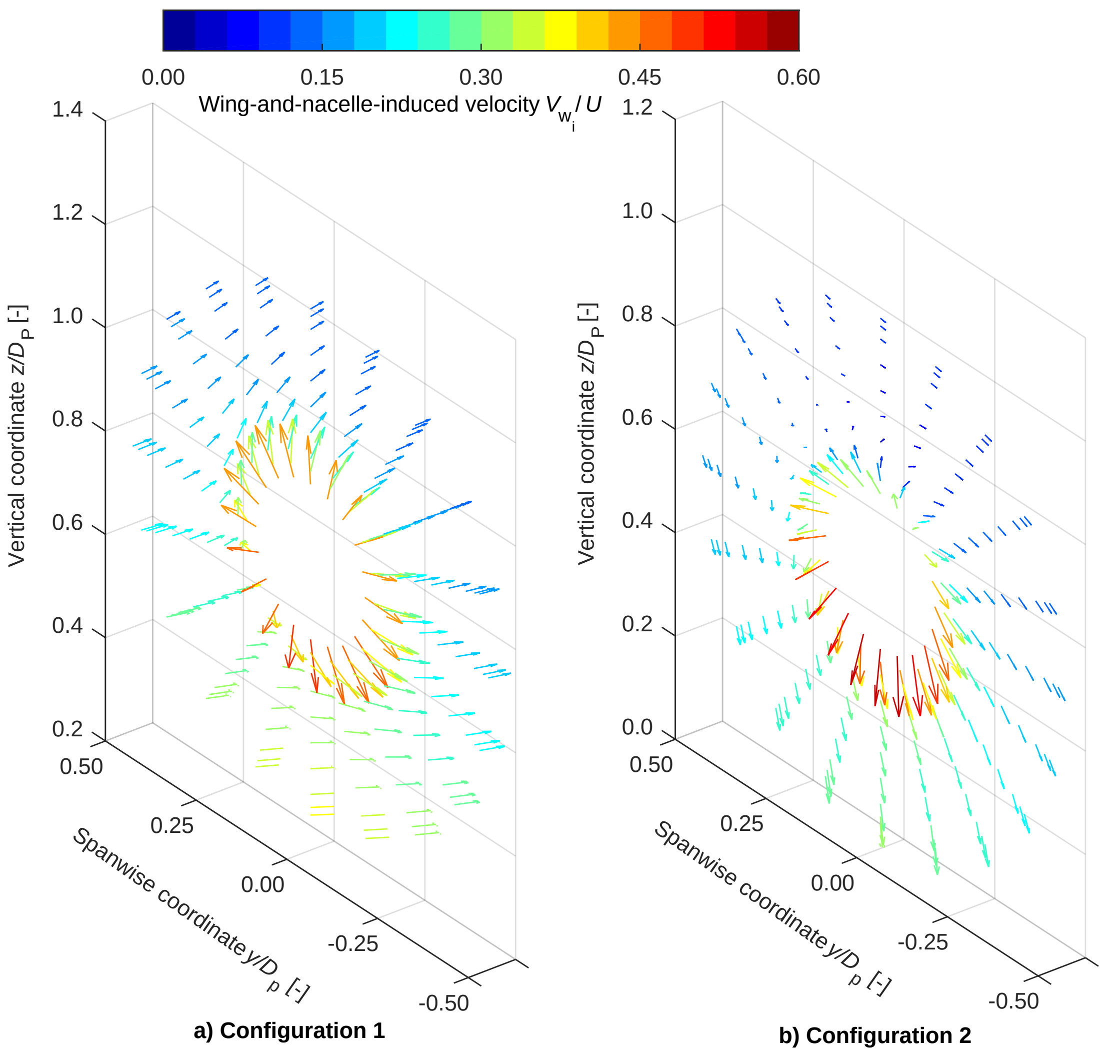

Figure 5.10: Numerically found vector plots of the wing-and-nacelle-induced velocity component at the propeller disk in Experiment 1, at $J = 0.7$.

and installed propeller, i.e. $\Delta C = C_{\text{installed}} - C_{\text{isolated}}$ for $C = C_T, C_Q, \eta$. Isolated propeller values can be found in Figure 4.9. Since the primary interest is in system performance, the advance ratio is based on freestream velocity, and not local inflow conditions.

Figures 5.11a, 5.11b and 5.11c present the propeller thrust coefficient increase in Experiment 2. Firstly, it can be seen how in all configurations, thrust is reduced compared to the isolated propeller. This is due to the axial velocity increase at the propeller disk caused by the wing. The thrust reduction becomes stronger as the propeller moves forward on the wing, since the wing inflow velocities are higher for the forward position, as discussed earlier. For increasing clearance, the thrust reduction decreases, since wing-induced velocities are lower further away from the wing. The effect of clearance is strongest for the forward positions, since these feature a stronger vertical velocity gradient. Secondly, the thrust reduction increases with increasing advance ratio. This is a result of the wing-induced velocities becoming more dominant as the propeller rotational velocity decreases.

The numerical model captures these effects qualitatively, but overestimates the thrust reduction at low advance ratio. This is a combination of two modelling errors. Firstly, the panel method overestimates the inflow velocities at the propeller disk, as was shown in Figure 4.6. This leads to an overestimation of the thrust reduction at all advance ratios. Furthermore, Figure 4.9 has shown that the BEM underestimates thrust at high advance ratio. This effect increases with increasing advance ratio. Since the effective advance ratio is higher when the propeller is installed, this leads to a significant underestimation of the installed propeller

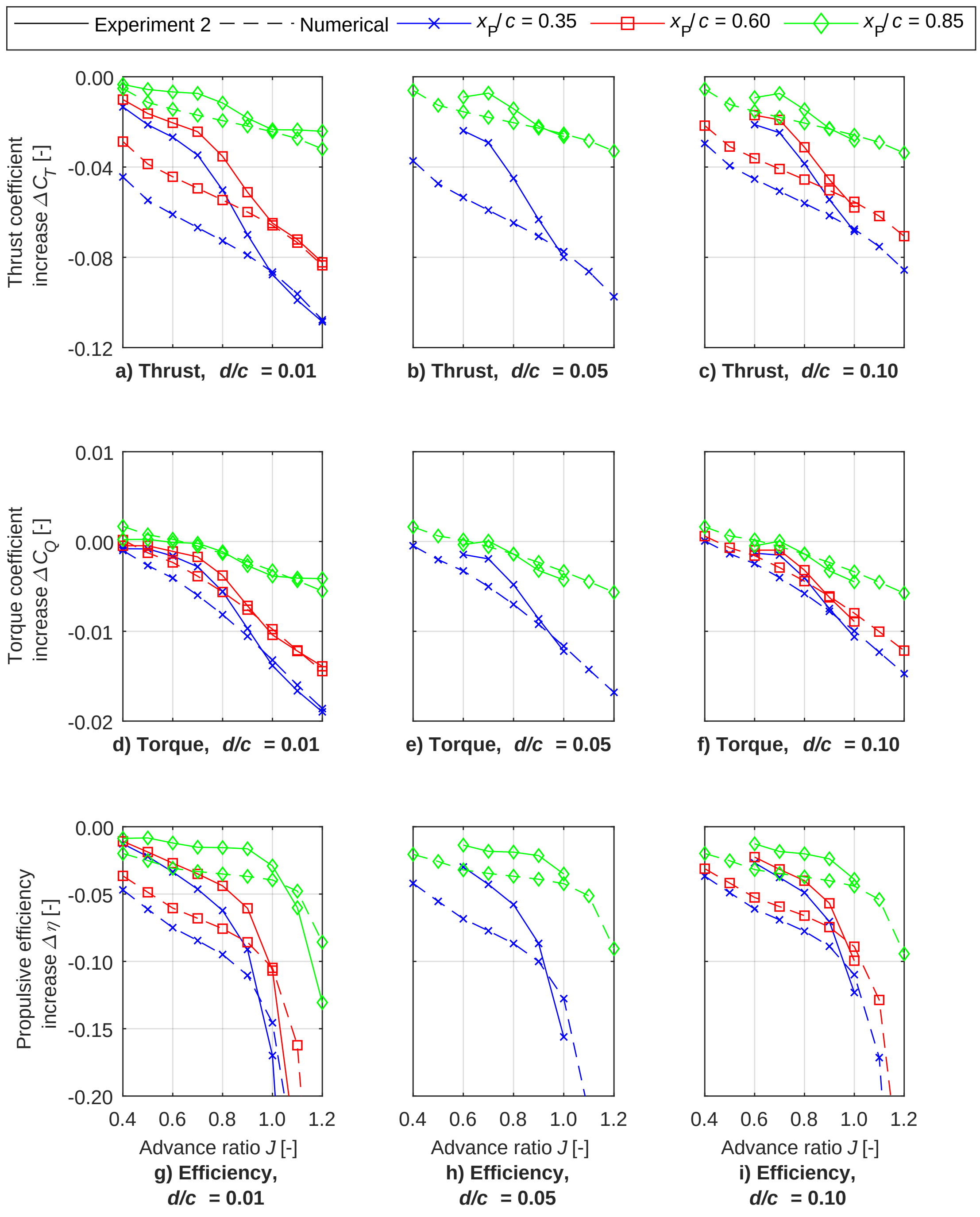

Figure 5.11: Propeller thrust and torque coefficients and efficiency versus advance ratio in Experiment 2, as found experimentally and by numerical simulation, at three clearances.

thrust at high advance ratio. At high advance ratio, both of these errors compensate each other, leading to a correct estimation of the thrust decrease.

The propeller torque coefficient in Experiment 2 can be found in Figures 5.11d, 5.11e and 5.11f. Similarly to the thrust, in most configurations, the torque is reduced compared to the isolated propeller, due to the wing-induced velocities, which increase the effective advance ratio. However, for $x_P/c = 0.85$, at low advance ratio, the torque is practically unchanged. This can be attributed to the wing-induced velocities having a negative z-component, which increases the propeller blade angle of attack at the up-going blade, while reducing it at the down-going blade. Similarly to the thrust, the torque reduction increases with increasing advance ratios, and decreases with increasing clearance.

Again, the numerical model captures these changes qualitatively, but overestimates the torque reduction at high advance ratio. This can also be explained by the overestimation of wing-induced velocities by the panel method, as well as the error in the modelling of the isolated propeller. Figure 4.9 depicts how the BEM over- and underestimates torque at high and low advance ratios, respectively. On the other hand, the overestimation of wing-induced velocities at the propeller disk results in an overestimation of the torque.

Finally, Figures 5.11g, 5.11h and 5.11i present the propeller efficiency in Experiment 2. Generally, the propeller efficiency is decreased compared to the isolated propeller, due to the increase in effective advance ratio. Once more, the numerical model captures the trends observed in the experiment. However, quantitatively, the errors in thrust and torque estimation lead to significant discrepancies with the experiment, especially at low advance ratio. Overall, the accuracy of the numerical tool concerning the effect of the wing on propeller performance is adequate for the aircraft conceptual design phase.

Figure 5.12 shows the effect of axial propeller position and clearance on the propeller efficiency at the advance ratio for optimal efficiency, $J = 1.0$. Similarly to the thrust and torque, the propeller efficiency decreases more as the propeller moves forward on the wing, due to the increase in inflow velocities. This effect becomes stronger at lower clearance, since inflow velocities are higher closer to the wing. This also leads to the propeller efficiency decreasing less with increasing clearance for $x_P = 0.35$, similarly to findings by Müller et al. [20]. On the contrary, for $x_P = 0.85$, the propeller efficiency decreases slightly more with increasing clearance, since the propeller disk inflow has an angle of attack, which is beneficial to propeller efficiency [41].

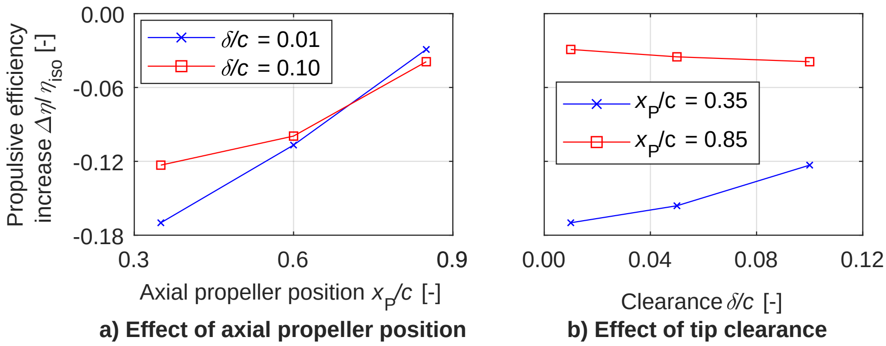

Figure 5.12: Propeller efficiency versus (a) axial propeller position at two clearances and (b) versus clearance at two axial propeller positions, as experimentally found in Experiment 2 at $J = 1.0$.

5.3.4. OVER-THE-WING PROPELLER IN-PLANE FORCES

The non-uniform inflow to the propeller disk causes forces inside the propeller disk plane, which are discussed in this section. As explained in Section 3.2.1, these results are limited to the numerical simulations. It is thus only possible to compare them to the behaviour as expected from the explanation in Section 2.4. A validation with experimental or higher-fidelity numerical (e.g. CFD) results is thus recommended.

Figure 5.13 presents normal and side force coefficients for over-the-wing configurations. Since the in-plane forces on the isolated propeller are naught, force coefficients are not presented as a difference between the installed and isolated propeller as in the previous section, but absolutely. Note that the forces are defined in the over-the-wing reference system, i.e. the normal force is parallel to the wing lift force, along the z-axis, and the side force acts parallel to the wing span, along the y-axis.

The propeller normal force can be seen in Figures 5.13a to c. Installing the propeller over-the-wing leads to a normal force counteracting the wing lift force. This is a result of the negative angle of attack of the flow, which follows the wing contour, as explained in Section 2.4. The normal force becomes larger as the propeller moves aft axially, due to the angle of attack becoming more negative. It also slightly strengthens for lower clearances, due to the stronger inflow effects as the wing is approached. Lastly, it increases in magnitude with increasing advance ratio, since the angle of attack leads to a higher blade section angle of attack change if the propeller rotational velocity is lower.

The propeller side force can be seen in Figures 5.13d to f. As explained in Section 2.4, the side force for an over-the-wing propeller is caused by the vertical velocity gradient above the wing, and is negative for a right-hand rotating propeller. It has already been shown that the highest gradient of wing-induced velocities can be found above the thickest part of the wing, near $x_P = 0.35$. This is why the side force decreases in magnitude as the propeller moves aft axially. Similarly to the normal force, it strengthens with decreasing clearance and with increasing advance ratio.

Although these results should still be validated by comparison to experimental or higher-fidelity numerical results, the trends match the expected behaviour explained in Section 2.4. The generation of these in-plane forces is undesirable since the negative normal force counteracts lift and the side force must be compensated with rudder deflection, which will both increase the aircraft's drag. For the wing in the experiment at a cruise lift coefficient of 0.5 and at the advance ratio for optimal efficiency ($J \approx 1.0$), the normal force at $x_P = 0.85$ and side force at $x_P = 0.35$ amount to 4.6% and 2.8% of the lift force on a wing area spanning the propeller diameter. Since the side force direction is dependent on the propeller rotational direction, the side force on the whole aircraft can also be neutralized by installing counterrotating propellers.

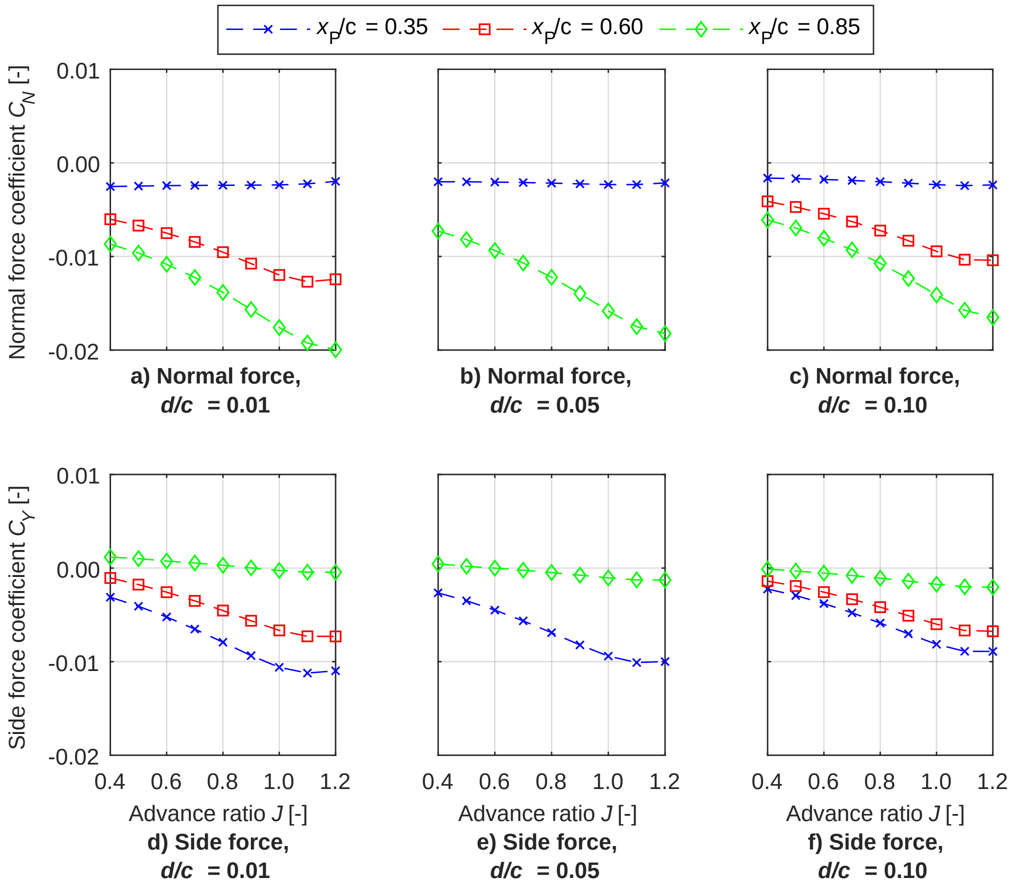

Figure 5.13: Propeller normal and side force coefficients in Experiment 2 versus advance ratio, as found by numerical simulation, at three clearances.

6

PERFORMANCE IN HIGH-LIFT CONFIGURATIONS

In this chapter, the results are presented for high-lift conditions. These conditions are representative of the climb segment, when the flap is deflected ($C_L \approx 1.6$) and wing lift should be maximized. Although the numerical model does not provide accurate results in case of flap deflection (see section 4.1.3), the experimental results are briefly discussed to demonstrate the potential of over-the-wing propellers, and to establish the need for improved methods capable of evaluating over-the-wing systems in high-lift conditions.

6.1. NACELLE EFFECTS ON THE WING

The installation effects in high-lift configurations will first be shown, similarly to Section 5.1. The installation effect on the wing pressure distribution, δC_p, is shown in Figure 6.1. Compared to cruise installation effects, the pressure increase upstream of the nacelle was stronger, and the pressure decrease downstream of the na-

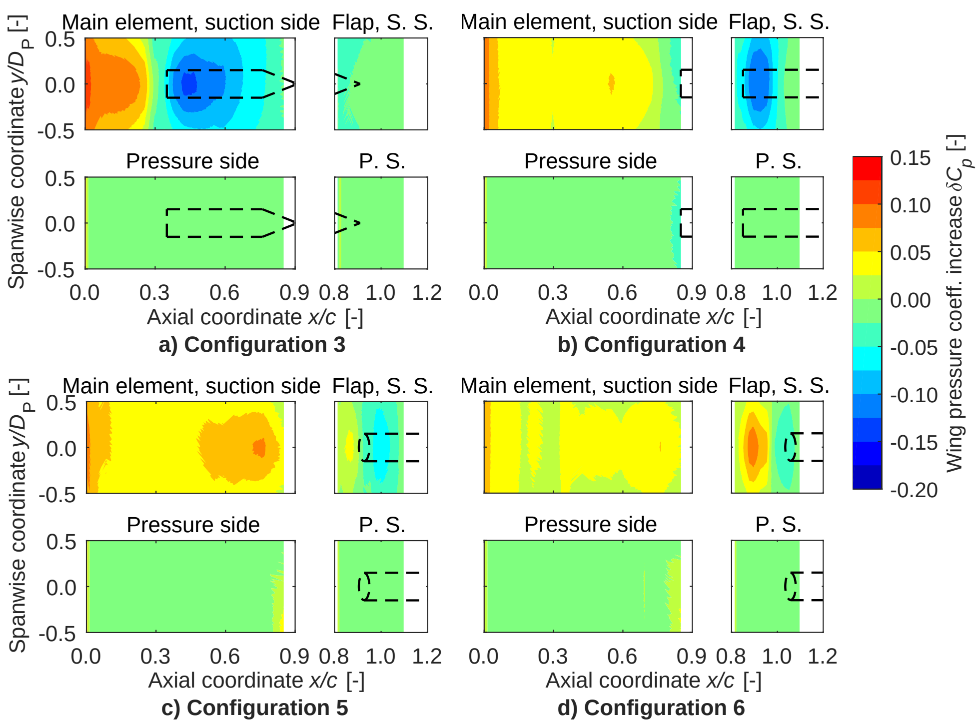

Figure 6.1: Wing pressure coefficient increase due to the presence of the nacelle Experiment 1 (in climb conditions). Dashed lines indicate the projection of the nacelle onto the wing surface.

celle affected a larger region of the wing. This is a result of the flow around the wing being directed downward more when the flap is deflected. The effective frontal area of the nacelle as seen by the flow is thus higher, leading to more blockage and a stronger effect on the wing pressure distribution. It can be seen that as the nacelle moves aft, the pressure increase at the leading edge remained, but diminished in magnitude. Moreover, a larger and smaller region of the wing were affected by the upstream pressure increase and downstream pressure decrease, respectively.

Table 6.1 presents the isolated wing and propeller-off lift, drag and pitching moment coefficients for the high-lift configurations of Experiment 1. The installation effects are similar to the cruise configurations. As a result, pressure drag increases in all configurations and lift decreases for nacelle positions near the trailing edge (Configurations 4 to 6), compared to the isolated wing. Pitching moment decreases in Configuration 3, while in the other configurations the pitching moment increases.

Table 6.1: Propeller-off and isolated wing performance coefficients Experiment 1 (in climb conditions).

Configuration	**Experimental**		
(propeller off)	C_L [-]	C_{D_p} [-]	$C_{m_{c/4}}$ [-]
Isolated wing	1.63	0.020	-0.35
3	1.64	0.032	-0.36
4	1.61	0.026	-0.35
5	1.60	0.025	-0.34
6	1.60	0.023	-0.34

6.2. PROPELLER EFFECTS ON THE WING

The propeller effects on the wing, in climb conditions, are demonstrated in this section. Results include the effects of the propeller on the wing pressure distribution, on wing boundary layer transition, and afterwards, the effect of the propeller on the wing performance coefficients, i.e. lift, pressure drag and pitching moment.

6.2.1. PROPELLER EFFECTS ON THE WING PRESSURE DISTRIBUTION

The wing pressure coefficient distributions, ΔC_p, are presented in Figure 6.2 for high-lift Configurations 3 to 6 (flap deflected) at advance ratio $J = 0.7$. Again, wing pressures were decreased and increased in front of and behind the propeller respectively, except in Configuration 3. In this configuration, the effective advance ratio was exceptionally high and, accordingly, propeller effects on the wing were weak. When the propeller was inclined at 23° (Configuration 5), the suction on the main element was decreased while the pressure on the flap was increased. The pressure variations became even more prominent in Configuration 6 due to an improved alignment between the propeller axis and the local flow direction, and reduced distance between the flap surface and the propeller. The found trends are similar to earlier results for an over-the-wing propeller configuration in which the wing has a plain flap [20].

Suction side results at advance ratios $J = 0.8$ and 0.9 can be found in Figure 6.3[1]. In Configuration 3, the pressure changes become stronger with increasing advance ratio. This is a result of the partial windmilling of the propeller increasing in strength and affecting a larger portion of the propeller disk. In Configurations 4 to 6, the pressure changes on the wing at $J = 0.8$ and 0.9 are very small. This can be attributed to the propeller barely producing thrust or windmilling near the wing surface.

6.2.2. PROPELLER EFFECTS ON WING BOUNDARY LAYER TRANSITION

The effect of the propeller on boundary layer transition in high-lift configurations is shown in Figure 6.4. Figure 6.4a shows the transition location of the isolated wing and noticably, that on part of the main element, transition occured earlier. This is presumably caused by a surface contamination that was present after positioning the wing in the high-lift configuration. In Configuration 3, no transition location movement is observed during propeller-off measurements. However, with the propeller on, Figure 6.4b shows that transition is delayed. As opposed to cruise Configuration 1, in this case the propeller is slightly behind the isolated-wing transition location, leading to a favourable pressure decrease. This effect was expected from earlier research on the effect of a pusher propeller [40] or over-wing nacelle [38] on the wing boundary layer. Contrary to a study by Müller et al. [19], no flow separation was observed. This can most likely be attributed to the higher

[1] The changes in pressure coefficient on the pressure side of the wing surface are negligible and these results are thus omitted.

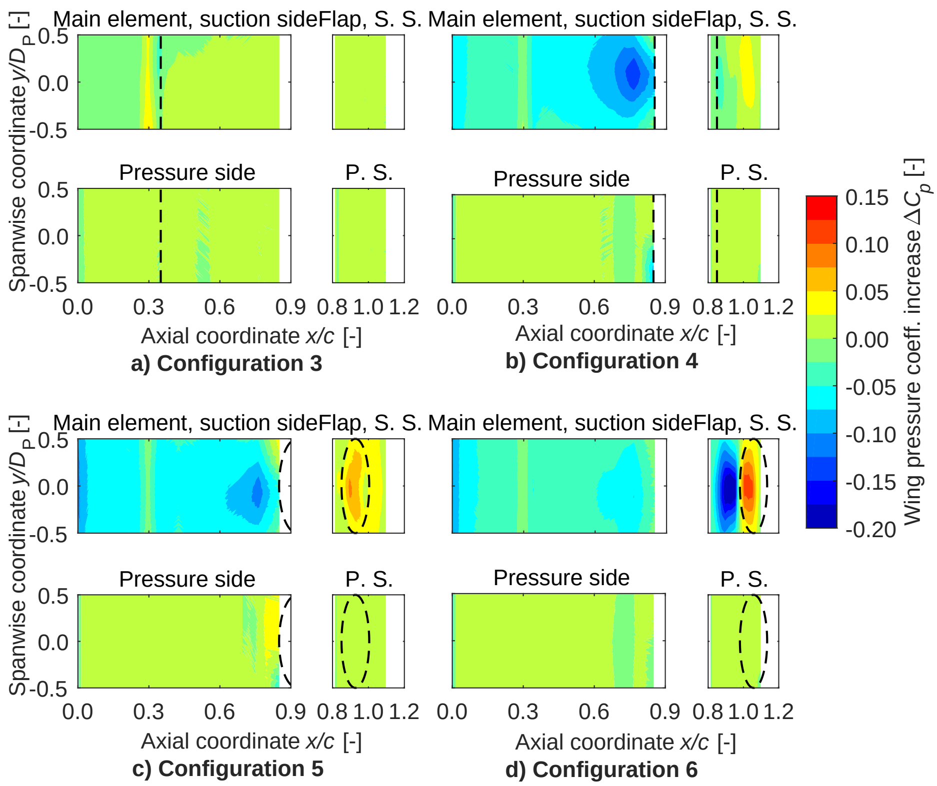

Figure 6.2: Wing pressure distributions at advance ratio $J = 0.7$, Experiment 1 (in climb conditions). Dashed lines indicate projection of propeller disk onto the wing surface.

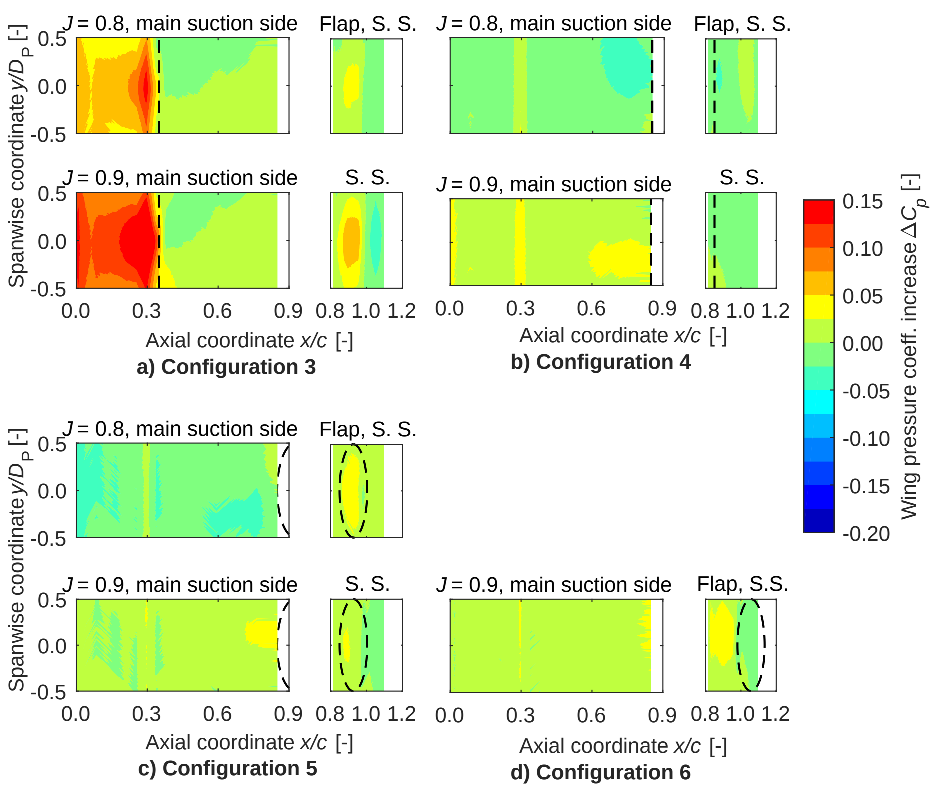

Figure 6.3: Wing suction side pressure distributions Experiment 1 (in climb conditions) at $J = 0.8$ and 0.9. Dashed lines indicate the projection of the propeller disk onto the wing surface. Note that results for Configuration 6 at $J = 0.8$ have not been measured. Furthermore, as opposed to Figure 6.2, only suction side results are shown.

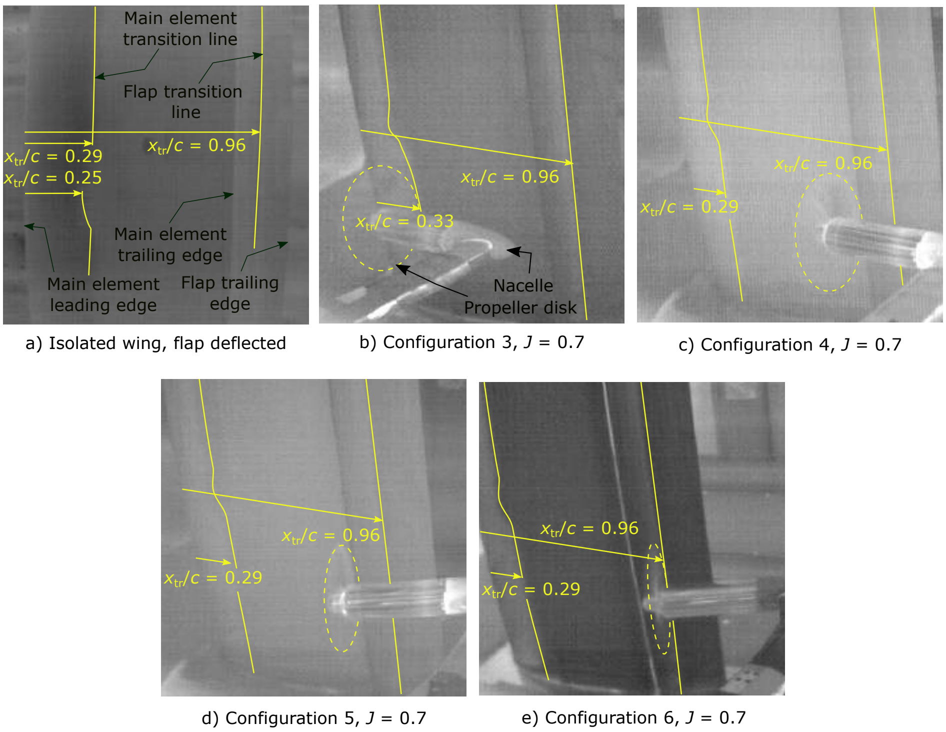

Figure 6.4: The effect of the propeller on boundary layer transition Experiment 1 (in climb conditions).

flap deflection angle used in this study (45°), but may also indicate that the observed flow separation only occurs if the propeller blade penetrates the wing boundary layer.

In Configurations 4 to 6, the nacelle had no effect on the transition location and Figures 6.4c, 6.4d and 6.4e show that this was also the case for the propeller. Since the propeller is slightly upstream of the flap transition location, a similar behaviour to Configuration 1 might have been expected. However, there is a larger distance between the propeller disk and the transition location in Configurations 4 and 5 than in Configuration 1. This further confirms that any viscous effects of the propeller on the wing are limited to a region close to the propeller disk.

Strips of increased pressure can be observed in Figure 6.2 on the suction side at $x/c = 0.3$ for all configurations. The infrared images reveal that this location corresponds to the chordwise location of boundary layer transition in high-lift conditions. Only in Configuration 3, for which this strip shows the strongest difference to the remaining pressure distribution, a significant movement in transition location can be observed. However, a pressure tap was located close behind the transition location, causing a very slight movement in Configurations 4 to 6 to show up very prominently.

6.2.3. PROPELLER EFFECTS ON WING PERFORMANCE

Figure 6.5 shows the lift, drag and pitching moment coefficients as a difference between propeller-on and propeller-off measurements, to remove installation effects. Figure 6.5a shows an increase in lift with decreasing advance ratio, comparable to the effect seen for cruise configurations. However, the lift is decreased in all configurations at $J = 0.9$ and in Configuration 3 also at $J = 0.8$, which is a result of the pressure differentials shown in Figures 6.2 and 6.3. This effect was more pronounced in the high-lift than in the cruise configurations, due to the larger inflow velocities perceived by the propeller when the flap was deflected. Similarly to the cruise configurations, as the advance ratio decreased, the pressure drag did as well, due to the increased suction in front of the wing location with maximum thickness.

Wing lift increases as the propeller moves aft on the wing, similarly to earlier research on an propeller over a wing with a deflected plain flap [20]. However, the wing drag reduction is generally higher for aft-wing axial propeller positions, which is contrary to earlier observations regarding such a configuration [35]. This is a result of the (partial) windmilling of the propeller discussed earlier, which reverses the effects on the wing pressure distribution created by a propeller producing thrust. As a result, the effect on the wing drag is

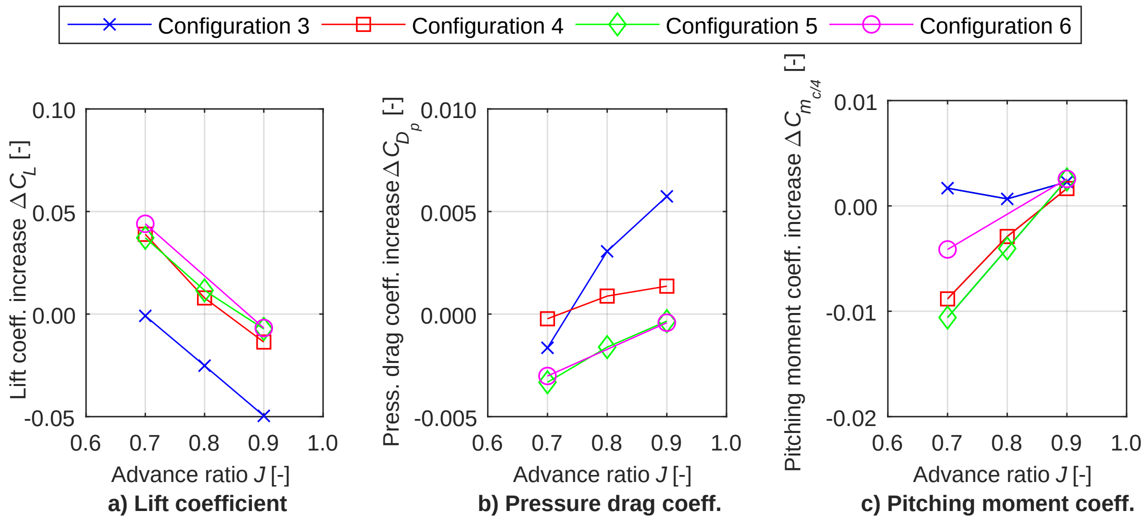

Figure 6.5: Wing lift, pressure drag and pitching moment increase with respect to propeller-off conditions, Experiment 1 (in climb conditions), as a function of advance ratio.

also reversed. Presumably, at a lower propeller advance ratio, the results would have been as expected. The steeper decrease in pressure drag with decreasing advance ratio seen for Configuration 3 compared to the other configurations indicates that this will indeed be likely.

In Configurations 4 to 6, a propeller producing thrust decreased the pitching moment, similarly to cruise Configuration 2. This effect was however weakened as the propeller moved aft, since the pressure increase aft of the propeller increased the pitching moment, and increased in strength in Configurations 4 through 6. In Configuration 3, the (partial) windmilling of the propeller led to a slight increase in pitching moment at all advance ratios.

6.3. WING EFFECTS ON THE PROPELLER

Results of the total pressure measurements of Experiment 1 in the wake plane for the climb configurations at advance ratio $J = 0.7$ are shown in Figure 6.6. Results $J = 0.8$ and 0.9 can be found in Figure 6.7. Even though the isolated propeller was producing thrust up to an advance ratio of more than $J = 1.0$ (see Figure 4.8), when installed over the wing, the propeller was found to be windmilling at advance ratios of up to $J = 0.8$ in Configuration 3. At these advance ratios the total pressure coefficients in the slipstream were lower than in the freestream, indicating that the propeller was extracting energy from the flow over the complete disk. Since flow velocities above the wing decrease as the distance to the wing surface increases, in some cases only the bottom fraction of the propeller was windmilling, while the top part, which had a lower effective advance ratio, was generating thrust, as reflected in Figure 6.6a.

For the same reason, when comparing Figures 5.8c, 6.6a and 6.6b, it can be seen that the thrust was reduced more in Configuration 3 than in Configurations 1 and 4. This is a result of the flow velocities above the wing being higher with the flap deflected and at 35% instead of 85% chord-length. In Figure 6.6b (Configuration 4), the upward-going blade side presents a higher loading than the down-going blade. This is due to the downwardly oriented wing-induced velocities, which follow the local inclination of the airfoil surface. If, on the other hand, the propeller is deflected 23° (Configurations 5 and 6), the angle of attack perceived by the blades is highest on the downward-going side. In both Configurations 5 and 6, the slipstream presents a large vertical displacement due to the inclination of the propeller, and penetrates the wing wake. The total pressure values are higher in Configuration 6 than in Configuration 5, since the propeller is ingesting lower-velocity flow.

Configurations 5 and 6 present higher momentum in the slipstream when compared to Configuration 4. This indicates that deflecting the propeller together with the flap can lead to increased propeller performance in high-lift conditions. Furthermore, in the previous section it was shown that deflecting the propeller together with the flap is also beneficial to wing performance, since it decreases the wing pressure drag significantly. Additionally, the thrust vectoring of the inclined propeller will increase the lift of the whole system.

For these three reasons, more research on a configuration in which the propeller is deflected with the flap is recommended.

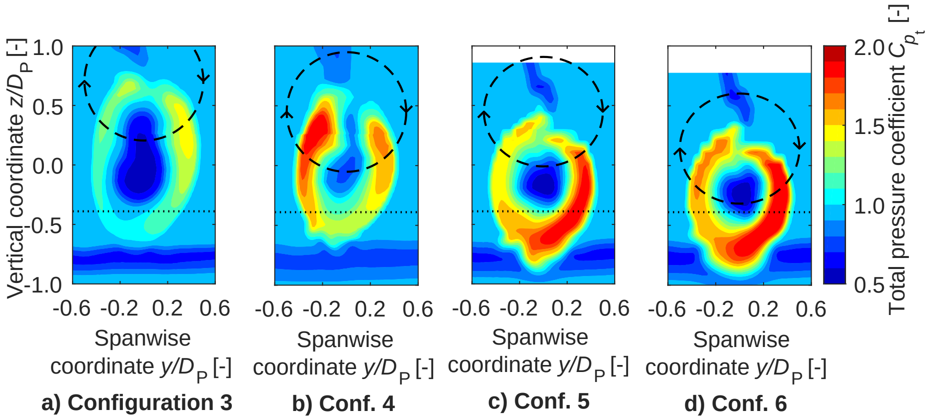

Figure 6.6: Total pressure distributions in the wake plane, Experiment 1 (in climb conditions) at $J = 0.7$. Dashed and dotted lines indicate projections of propeller disk and wing trailing edge, respectively, onto the measurement plane.

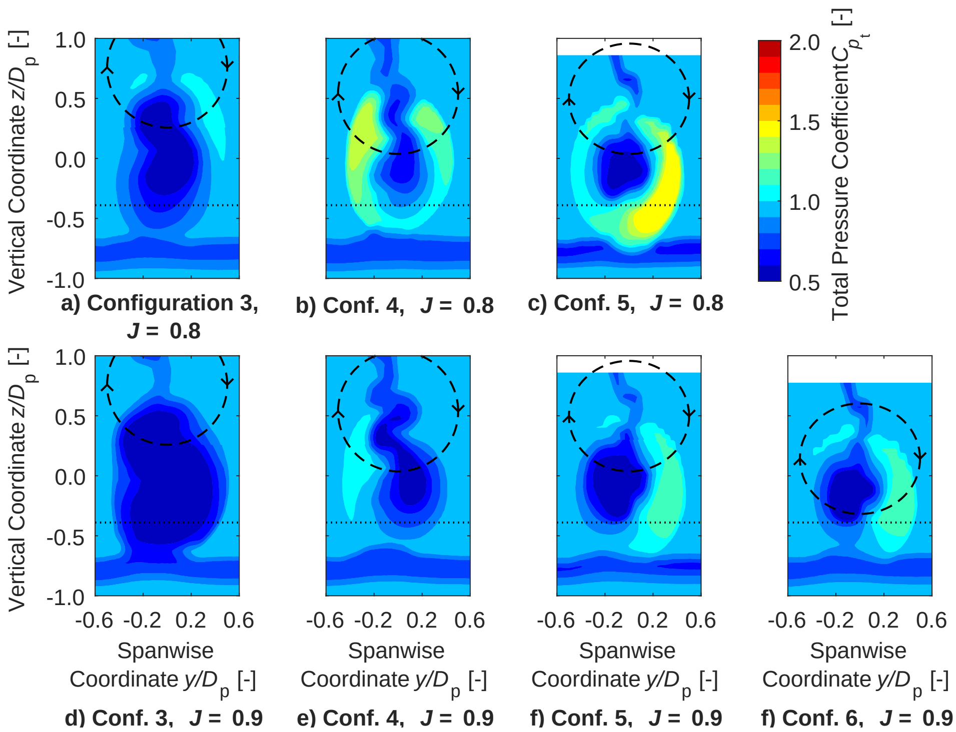

Figure 6.7: Wake plane total pressure distributions Experiment 1 (in climb conditions), at $J = 0.8$ and 0.9. Dashed and dotted lines in the wake plane indicate projections of propeller disk and wing trailing edge, respectively.

7

SENSITIVITY ANALYSES

This chapter demonstrates the applicability of the numerical tool by evaluating the impact of two of the most important design parameters: the axial position and size of the propeller. Section 5.3.2 has shown that the effective advance ratio—and thus, thrust—varies strongly depending on the configuration. Accordingly, the comparison was performed at constant thrust instead of constant advance ratio. Furthermore, for engineering applications, it is more accurate to compare wing drag and propeller efficiency at constant lift, instead of constant angle of attack.

7.1. EFFECT OF PROPELLER AXIAL LOCATION

Figure 7.1 presents the lift coefficient, pressure drag coefficient, and propeller efficiency versus propeller axial position. This is done for four different wing-area-normalized thrust coefficient ($T_C^* = \frac{T}{\rho_\infty U_\infty^2 S_{\text{ref}}}$) values[1]. The lift and pressure drag coefficients are shown as absolute increases, and the propeller efficiency as an increase relative to the isolated propeller efficiency η_{iso} of the propeller-on versus propeller-off simulations. The drag coefficient and propeller efficiency changes are presented at a constant lift, $C_L = 0.5$. Note that the analysis is limited to axial positions aft of $x_{\text{P}}/c = 0.2$, since ahead of this location, the slipstream geometry intersects with the wing surface if the same tip clearance is maintained.

With regards to the axial position of the propeller, several important trends can be distinguished. Firstly, lift is increased further as the propeller moves aft on the wing, due to a larger wing area experiencing the suction in front of the propeller, as explained in Section 5.2. At a high thrust setting ($T_C^* = 0.32$), the lift coefficient is increased by up to $\Delta C_L \approx 0.3$. The effect on pressure drag, on the other hand, is strongly dependent on the axial position of the propeller. At all thrust settings, pressure drag decreases for propeller positions forward of $x_{\text{P}}/c = 0.8$, while increasing aft of this position. The $T_C^* = 0.32$ curve attains a minimum value of $\Delta C_{D_p} = -0.020$ at $x_{\text{P}}/c = 0.3$.

Furthermore, a pressure drag increase is found for an axial propeller position near the wing trailing edge, as opposed to Johnson and White [11], but in agreement with other studies [17, 18, 35]. The axial propeller position that gives the maximum increase in lift is above the wing trailing edge, contrary to the mid-wing position found by Veldhuis [18], but coinciding with other findings [17, 35]. The other trends in lift and drag versus axial propeller position coincide with earlier observations [11, 17, 18, 35].

Surprisingly, at $x_{\text{P}}/c \approx 0.9$ the pressure drag coefficient increase is nearly independent of thrust. This indicates that, at this location, the overall pressure changes on the forward-facing and backward-facing surfaces of the airfoil scale equally with thrust. Finally, the propeller efficiency is lowest near the locations of lowest wing drag, since here the flow velocities above the wing are highest. At $x_{\text{P}} = 0.3$, propeller efficiency is decreased by $\Delta\eta/\eta_{iso} = 0.21$ at $T_C^* = 0.32$. As the propeller moves toward the trailing edge, wing-induced velocities decrease, similarly to the results of Experiment 2 (see Figure 5.12a). The efficiency penalty is reduced to approximately 1% at the trailing edge.

The optimal propeller position in an over-the-wing configuration is thus most importantly a trade-off between wing lift and propeller efficiency versus wing drag. To estimate the optimal axial propeller position,

[1]Note that constant T_C^* was preferred over constant C_T since in the next sensitivity analysis, the propeller diameter will be varied, on which C_T is dependent. Furthermore, the comparison is not done at constant propeller power, since it is assumed that the aircraft requires a certain thrust to maintain forward flight.

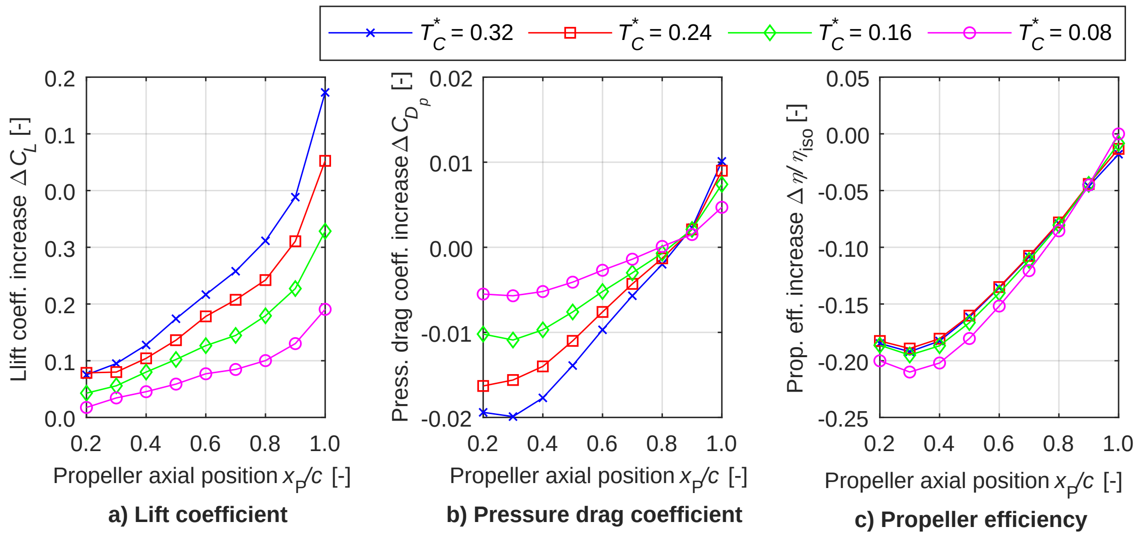

Figure 7.1: Effect of the axial position of the propeller on the (a) lift increase, (b) pressure drag increase, and (c) propeller efficiency increase, with respect to propeller-off conditions. The three parameters are evaluated with the geometry of Experiment 1, at four constant thrust settings, and (b) and (c) at constant lift ($C_L = 0.5$).

an overall system efficiency has to be evaluated. Since the infrared camera showed no large effect on the wing boundary layer, the viscous drag can be assumed to be approximately constant. XFOIL calculations were performed to obtain the viscous drag coefficient of the airfoil at $Re = 1.65$ million. This coefficient is equal to 0.005 for the relevant angle of attack range (1° to 3°). Using this coefficient, the installed system efficiency:

$$\eta_{\text{system}_{\text{installed}}} = \frac{(T - D)U_\infty}{P}, \tag{7.1}$$

i.e. the ratio of net output to input power, can be determined. This system efficiency can be compared to the uninstalled system efficiency, i.e. the system efficiency that would be obtained by the isolated wing and isolated propeller:

$$\eta_{\text{system}_{\text{uninstalled}}} = \frac{(T_{\text{iso}} - D_{\text{iso}})U_\infty}{P_{\text{iso}}}. \tag{7.2}$$

Results are shown in Figure 7.2, for four different thrust coefficients, and at constant lift $C_L = 0.5$. It can be seen that for any axial position, $T_C^* = 0.08$ presents a low system efficiency. This is a result of the pressure drag decrease and propeller efficiency being the lowest at this thrust setting. For $T_C^* = 0.16$ and 0.24, the pressure drag decrease is higher, and the propeller efficiency decrease lower, and correspondingly the system efficiency is increasingly higher. At $T_C^* = 0.32$, the system efficiency is slightly lower again, since the high pressure drag decrease comes at the cost of a lower propeller efficiency.

Installing the propeller above the wing generally decreases the system efficiency, since the loss in propeller efficiency has a higher influence on system efficiency than the reduction in wing drag. This shows that as opposed to using generic propeller and wing geometries, an effective over-the-wing propeller system requires a redesign of the propeller and wing. Furthermore, a duct may improve the system performance (see for example Hongbo et al. [28]) and other benefits, such as noise shielding and thrust vectoring possibilities are not included in this analysis.

At all thrust settings, the installed system efficiency shows local maxima, $x_P = 0.2$ and 0.9. These maxima are near the locations of minimum pressure drag, $x_P = 0.3$, and the location of maximum propeller efficiency, $x_P = 1.0$, respectively[2]. Consequently, a propeller position near the wing trailing edge is recommended, since there the lift increase is highest, while system efficiency is at a maximum. The observed trends in the system efficiency versus axial propeller position agree with earlier findings [18, 20, 35].

[2]It should be noted that it is unknown whether an axial position forward of $x_P = 0.2$ will have a higher system efficiency. However, it has already been explained in Section 5 that such a position will most likely lead to a smaller lift decrease, a higher pressure drag and a reduced propeller efficiency. Earlier research [18, 20, 35] confirms this.

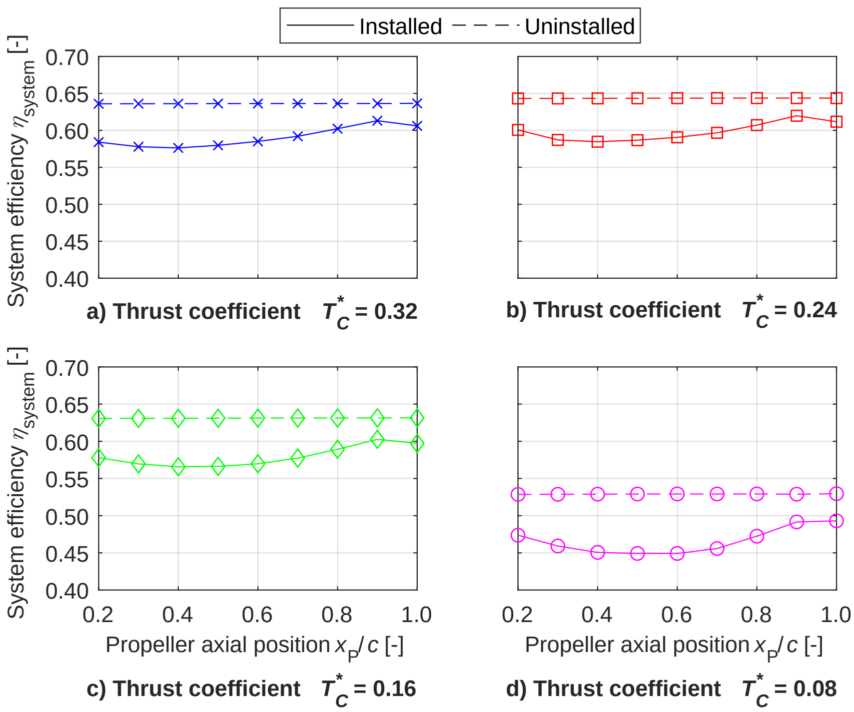

Figure 7.2: Effect of the axial propeller position on installed and uninstalled system efficiency, evaluated with the geometry of Experiment 1, at four constant thrust settings, and at constant lift ($C_L = 0.5$) and a viscous drag coefficient of 0.005.

7.2. EFFECT OF PROPELLER DIAMETER

For distributed-propulsion applications, it is important to analyze the effect of propeller diameter, which can differ considerably depending on the number of propulsors selected. This parameter is difficult to vary experimentally, whereas it is easily changed in numerical simulations. To this end, Figure 7.3 presents ΔC_L, ΔC_{D_p}, and $\Delta\eta/\eta_{iso}$ versus the propeller diameter, expressed as a fraction of the wing chord. The nacelle was scaled with propeller diameter. As a comparison, the propeller-to-chord ratios in Experiment 1 and Experiment 2 were 0.395 and 0.550, respectively.

In the previous section it was shown that system efficiency is maximal at an axial propeller position of $x_P = 0.9$. However, at this location the change in wing pressure drag due to the propeller is very small. In order to make pressure drag changes more visible, the diameter-sensitivity analysis was performed at an axial propeller position of $x_P = 0.95$. The lower bound of the diameter interval is limited by the tip Mach number, which increases considerably for smaller propellers if they have to produce large T_C^* values.

Figure 7.3 shows that, within the interval studied, the three parameters are less sensitive to the propeller diameter than the axial position of the propeller. Nonetheless, it can be seen that wing lift and propeller efficiency are increased as the propeller diameter is reduced, while pressure drag is practically unchanged. This is a result of the top of the propeller being closer to the wing if it has a smaller diameter, leading to slightly stronger changes in the wing pressure distribution. In other words, the smaller streamtubes near the wing surface reduce the three-dimensional relief effect that occurs in the space between the slipstream and the wing. This is contrary to the trend observed for tractor propellers [26]. In the case of the lift, the effect in front of the propeller disk dominates, leading to increased lift with decreasing diameter. On the other hand, the decreased pressure in front of the propeller disk and increased pressure behind it balance each other in terms of pressure drag. Since the top of the propeller disk is closer to the wing, the wing-induced inflow angle of attack is higher, which is beneficial to efficiency. This effect is similar to the effect of decreasing clearance seen in the results of Experiment 2 at $x_P = 0.85$ (see Figure 5.12b).

Figure 7.4 shows the installed and uninstalled system efficiencies, as a function of propeller diameter. The system efficiencies are shown at four thrust settings, again assuming constant viscous drag. It can be seen that at the two highest thrust settings ($T_C^* = 0.24$ and 0.32), system efficiency strongly decreases with decreasing propeller diameter. This decrease in system efficiency is largely due to the reduction in isolated propeller efficiency as the diameter is reduced. Since the propeller advance ratio must decrease to produce the requested

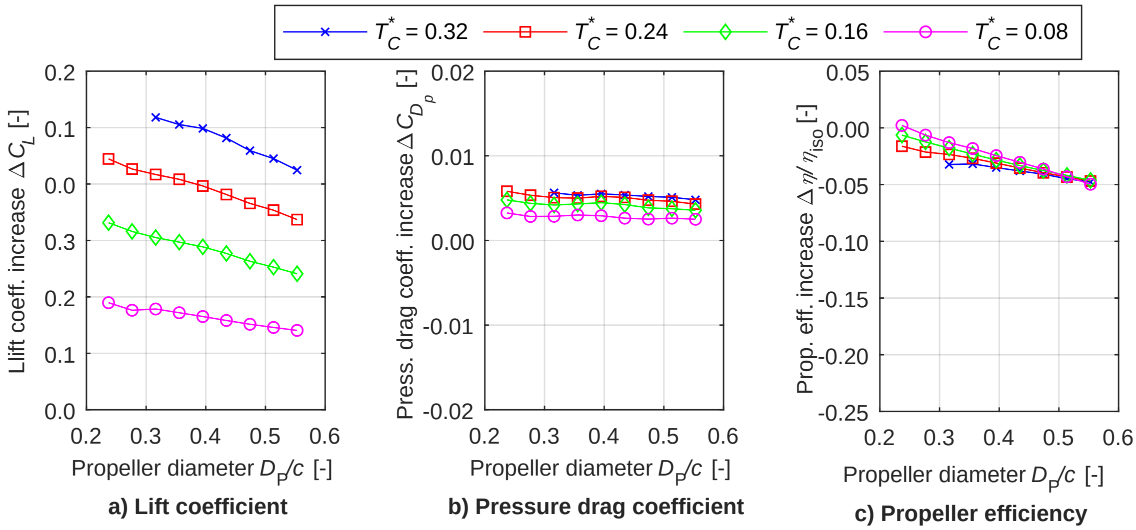

Figure 7.3: Effect of propeller diameter on (a) the wing lift increase, (b) wing pressure drag increase, and (c) propeller efficiency increase, with respect to propeller-off conditions. The three parameters are evaluated at $x_P/c = 0.95$ with the geometry of Experiment 1, for four constant thrust settings, and (b) and (c) at constant lift ($C_L = 0.5$).

thrust, the propeller moves from operational point B towards A in Figure 2.2. At the two lower thrust settings (T^*_C = 0.08 and 0.16), the decrease in propeller diameter initially shifts the propeller from operational point C towards B in Figure 2.2. This leads to an increase in system efficiency up to an optimal propeller diameter, after which the propeller efficiency decreases again with decreasing propeller diameter.

Installing the propeller above the wing generally decreases the system efficiency. Similarly to the previous sensitivity analysis, it should be noted that this may be different for a properly optimized design, and other benefits of the over-the-wing configuration are not included in this analysis. The decrease in system efficiency increases with decreasing thrust setting, since the propeller efficiency loss and wing drag reduction increase and decrease, respectively, with decreasing thrust setting. Increasing the propeller diameter similarly leads to a higher system efficiency loss when installing the propeller. At T^*_C = 0.16 and 0.08, there are optima near $D_P \approx 0.45$ and 0.3, respectively. Thus, propellers with a smaller diameter are only beneficial to the system if the requested thrust is distributed among a larger number of propellers. In this case, disk area, advance ratio and thus isolated propeller efficiency can be kept constant. As a result, system efficiency is increased if propeller diameter is reduced.

Note that the previous conclusion is specifically for the axial position considered in Figure 7.3, $x_P/c = 0.95$. At this location, the velocity gradient at the propeller disk is relatively small, and the negative inflow angle has a positive effect on propeller efficiency [41]. If the propeller were positioned at, for example, $x_P/c = 0.35$, the propeller efficiency would likely decrease as the propeller diameter is reduced, due to the higher inflow velocities closer to the wing. The propeller diameter also has a larger impact on pressure drag if the propeller is positioned at a different axial location.

In this case it is not possible to attain the system efficiency of a propeller with a larger diameter at a higher thrust setting. It should however be noted that this simulation features a single over-the-wing propeller, whereas the increase in lift is larger for a distribution of over-the-wing propellers [21]. To assess the effect of an distributed over-the-wing propeller configuration, it is thus recommended to extend the tool's applicability by implementing symmetrical boundary conditions at the wing spanwise locations $y = \pm D_P/2$.

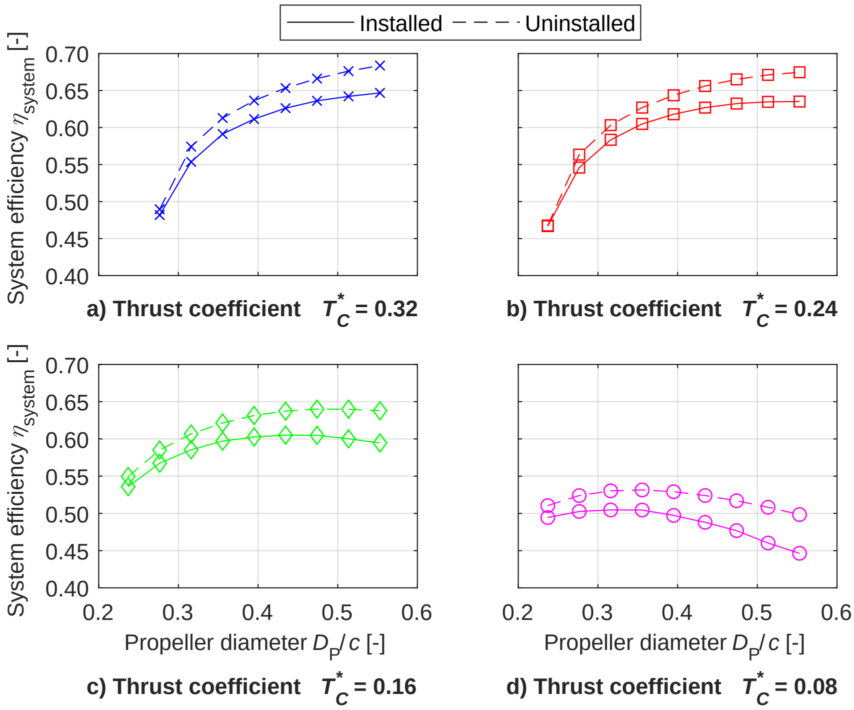

Figure 7.4: Effect of the propeller diameter on installed and uninstalled system efficiency, evaluated at $x_P/c = 0.95$ with the geometry of Experiment 1, for four constant thrust settings, and at constant lift ($C_L = 0.5$) and a viscous drag coefficient of 0.005.

8

Conclusion and recommendations

8.1. Conclusions

Two wind tunnel experiments have been carried out and a numerical method has been developed to study over-the-wing propeller aerodynamic interaction effects. The findings were used to answer the research questions in Section 1.2:

1. *What are the dominant aerodynamic flow phenomena for an over-the-wing propeller?*

   (a) *How does the propeller affect the wing pressure distribution?*

   The first experiment confirmed earlier findings: the propeller decreases the pressure on the wing surface upstream of the propeller disk, while decreasing the pressure behind it. The numerical simulation showed that this was caused by the propeller accelerating flow axially upstream of the propeller disk. On the other hand, downstream of the propeller disk flow was decelerated axially due to the slipstream surface diverging from the wing surface.

   However, increased inflow velocities at the propeller disk, produced by the wing, may lead to the propeller (partially) windmilling, leading a pressure increase upstream of the propeller disk and a pressure decrease downstream of it. Additionally, the nacelle was also found to have a significant effect on the pressure distribution. Similarly to a partially windmilling propeller, the nacelle increased the pressure upstream of the propeller disk, and decreased it behind it.

   Regarding viscous effects, the propeller was only shown to have a significant influence on wing boundary layer transition if the propeller or nacelle were positioned close to the transition location. With the propeller disk slightly upstream of the transition location, the nacelle delayed transition, whereas the propeller caused transition to occur further upstream. Positioning the propeller slightly downstream of the transition location delayed transition.

   (b) *In which way does the wing affect the propeller disk loading?*

   The effect of the wing on the propeller disk loading is strongly dependent on the axial propeller position. In general, the wing induces axial velocities at the propeller disk, leading to a reduced disk loading. This effect is strongest for mid-wing positions. Furthermore, a mid-wing axial propeller position leads to a vertical loading gradient in which the top of the propeller disk has a higher loading. This is a result of a strong vertical gradient in the wing-induced velocity magnitude.

   An aft-wing axial propeller position leads to an inflow with a downward component, since the wing-induced velocity component is aligned with the wing surface. Accordingly, the loading on the up-going blade side is higher than on the downward-going blade side. The wing flow field thus significantly alters propeller blade angles of attack, indicating that effective operation requires a redesign of the propeller compared to a tractor configuration.

   (c) *How does the wing deform the propeller slipstream?*

   The wing-induced velocity component accelerates the slipstream axially. This axial acceleration is strongest close to the wing surface, leading to the bottom of the slipstream traveling downstream faster than the top. Secondly, the wing-induced velocity component has a downward component, leading to downward movement of the slipstream. This downward movement is also stronger close to the wing surface, leading to vertical stretching of the slipstream.

2. *How does the performance of over-the-wing systems compare to the isolated wing and propeller performances?*

   (a) *In which way does the propeller affect the wing lift, drag and pitching moment in cruise conditions?*
   In cruise configurations, it has been shown that an over-the-wing propeller significantly increases wing lift. The lift increase is strongest for axial propeller positions toward the wing trailing edge. The change in wing pressure drag was shown to be strongly dependent on axial propeller position. With the propeller near the trailing edge, it was slightly increased, whereas it decreased for mid-wing propeller positions. Pitching moment increased for mid-wing propeller positions, while it decreased for aft-wing propeller positions. Furthermore, the propeller nacelle was observed to decrease lift and increase pressure drag.

   (b) *What effects does the wing have on the propeller thrust, torque and efficiency in cruise conditions?*
   In the cruise configurations, it was shown that an over-the-wing position leads to decreased propeller thrust, torque and efficiency. This is a result of the increased axial inflow velocity above the wing, and the non-uniform loading distribution. Moreover, it has been shown that mid-wing and aft-wing positions led to significant side and normal forces, respectively, on the propeller.

   (c) *In which way does the propeller affect the wing lift, drag and pitching moment in high-lift conditions?*
   In high-lift configurations, the propeller generally increased the wing lift and reduced its pressure drag. The wing's pitching moment was also decreased. The nacelle and operating conditions in which the propeller was (partially) windmilling led to the opposite effects on wing performance.

   (d) *What effects does the wing have on the propeller thrust, torque and efficiency in high-lift conditions?*
   Wake plane pressure distributions showed that in high-lift over-the-wing configurations, the propeller thrust was reduced. This was however only shown qualitatively, and it is unknown what the effect on the propeller torque and efficiency are.

3. *Which parameters govern the performance of the system?*

   (a) *How are wing and propeller performances affected by propeller thrust setting?*
   The changes in wing lift, drag and pitching moment generally increased with decreasing propeller advance ratio. For low propeller advance ratios, it was found that the propeller was partially windmilling close to the wing surface, leading to reversed effects on the wing pressure distribution and its performance coefficients. On the other hand, the wing effect on the propeller generally decreased with decreasing advance ratio.

   (b) *What is the effect of chordwise propeller position?*
   The effect of axial propeller position on wing performance in cruise configurations was already discussed in Answer 2a. Furthermore, the propeller thrust, torque and efficiency reductions in cruise configurations are lower as the propeller moves aft on the wing. The resulting system performance was found to be highest for an axial propeller position near the wing trailing edge.

   In high-lift configurations, the axial propeller position has a strong effect on the propeller's effective advance ratio. As a result, for a mid-wing position, wing lift and pressure drag were found to be decreased and increased, respectively, as opposed to the general trend observed in Answer 2c. Similarly to the cruise configurations, the decreases in propeller thrust became increasingly large as the propeller moved forward on the wing.

   (c) *What is the effect of propeller diameter?*
   Assuming constant thrust at an aft-wing propeller position, the wing lift increase and propeller efficiency increase increased and decreased, respectively, with decreasing propeller diameter. However, since the isolated propeller efficiency generally decreases with decreasing propeller diameter, system efficiency will only increase with decreasing propeller diameter if thrust is distributed among a larger number of propellers.

   It is however not possible to obtain the system efficiency of a propeller with a larger diameter at a higher thrust setting. To determine if this is limited to a single propeller or if this is also the case for a distributed over-the-wing propeller configuration, the applicability of the numerical tool should be extended.

(d) *What is the effect of clearance between propeller and wing?*

The effect of clearance between the propeller and wing is dependent on the axial propeller position. For mid-wing positions, the thrust, torque and efficiency reductions were found to increase with decreasing clearance, whereas the opposite effect was seen for an aft-wing position. To determine the effect of the clearance on the wing performance, a numerical sensitivity analysis should still be performed.

4. *How can the performance of over-the-wing propellers be determined in a preliminary design phase?*

(a) *What are computationally effective ways to model the propeller, its slipstream and the wing?*

A numerical tool has been developed which models the wing with a panel method, the propeller by a blade element method adapted for non-uniform inflow and the propeller slipstream by a vortex lattice method. The determination of the slipstream geometry includes wing-induced deformation and movement of the slipstream.

(b) *In which way can the propeller and wing flow fields be coupled?*

The propeller-wing interaction is modeled by computing the wing-induced velocities at the propeller disk and the propeller-induced velocities at the wing surface. These induced velocities are taken into account during the solution of the blade element and panel methods, respectively. The individual components of the solver are iteratively run until the induced velocities are within a user-set convergence value of their values in the previous iteration.

Promising results have been obtained for a propeller located at 85% of the wing chord. In this position, with the flap is retracted, the pressure drag is increased by approximately 2 counts and wing lift is improved by 8%, with respect to an isolated wing. In high-lift conditions (flap deflected), wing lift increased by 3% and the pressure drag is reduced by 3 counts. These values are conservative, since the benefits in terms of wing lift and pressure drag were found to increase with decreasing advance ratio.

With the propeller at 85% of the chord, propeller thrust and efficiency decreases in a cruise configuration were limited. At the advance ratio for optimal efficiency, they decreased by approximately 1.5% and 5.7%, respectively, almost independent of propeller clearance. Moreover, deflecting the propeller together with the flap in this position leads to improved propeller performance when compared to the same propeller without deflection. Additionally, the wing lift increase and pressure drag decrease were higher when the propeller was deflected, and the thrust-vectoring enhances lift, which improves climb performance.

The low-fidelity numerical tool, which can determine the performance of over-the-wing propeller systems, has been validated by comparing to the experimental results. It is currently limited to cruise configurations, and has shown to capture the most important aerodynamic interaction effects. However, for mid- and aft-wing positions, the effect of the propeller on the wing is under- and overestimated, respectively. Furthermore, the effect of the wing on propeller thrust, torque and efficiency at low and intermediate advance ratio is overestimated. The tool was also compared to higher-fidelity numerical simulations, which showed that it performed remarkably well, especially considering its significantly lower computational cost.

The experimental results show that it is possible to design over-the-wing propellers which significantly enhance wing performance, with limited losses in propeller performance. Besides supporting the conclusions drawn during the wind tunnel campaign and giving more insight into the experimental results, the numerical tool allows rapid design-space explorations of over-the-wing propeller configurations and is thus very suitable for conceptual aircraft design.

8.2. RECOMMENDATIONS

The two wind tunnel experiments have shown that the complex aerodynamic interaction effects between a wing and an over-the-wing propeller have a significant effect on the system performance. Furthermore, a numerical model to simulate over-the-wing propeller configurations was succesfully developed and shown to be applicable in the conceptual design phase of aircraft. However, several improvements and recommendations for future research can be made.

Firstly, although it has been shown that the system efficiency loss can be minimized by choosing the optimal propeller axial position on the wing, over-the-wing propeller configuration system efficiency can still be further improved in several ways. In this thesis, the propellers and wings that have been used are designed to have a high isolated or tractor configuration performance. The strong aerodynamic interaction effects for over-the-wing configurations indicate that an optimal design requires a geometric redesign of both propeller and wing. Additionally, recent research [28, 71] indicates that the system performance of over-the-wing propeller systems may be signficantly increased by placing a smaller wing above the propeller. Although the wing above the propeller comes at the cost of increased drag, it reduces the inflow velocities to the propeller, which increases propeller efficiency. As a result, system efficiency can be increased [71], which is exploited by ONERA's AMPERE [23] and the Lilium Jet (https://lilium.com/).

Secondly, a sensitivity analysis on the effect of clearance between the propeller and wing should still be performed. It is expected, and found in earlier research [20] that the effect of the propeller on wing performance increases with decreasing clearance. This research also shows that the system efficiency decreases with decreasing clearance for a mid-wing position. It is however unknown what the effect of clearance on system performance is for an aft-wing position.

Based on the findings of this study, another future research possibility on over-the-wing propellers is their performance in high-lift conditions. While it was shown that wing performance in such a configuration can be improved, it is unclear how propeller performance (e.g. thrust and efficiency) is affected quantitatively, especially if the propeller is deflected with the flap for thrust-vectoring. Since it was shown that a configuration in which the propeller is deflected together with the flap has several performance benefits, more research on such a configuration is recommended. Moreover, a model to rapidly estimate the performance of such a high-lift setup is still unavailable. Lastly, an earlier study has indicated that boundary layer separation may lead to a significant deterioration of high-lift configuration performance [19]. It is uncertain if this is specific to the channel wing and high flap deflection in this research and if this can be prevented by, for example, increasing the clearance between propeller and wing.

Another research subject that can be pursued is the performance of propellers subjected to non-uniform inflow conditions. By a better understanding of wing-induced inflow on propeller performance, the propeller shape can be optimized to improve its performance in certain positions above the wing. It is also important to gain more insight into the production of vibrations and increased noise due to the changed inflow. Thirdly, the estimation of the coupled model normal and side forces must still be validated, for example by comparison to experimental or CFD results.

More research can also be done on the installation of over-the-wing propellers. In particular, little is known on the structural limitations involved in over-the-wing propeller configurations. Furthermore, the first experiment has shown that the nacelle has a significant effect on wing performance, and this is also expected to be the case for any pylon to attach the propeller to the wing. The effects of possible installations on the aerodynamic performance should be further quantified, leading to suggestions on the design and optimisation of the system.

Additionally, the numerical model can be improved in several ways. Firstly, the numerical model should be adapted to incorporate boundary layer effects. This could for example be done by dividing the wing into strips and determining the effective airfoil shape with the found pressure distributions, using an inverse design method. Then, a viscous solution could be found with this effective shape. This would lead to a more accurate representation of the pressure distribution and would provide viscous drag results. Secondly, the numerical method should be elaborated to include the effect of multiple propellers. This can be done by adapting the panel and slipstream vortex lattice methods to use symmetry planes at the spanwise ends of the wing segment under the propeller. Lastly, the blade element method has shown to be inaccurate at high advance ratio, which can be remedied by modelling Reynolds number effects. The resulting method will be invaluable in the conceptual design phase of radical aircraft concepts featuring over-the-wing distributed propeller configurations.

Bibliography

[1] Kim, H. D., "Distributed Propulsion Vehicles," International Congress of the Aeronautical Sciences, Nice, France, 2010.

[2] Sehra, A. K. and Whitlow, W., "Propulsion and power for 21st century aviation," *Progress in Aerospace Sciences*, Vol. 40, No. 4-5, 2004, pp. 199–235.

[3] Bonet, J.T., Schellenger, H.G., Rawdon, B.K., Elmer, K.R., Wakayama, S.R., Brown, D.L. and Guo, Y., "N+2 Advanced Vehicle Concepts Study and Conceptual Design of Subscale Test Vehicle (STV)," Environmentally Responsible Aviation (ERA) Project, 2011.

[4] Advisory Council for Aviation Research and Innovation in Europe (ACARE), "Realising Europe's Vision for Aviation: Strategic Research & Innovation Agenda, Volume 1," Advisory Council for Aviation Research and Innovation in Europe (ACARE), 2012.

[5] Isikveren, A. T., Pornet, C., Vratny, P. C., and Schmidt, M., "Optimization of Commercial Aircraft Using Battery-Based Voltaic-Joule/Brayton Propulsion," *Journal of Aircraft*, Vol. 54, No. 1, 2017, pp. 246–261.

[6] Borer, N. K., Derlaga, J. M., Deere, K. A., Carter, M. B., Viken, S. A., Patterson, M. D., Litherland, B. L., and Stoll, A. M., "Comparison of Aero-Propulsive Performance Predictions for Distributed Propulsion Configurations," 55th AIAA Aerospace Sciences Meeting, Grapevine, TX, USA, 2017.

[7] Pornet, C. and Isikveren, A. T., "Conceptual design of hybrid-electric transport aircraft," *Progress In Aerospace Sciences*, Vol. 79, 2015, pp. 114–135.

[8] Felder, J. L., Kim, H. D., and Brown, G. V., "Turboelectric Distributed Propulsion Engine Cycle Analysis for Hybrid-Wing-Body Aircraft," 47th AIAA Aerospace Sciences Meeting, Orlando, FL, USA, 2009.

[9] Beck, S. C., Müller, L., and Langer, S. C., "Numerical assessment of the vibration control effects of porous liners on an over-the-wing propeller configuration," *CEAS Aeronautical Journal*, Vol. 7, No. 2, 2016, pp. 275–286.

[10] Broadbent, E. G., "Noise shielding for aircraft," *Progress In Aerospace Sciences*, Vol. 17, 1977, pp. 231–268.

[11] Johnson Jr., J. L. and White, E. R., "Exploratory Low-Speed Wind-Tunnel Investigation of Advanced Commuter Configurations Including an Over-the-Wing Propeller," AIAA Aircraft Design, Systems and Technology Meeting, Fort Worth, TX, USA, 1983.

[12] Müller, L., Heinze, W., Kožulović, D., Hepperle, M., and Radespiel, R., "Aerodynamic Installation Effects of an Over-the-Wing Propeller on a High-Lift Configuration," 30th AIAA Applied Aerodynamics Conference, New Orleans, LA, USA, 2000.

[13] Torenbeek, E. and Wittenberg, H., *Flight physics: Essentials of aeronautical disciplines and technology, with historical notes*, Springer, Dordrecht, 2009.

[14] "Dornier Do-X," http://www.shu-aero.com/AeroPhotos_Shu_Aero/Aircraft_C/Dornier/Do_X_01_large.jpg, accessed December 2017.

[15] "Custer's Channel Wing," https://tse2.mm.bing.net/th?id=OIP.ku9KCZhUmKHnkdC7fzzDrwHaE1&pid=Api, accessed December 2017.

[16] "Izdeliye 181," https://upload.wikimedia.org/wikipedia/commons/c/ce/Antonov_Izdeliye_181.jpg, accessed December 2017.

[17] Cooper, R. K., McCann, W. J., and Chapleo, A. Q., "Over wing propeller aerodynamics," 18th Congress of the International Council of the Aeronautical Sciences, Beijing, China, 1992.

[18] Veldhuis, L. L. M., *Propeller Wing Aerodynamic Interference*, Ph.D. thesis, TU Delft, 2005.

[19] Müller, L. and Friedrichs, J., "Unsteady Flow Simulations of an Over-the-Wing Propeller Configuration," 50th AIAA Joint Propulsion Conference, Cleveland, OH, USA, 2014.

[20] Müller, L., Hepperle, M., and Radespiel, R., "The Influence of the Propeller Position on the Aerodynamics of a Channel Wing," 61er Deutscher Luft- und Raumfahrtkongress, Berlin, Germany, 2012.

[21] Fischer, J., *Analysis of an over-the-wing based dsitributed propulsion system*, Master's thesis, TU Delft, 2017.

[22] Magliozzi, B., Hanson, D. B., and Amiet, R. K., "Propeller and Propfan Noise," NASA Langley Research Center, Aeroacoustics of Flight Vehicles: Theory and Practice, Volume 1: Noise Sources, pp. 1-64, 1991.

[23] Hermetz, J., Ridel, M., and Doll, C., "Distributed electric propulsion for small business aircraft a concept-plane for key-technologies investigations," 2016.

[24] "ONERA AMPERE," http://i.f1g.fr/media/figaro/orig/2017/06/20/XVMd51d1638-4f6d-11e7-92a8-9c5efd70ddb0.jpg, accessed March 2018.

[25] "Lilium Jet," https://www.designboom.com/wp-content/uploads/2016/06/lilium-electric-aircraft-concept-designboom-bheader1.jpg, accessed March 2018.

[26] Patterson, M. D., *Conceptual Design of High-Lift Propeller Systems for Small Electric Aircraft*, Ph.D. thesis, Georgia Institute of Technology, 2016.

[27] Alba, C., Elham, A., Veldhuis, L., and German, J. G., "A Surrogate-Based Multi-Disciplinary Design Optimization Framework Exploiting Wing-Propeller Interaction," 18th AIAA/ISSMO Multidisciplinary Analysis and Optimization Conference, Denver, CO, USA, 2017.

[28] Hongbo, W., Xiaoping, Z., and Zhou, Z., "Numerical Simulation of the Propeller/Wing Interactions at Low Reynolds Number," 30th Congress of the International Council of the Aeronautical Sciences, Daejeon, Korea, 2016.

[29] Wald, Q. R., "The aerodynamics of propellers," *Progress in Aerospace Sciences*, Vol. 42, No. 2, 2006, pp. 85–128.

[30] Rankine, W. J. M., *On the mechanical principles of the action of propellers*, Institution of Naval Architects, London, 1865.

[31] McCormick, B. W., *Aerodynamics, aeronautics, and flight mechanics*, J. Wiley, New York, 1979.

[32] Luijendijk, A. P. M., "Propeller-wing interference study for over the wing positioned propeller configurations," Master thesis, TU Delft, 2002.

[33] Prandtl, L., "Mutual influence of wings and propeller, NACA Technical Report No. 74," National Advisory Committee for Aeronautics, Extract from the first report of the Gottingen Aerodynamic Laboratory, Chap. IV, Sec. 6, 1921.

[34] Wisda, D., Murray, H., Alexander, W. N., Nelson, M. A., and Devenport, W., "Flow distortion and noise produced by a thrusting rotor ingesting a planar turbulent boundary layer," 21st AIAA/CEAS Aeroacoustics Conference, Dallas, TX, USA, 2017.

[35] Müller, L., Kožulović, D., and Radespiel, R., "Aerodynamic performance of an over-the-wing propeller configuration at increasing Mach number," *CEAS Aeronautical Journal*, Vol. 5, No. 3, 2014, pp. 305–317.

[36] Kroo, I., "Propeller-wing integration for minimum induced loss," *Journal of Aircraft*, Vol. 23, No. 7, 1986, pp. 561–565.

[37] Wick, A., Hooker, J. R., Hardin, C. J., and Zeune, C. H., "Integrated aerodynamic benefits of distributed propulsion," 2015.

[38] Perry, A., Ansell, P., and Kerho, M., "Aero-propulsive and propulsor cross-coupling effects on a distributed propulsion system," 2018 AIAA Aerospace Sciences Meeting, Kissimmee, FL, USA, 2018.

[39] Stoll, A. M., Bevirt, J., Moore, M. D., Fredericks, W. J., and Borer, N. K., "Drag Reduction Through Distributed Electric Propulsion," 14th AIAA Aviation Technology, Integration, and Operations Conference, Atlanta, USA, 2014.

[40] Catalano, F. M., "On the Effects of an Installed Propeller Slipstream on Wing Aerodynamic Characteristics," *Acta Polytechnical*, Vol. 44, No. 3, 2004, pp. 8–14.

[41] Veldhuis, L. L. M., Berkel, E. V., Kotsonis, M., and Eitelberg, G., "Non-Uniform Inflow Effects on Propeller Performance," 31st AIAA Applied Aerodynamics Conference, San Diego, USA, 2013.

[42] Maunsell, M. G., "A study of propeller-wing-body interference for a low speed twin-engined pusher configuration," ICAS-90-5.4.3, Stockholm, Sweden, 1990.

[43] Berguin, S. H. and Mavris, D. N., "Interactions in Over-Wing Nacelle Optimization," 51st AIAA Aerospace Sciences Meeting, Grapevine, TX, USA, 2013.

[44] Szodruch, J. and Kotschote, J., "On the aerodynamics of over-the-wing nacelles supported on 'stub-wings'," 21st Aerospace Sciences Meeting, Reno, NV, USA, 1983.

[45] Szodruch, J. and Kotschote, J., "Wind tunnel tests of over-the-wing nacelles," *Journal of Aircraft*, Vol. 20, No. 7, 1983, pp. 606–611.

[46] Reubush, D. E., "Effect of Over-the-Wing Nacelles on Wing-Body Aerodynamics," *Journal of Aircraft*, Vol. 16, No. 6, 1979, pp. 359–365.

[47] Sasaki, D. and Nakahashi, K., "Aerodynamic optimization of an over-the-wing-nacelle-mount configuration," *Modelling and Simulation in Engineering*, Vol. 2011, 2011.

[48] Hooker, J. R., Wick, A., Zeune, C., and Agelastos, A., "Over Wing Nacelle Installations for Improved Energy Efficiency," 31st AIAA Applied Aerodynamics Conference, San Diego, CA, USA, 2013.

[49] Hill, G. A. and Kandil, O. A., "Aerodynamic Investigations of an Advanced Over-the-Wing Nacelle Transport Aircraft Configuration," *Journal of Aircraft*, Vol. 46, No. 1, 2009.

[50] Berguin, S., Ashwin Renganathan, S., Ahuja, J., Chen, M., Tai, J., and Mavris, D. N., "Sensitivity analysis of aero-propulsive coupling for over-wing-nacelle concepts," 2018 AIAA Aerospace Sciences Meeting, Kissimmee, FL, USA, 2018.

[51] Veldhuis, L. L. M., "Configuration and Propulsion aerodynamics research on the Low Speed Aerodynamics laboratory (in Dutch), Review of project 90-LR-5-S," Internal Report LSW 93-1, Fac. of Aerospace Engineering, Delft University of Technology, 1993.

[52] Boermans, L. M. M. and Rutten, P. B., "Two-dimensional Aerodynamic Characteristics of Airfoil NLF-MOD22 with Fowler Flap," TU Delft Internal Report LSW-95-3, 1995.

[53] Jansen, D. P., *Passive Flow Separation Control on an Airfoil-Flap Model*, Master's thesis, TU Delft, 2012.

[54] Sinnige, T., de Vries, R., Della Corte, B., Avallone, F., Ragni, D., Eitelberg, G., and Veldhuis, L. L. M., "Unsteady Pylon Loading Caused by Propeller-Slipstream Impingement for Tip-Mounted Propellers," *Journal of Aircraft*, in press.

[55] Garner, H. C., Rogers, E., Acum, W., and Maskell, E., "Subsonic wind tunnel wall corrections," *AGARDograph, AG-109*, 1966, p. 466.

[56] Goett, H. J., "Experimental Investigation of the Momentum Method for Determining Profile Drag," NACA Report 660, 1939.

[57] Nahuis, B. and Sinnige, T., "Design, manufacture and commissioning of a new NLR six-component rotating shaft balance for Delft University of Technology," 10th International Symposium on Strain-Gauge Balances, Mianyang, China, 2016.

[58] Sinnige, T., personal communication.

[59] Katz, J. and Plotkin, A., No. February 2013, McGraw-Hill, New York, 1991.

[60] Box, W. and Hoeijmakers, H., "Toepassing van de FASD panelenmethode voor de predictie van het drukveld opgewekt door een passerende trein," TU Eindhoven, 1994.

[61] van den Berg, B. and Gooden, J., "Low-speed surface pressure and boundary layer measurement data for the NLR 7301 airfoil section with trailing edge flap," *A selection of experimental test cases for the validation of CFD codes, AGARD advisory report No. 303, Volume II*, 1994.

[62] Drela, M., "XFOIL 6.9 User Primer," 2001, http://web.mit.edu/drela/Public/web/xfoil/xfoil_doc.txt, accessed October 2017.

[63] Snel, H., Houwink, R., and Bosschers, J., "Sectional prediction of lift coefficients on rotating wind turbine blades in stall," Tech. Rep. ECN-C-93-052, National Aerospace Laboratory (NLR), Netherlands, 1994.

[64] Dorfling, J. and Rokhsaz, K., "Integration of Airfoil Stall and Compressibility Models into a Propeller Blade Element Model," *Journal of Aerospace Engineering*, Vol. 29, No. 04016014, 2016, pp. 1–14.

[65] Rwigema, "Propeller blade element momentum theory with vortex wake deflection," 27th International Congress of the Aeronautical Sciences, Nice, France, 2010.

[66] McLemore, H. C. and Cannon, M. D., "Aerodynamic investigation of a four-blade propeller operating through an angle-of-attack range from 0° to 180° ," National Advisory Committee for Aeronautics, Technical Note 3228, 1991.

[67] Anderson, J. D., *Fundamentals of aerodynamics*, McGraw-Hill, New York, 5th ed., 2006.

[68] van Beek, C. M., Piers, W. J., and Oskam, B., "Aerodynamic Analysis of Slipstream/Wing/Nacelle Interference for Preliminary Design of Aircraft Configurations," *AGARD CP 498*, 1991.

[69] de Young, J., "Propellers at High Incidence," *Journal of Aircraft*, Vol. 2, No. 8, 1965, pp. 241–250.

[70] Acheson, D., No. March 1990, Oxford University Press, New York, 1990.

[71] Khajehzadeh, A., *Simulation and analysis of the aerodynamic interactions between distributed propellers and wings*, Master's thesis, TU Delft, 2018.

[72] Schlichting, H., McGraw-Hill, New York, 1979.

[73] Biermann, D. and Hartman, E.P., "Tests of Five Full-Scale Propellers in the Presence of a Radial and a Liquid-Cooled Engine Nacelle, Including Tests of Two Spinners," NACA Report No. 642, 1938.

[74] Dimchev, M., *Experimental and numerical study on wingtip mounted propellers for low aspect ratio UAV design*, Master's thesis, TU Delft, 2012.

[75] Wassink, J., "Blowin' in the wind," *Delft Outlook*, Vol. 3, 2008.

IV

Appendices

A

WING GEOMETRIES

The experiments and simulations featured several wings, for which airfoil coordinates will be presented for reference and to reproduce results if necessary. Figure A.1 presents a detailed plot of the NLF-MOD22B airfoil, with pressure holes used in the Experiment 1 indicated. The kink in the main element lower surface of this airfoil improves cruise performance, due to the smoother lower surface with the flap retracted [52]. However, this surface discontinuity prevented the numerical model from converging. For this reason, the smoother version of the main airfoil, NLF-MOD22A, as depicted in the same figure, was also used. In Experiment 2, the wing with airfoil coordinates shown in Figure A.2 was used. More information on this wing was not available at the time of writing. Coordinates of the wing airfoils used in the experiments can be found in table A.1.

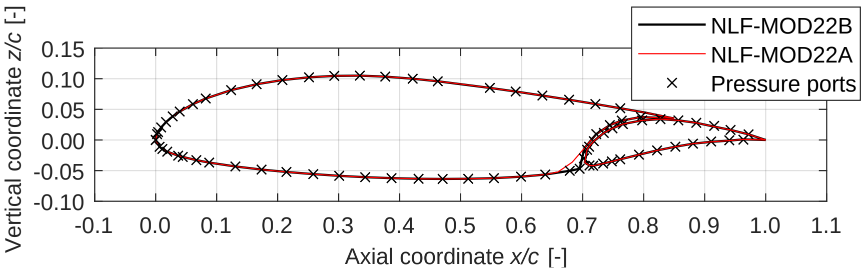

Figure A.1: NLF-MOD22B and -A airfoil plots, with markers indicating the locations of the pressure holes.

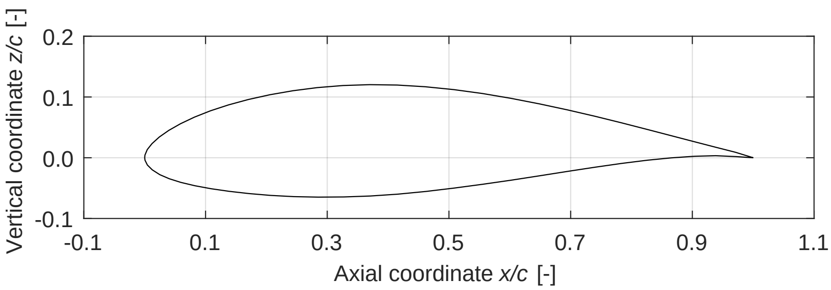

Figure A.2: Plot of the airfoil used during Experiment 2.

Table A.1: Airfoil coordinate table of wings used in the experiments.

MOD22B airfoil (Experiment 1)									
Main element						**Experiment 2 airfoil**			
Upper surface		**Lower surface**		**Flap**		**Upper surface**		**Lower surface**	
x/c [-]	z/c [-]	x/c [-]	z/c [-]	x/c [-]	z/c [-]	x/c [-]	z/c [-]	x/c [-]	z/c [-]
0.8500	0.0354	0.0000	0.0000	1.0000	0.0000	1.0000	0.0000	0.0000	0.0002
0.8063	0.0440	0.0050	-0.0095	0.9719	0.0092	0.9858	-0.0008	0.0020	-0.0080
0.7616	0.0518	0.0063	-0.0111	0.9424	0.0164	0.9549	0.0071	0.0080	-0.0159
0.7208	0.0587	0.0109	-0.0147	0.9100	0.0235	0.9212	0.0160	0.0180	-0.0239
0.6777	0.0657	0.0189	-0.0191	0.8862	0.0280	0.8848	0.0257	0.0320	-0.0314
0.6339	0.0725	0.0368	-0.0256	0.8568	0.0320	0.8459	0.0361	0.0490	-0.0378
0.5901	0.0791	0.0443	-0.0277	0.8275	0.0340	0.8050	0.0471	0.0703	-0.0437
0.5478	0.0850	0.0666	-0.0329	0.7975	0.0320	0.7622	0.0582	0.0951	-0.0490
0.5000	0.0913	0.0877	-0.0369	0.7659	0.0260	0.7179	0.0692	0.1231	-0.0538
0.4624	0.0958	0.1306	-0.0432	0.7488	0.0190	0.6724	0.0796	0.1543	-0.0580
0.4213	0.1000	0.1735	-0.0483	0.7346	0.0115	0.6260	0.0895	0.1884	-0.0616
0.3763	0.1034	0.2143	-0.0522	0.7182	-0.0020	0.5791	0.0984	0.2252	-0.0644
0.3347	0.1050	0.2583	-0.0557	0.7105	-0.0110	0.5320	0.1059	0.2643	-0.0661
0.2927	0.1046	0.3008	-0.0585	0.7072	-0.0160	0.4850	0.1118	0.3055	-0.0666
0.2513	0.1023	0.3434	-0.0607	0.7020	-0.0300	0.4386	0.1159	0.3485	-0.0660
0.2077	0.0978	0.3866	-0.0623	0.7020	-0.0300	0.3930	0.1179	0.3930	-0.0640
0.1654	0.0910	0.4309	-0.0633	0.7061	-0.0386	0.3485	0.1178	0.4386	-0.0605
0.1236	0.0814	0.4704	-0.0636	0.7112	-0.0415	0.3055	0.1156	0.4850	-0.0558
0.0820	0.0677	0.5123	-0.0633	0.7172	-0.0420	0.2643	0.1116	0.5320	-0.0501
0.0610	0.0585	0.5545	-0.0623	0.7335	-0.0385	0.2252	0.1059	0.5791	-0.0439
0.0393	0.0464	0.5989	-0.0599	0.7478	-0.0350	0.1884	0.0989	0.6260	-0.0371
0.0278	0.0385	0.6386	-0.0564	0.7615	-0.0315	0.1543	0.0907	0.6724	-0.0302
0.0169	0.0293	0.6788	-0.0503	0.7923	-0.0240	0.1231	0.0816	0.7179	-0.0234
0.0089	0.0205	0.6950	-0.0470	0.8219	-0.0170	0.0951	0.0717	0.7622	-0.0171
0.0039	0.0129	0.6976	-0.0464	0.8519	-0.0110	0.0703	0.0612	0.8050	-0.0116
0.0022	0.0096	0.6933	-0.0300	0.8808	-0.0060	0.0490	0.0504	0.8459	-0.0073
0.0000	0.0000	0.7027	-0.0135	0.9106	-0.0025	0.0317	0.0396	0.8848	-0.0043
		0.7222	0.0096	0.9403	0.0000	0.0177	0.0287	0.9212	-0.0026
		0.7445	0.0243	0.9634	0.0010	0.0079	0.0185	0.9549	-0.0030
		0.7640	0.0317	1.0000	0.0000	0.0019	0.0091	0.9858	-0.0058
		0.7954	0.0375			0.0000	0.0002	1.0000	0.0000
		0.8500	0.0354						

B
Propeller geometries and section data

Three propellers were simulated and used during experiments. Their geometries and blade section coordinates and polars are shown in this appendix for reference and to reproduce results. The blade chord, pitch and thickness distributions for the three propellers can be found in Figure B.1.

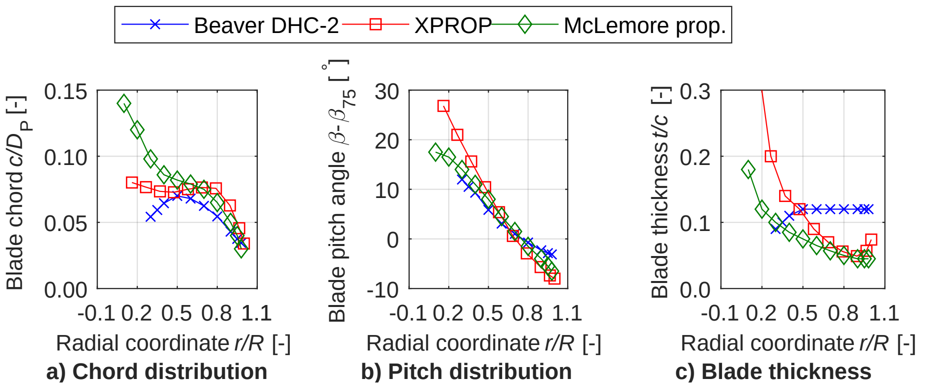

Figure B.1: Blade chord, pitch and thickness distributions of the Beaver DHC-2 propeller, XPROP and McLemore's propeller.

The first propeller is used in Experiment 1, and is a scaled Hamilton Standard 6101 propeller [73]. The propeller uses a NACA64A416/4416MOD airfoil for the whole blade, with exception of the blade root, which has a cylindrical shape. It was unclear what the modification entailed, which is why the numerical model employed a NACA64A416 section. Figure B.2 shows this airfoil shape with corresponding lift and drag curves at a Reynolds number of $2 \cdot 10^5$, produced with XFOIL [62].

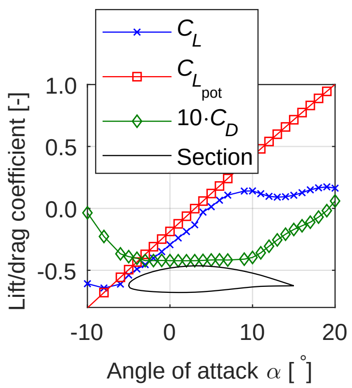

Figure B.2: NACA64A416 airfoil used to model the Hamilton Standard 6101 propeller numerically, with lift and drag curves.

The second propeller in the thesis is a scaled version of the Dowty-Rotol propeller on the Fokker F50, the XPROP. Data on this propeller were available in-house [58]. The propeller uses ARA-D and -A airfoil sections. The eight blade sections used in the numerical model are shown in Figure B.3 with corresponding lift and drag curves at a Reynolds number of $5 \cdot 10^4$, produced with XFOIL [62].

The final propeller, used for the validation of the BEM for propellers at angle of attack, is a 1.62 m diameter propeller designed for a convertible-type airplane. Extensive experimental studies of the performance of this propeller at angle of attack were done by McLemore [66]. Figure B.4 contains its NACA 16-series blade sections and their corresponding polars.

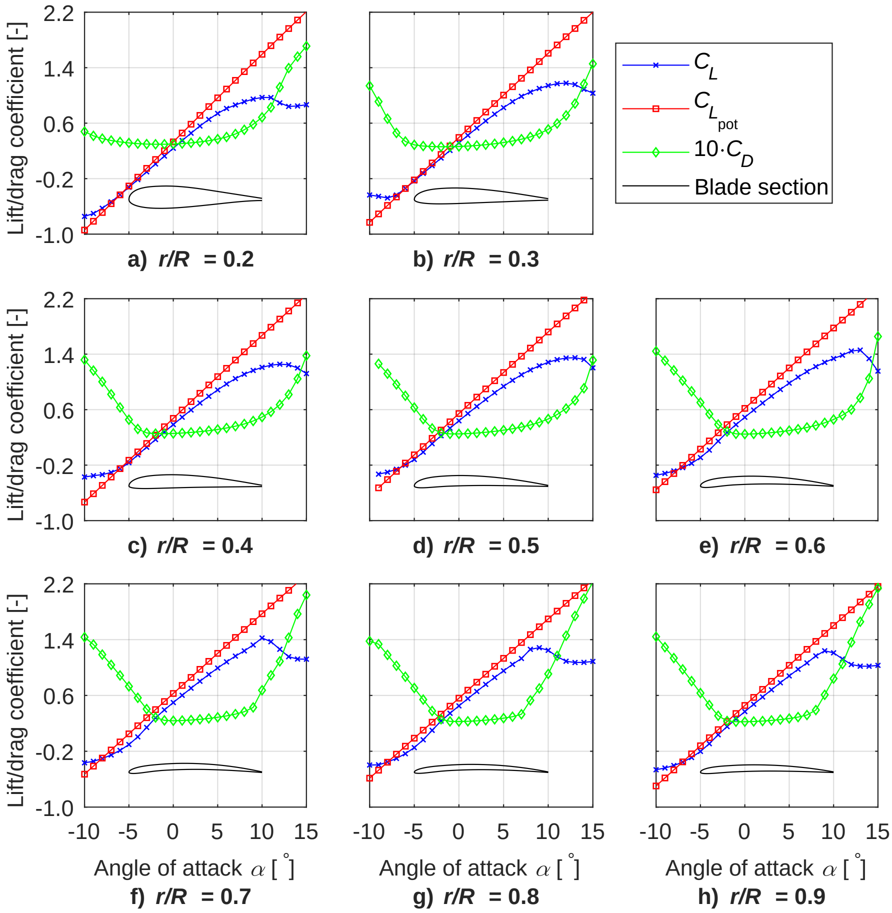

Figure B.3: ARA-D and -A airfoils used to model the XPROP propeller numerically, with lift and drag curves.

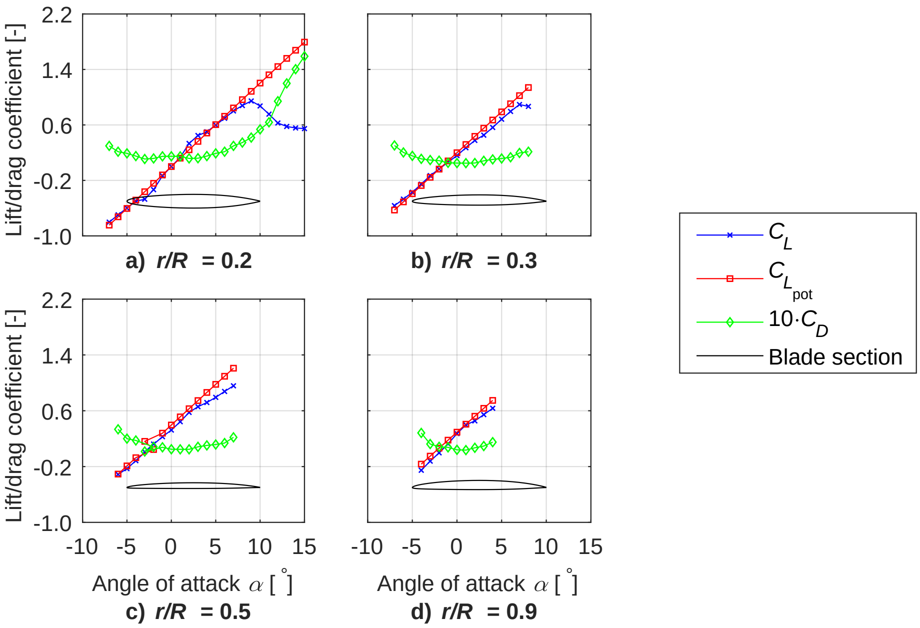

Figure B.4: NACA 16-series airfoils used to model McLemore's propeller numerically, with lift and drag curves.

C

WIND TUNNEL LAYOUT

Figure C.1 contains the cross-section of the Low Turbulence Tunnel that was used during Experiment 1. The layout of the Open Jet Facility used in Experiment 2 is shown in Figure C.2.

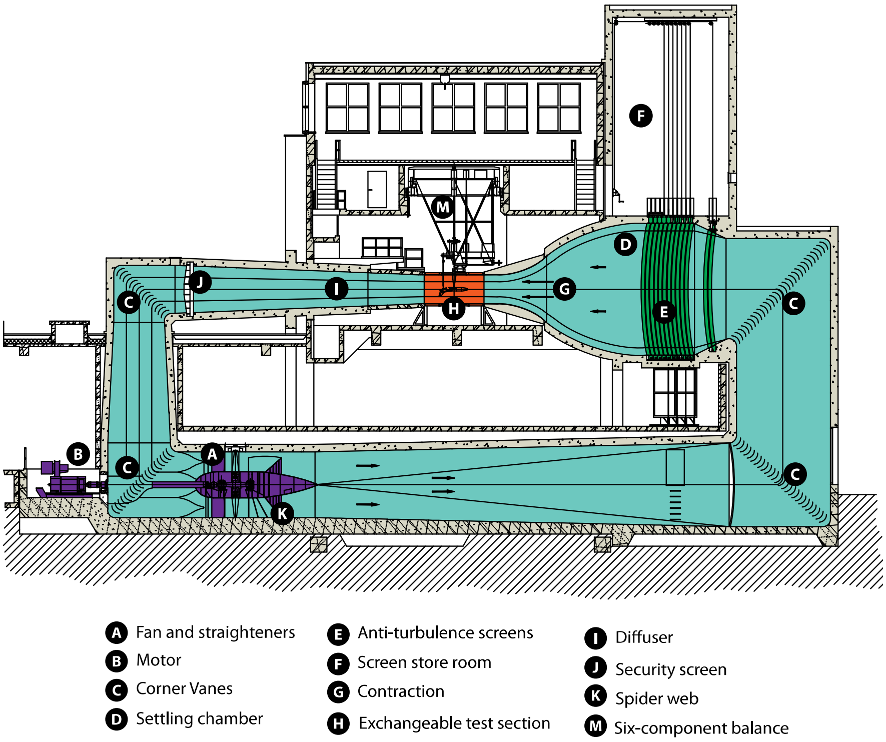

Figure C.1: Low Turbulence Tunnel layout [74].

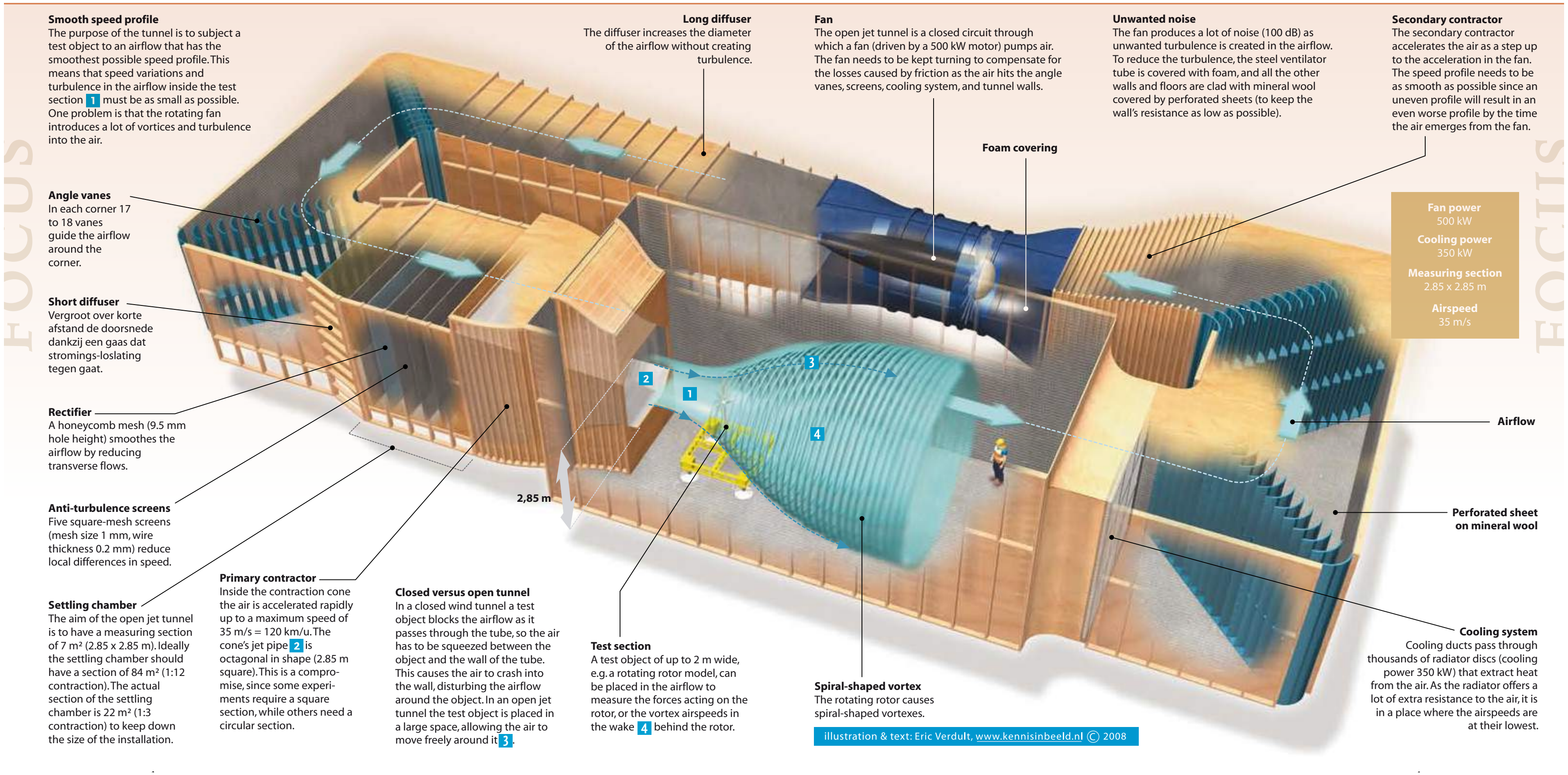

Figure C.2: Open Jet Facility layout [75].

D

WIND TUNNEL CORRECTIONS

The coefficients found during the experimental campaign have been corrected for wind tunnel blockage effects [55]. The sources of the correction factors and their formulae will be presented, but their derivation is omitted for brevity. Firstly, the curvature of the streamlines is changed, for which a streamline curvature coefficient is defined:

$$C_{\mathrm{SC}} = \frac{\sigma_{\mathrm{WT}}}{\beta_1^2}. \tag{D.1}$$

σ_{WT} is a ratio between the wing chord and wind tunnel height, equal to $\frac{\pi^2}{48}(\frac{c}{h})^2$. h is the effective wind tunnel width, i.e. the cross-sectional area divided by the model span, in this case 1.656 m. β_1 is a Mach number correction, equal to $\sqrt{1-M^2}$. Secondly, the wing model is blocking the wind tunnel flow, leading to an increase in effective flow velocity near the wing. Accordingly, a solid blockage factor is used:

$$C_{\mathrm{SB}} = (1 + 1.1\frac{\beta_1}{t/c})\frac{\Lambda\sigma_{\mathrm{WT}}}{\beta_1^3}. \tag{D.2}$$

t is the airfoil thickness and Λ is the body-shape factor:

$$\Lambda = \frac{16}{\pi}\int_0^1 \frac{z}{c}\sqrt{(1-C_p)\big(1+(\frac{dz}{dx})^2\big)}\,d\frac{x}{c} \tag{D.3}$$

in which x and z are the airfoil coordinates and C_p its pressure distribution. In the case of the NLF-MOD22B airfoil, it is equal to 0.3076 or 0.2715 with the flap nested or deflected, respectively. Thirdly, the model wake in the wind tunnel is finite, since it ends at the walls. A wake blockage coefficient is needed to correct for this:

$$C_{\mathrm{WB}} = \frac{c}{4h\beta_1^2}C'_{D_p}(1+0.4M), \tag{D.4}$$

with the prime indicating an uncorrected value.

Subsequently, the corrected lift coefficient can be found:

$$C_L = C'_L\big(1 - C_{\mathrm{SC}} + 5.25C_{\mathrm{SC}}^2 - (2-M^2)(C_{\mathrm{SB}} + C_{\mathrm{WB}})\big). \tag{D.5}$$

The first term is a second-order streamline-curvature correction, whereas the second term corrects for solid and wake blockage. The pitching moment coefficient should only be corrected for streamline curvature, as follows:

$$C_M = C'_M(1 - \frac{C_{\mathrm{SC}}}{4} + 1.05C_{\mathrm{SC}}^2). \tag{D.6}$$

Since the wing is placed in the wind tunnel vertically, a correction for wake buoyancy is also applied to the pressure drag coefficient:

$$C_{D_p} = C'_{D_p}\frac{1-(1+0.4M^2)C_{\mathrm{SB}}}{1-0.2M^2\big((1+C_{\mathrm{SB}}C_{\mathrm{WB}})^2-1\big)^{2.5}(1+C_{\mathrm{SB}}C_{\mathrm{WB}})^2}. \tag{D.7}$$

The numerator contains the wake buoyancy correction, while the denominator carries the second-order wake and solid blockage corrections.

Note that a correction for the propeller should still be added. A propeller generating forward thrust increases the velocities inside its slipstream. In an open test section, the velocities outside the slipstream are generally equal to freestream. In the closed test section, however, mass continuity requires the flow outside the slipstream to decelerate. Garner [55] quantifies the velocity decrease inside the slipstream, ΔU as:

$$\Delta U = -U \frac{C_T D_{\mathrm{P}}^2}{2hc\sqrt{1+\frac{8C_T}{\pi J^2}}}. \tag{D.8}$$

It is thus not possible to apply this correction, since the thrust coefficient in the wind tunnel experiment is unknown. However, it will now be shown that the correction is negligible by applying it to the highest thrust setting in the wind tunnel experiment. This is Configuration 2, since this featured the lowest inflow velocities at the propeller disk. At the highest thrust setting, $J = 0.7$, the thrust coefficient of the isolated propeller is 0.12. When placed above the wing, the propeller thrust is reduced, but assuming it is not, evaluating Equation D.8 for the experimental values leads to a velocity decrease smaller than 0.2% of the freestream velocity. Correspondingly, the correction to dynamic pressure is of the order of 0.004% of the freestream dynamic pressure, leading to negligible changes to aerodynamic coefficients.

E

Blade element model corrections

The BEM corrects the blade element lift and drag coefficients for compressibility, three-dimensional effects and root and tip effects. Firstly, the compressibility correction is applied. Since the propeller is rotating at significant speed, the Mach numbers increase toward the blade tips and may significantly exceed the freestream Mach number. Dorfling's compressibility correction [64] is used, and reportedly valid until Mach numbers of 0.9. Empirical relations are used to accounts for the two most significant compressibility effects, an increase in the lift coefficient with Mach number and drag divergence. First, the drag divergence Mach number M_{DD} must be estimated:

$$M_{\mathrm{DD}} = \kappa - \frac{t}{c} - 0.1C_L'. \tag{E.1}$$

κ is a factor related to airfoil shape, which is equal to 0.87 for NACA 6-series and to 0.95 for supercritical airfoils. The thickness ratio t/c and lift coefficient C_L' are the blade element's thickness-to-chord ratio and its uncorrected lift coefficient. This can be used to determine the Mach-number-corrected lift and drag coefficients with empirical formulae. If the local Mach number is lower than the drag divergence Mach number, the lift is corrected to:

$$C_L = C_L' \frac{1}{\sqrt{(1-M^2)}} + \frac{t/c}{1+t/c}\Big(\frac{1}{\sqrt{(1-M^2)}}\big(\frac{1}{\sqrt{(1-M^2)}} - 1\big) + \frac{\gamma+1}{4}\frac{M^4}{1-M^2}\Big). \tag{E.2}$$

γ is the heat capacity ratio, approximately 1.4 for air at room temperature. If the local Mach number is higher than the drag divergence Mach number, lift and drag are corrected for drag divergence:

$$C_L = C_L' \frac{1-M^2}{1-M_{\mathrm{DD}}^2}\Big(\frac{1}{\sqrt{(1-M^2)}} + \frac{t/c}{1+t/c}\Big(\frac{1}{\sqrt{(1-M^2)}}\big(\frac{1}{\sqrt{(1-M^2)}} - 1\big) + \frac{\gamma+1}{4}\frac{M^4}{1-M^2}\Big)\Big), \tag{E.3}$$

and

$$C_D' + 1.1\Big(\frac{M - M_{\mathrm{DD}}}{1-M_{\mathrm{DD}}^2}\Big)^3. \tag{E.4}$$

An example of the resulting correction factors C_L/C_L' and C_D/C_D' are shown in Figure E.1. Until the drag divergence Mach number is reached, lift increases with increasing Mach number. At the drag divergence Mach number, shock waves appear, causing boundary layer separation [67]. This leads to a decrease in lift and steep rise in drag with increasing Mach number.

Subsequently, Prandtl hub and tip loss factors are applied [65]. These account for the finite nature of the blades. At the propeller hub and blade tips, aerodynamic coefficients are generally lower due to the vortices there. The correction factor for both lift and drag coefficients are equal to $\frac{2\cos^{-1}(e^{-f})}{\pi}$, with:

$$f = \begin{cases} \dfrac{B(R-r)}{r\sin\theta}, & \text{if } r > R/2, \\ \dfrac{B(r-R_{\mathrm{hub}})}{r\sin\theta}, & \text{if } r < R/2. \end{cases}$$

Finally, corrections for three-dimensional flow are applied according to Snel [63]. This models radial flow on the propeller blade, leading to the so-called Himmelskamp effect. The boundary layer has a low flow velocity

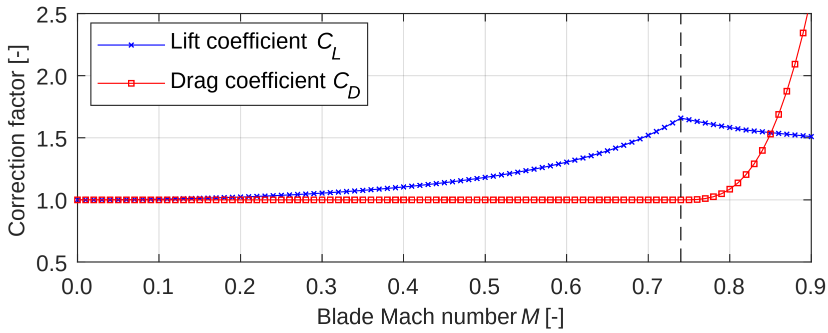

Figure E.1: Dorfling Mach correction factors C_L/C_L' and C_D/C_D' as a function of Mach number. Plots were made for a Beaver propeller section at $r/R = 0.5$, at lift coefficient 0.1. The drag divergence Mach number of this blade section is indicated by a dashed line.

and is thus strongly affected by radial flow on the blades. Radial velocities generally point toward the blade tips due to the centrifugal force, and accordingly sweep the boundary layer outward. This leads to a thinner boundary layer on the inner blade sections, which increases lift, since the boundary layer has a decambering effect on airfoils. Furthermore, stall is postponed. The correction for this is:

$$C_L = C_L' + 3\frac{c^2}{r^2}(C_{L_{\text{pot}}} - C_L), \tag{E.5}$$

in which C_L and $C_{L_{\text{pot}}}$ are the lift and inviscid lift coefficient of the blade section, respectively.

F

SLIPSTREAM MODELS

In the slipstream vortex lattice method, theories by Rwigema [65] and de Young [69] are used. The used equations are briefly described in this appendix, although the reader is referred to the relevant papers for their explanation. Figure F.1 shows the side view of the slipstream path. The propeller is at an angle of attack α_P. At the propeller disk, the slipstream has a radius R, but due to its contraction, the slipstream radius at an axial coordinate x is reduced to:

$$R_\mathrm{s}(x) = R\sqrt{\frac{1+a}{1+s(x)}}. \tag{F.1}$$

$s(x)$ is the axial acceleration factor at the considered axial coordinate, which is equal to:

$$s(x) = a\frac{1+x}{\sqrt{x^2+R^2}}. \tag{F.2}$$

In the slipstream VLM in this thesis, these equations are used for every blade element, with corresponding axial acceleration factor, leading to a dependence of the slipstream radius and acceleration on the radial and azimuthal position. This is not fully accurate, since it neglects any interaction between slipstream segments. However, it is a necessary approximation to limit the complexity of the modelling of the slipstream.

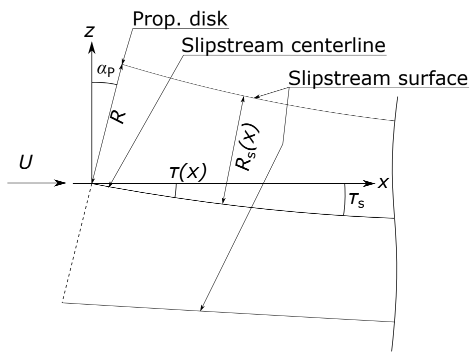

Figure F.1: Generic sketch of the side view of the slipstream.

Furthermore, if the propeller is at an angle of attack, the slipstream centerline will follow a curved path in the (x,z)-plane. At the propeller disk, its angle with respect to the x-axis is α_P. Downstream, the slipstream has fully developed, leading to a static angle τ_s w.r.t. the x-axis, but closer behind the propeller disk, this angle, $\tau(x)$, is dependent on the axial location. De Young found experimentally that the slipstream has generally fully developed at $x = D_\mathrm{P}$, and furthermore that the angle varies linearly, i.e.:

$$\tau(x) = \tau_\mathrm{s} + (\alpha_\mathrm{P} - \tau_\mathrm{s})(\frac{D_\mathrm{P} - x_\mathrm{P}}{x + D_\mathrm{P}}). \tag{F.3}$$

Moreover, he found an empirical relation to calculate the developed slipstream angle:

$$\tau_\mathrm{s} = \alpha_\mathrm{P}\Big(1.06\frac{\sigma_\mathrm{e}}{1+2\sigma_\mathrm{e}}\sin(\beta_{75}+0.052)\sqrt{1+T_{C_\mathrm{DY}}}\frac{2T_{C_\mathrm{DY}}+3+\sqrt{T_{C_\mathrm{DY}}}}{(2+T_{C_\mathrm{DY}})^2}+\frac{1+T_{C_\mathrm{DY}}-\sqrt{T_{C_\mathrm{DY}}}}{2+T_{C_\mathrm{DY}}+1}\Big). \tag{F.4}$$

This formula contains de Youngs thrust coefficient $T_{C_\mathrm{DY}} = \frac{8C_T}{\pi J^2}$ and the effective blade solidity $\sigma_\mathrm{e} = 0.0356B\frac{\bar{c}_\mathrm{b}}{R}\bar{c}_{l_\alpha}$ based on the mean blade chord $\bar{c}_\mathrm{b}$ and section lift gradient $\bar{c}_{l_\alpha}$. Veldhuis [18] reported that within certain operational limits (most notably, $\alpha_\mathrm{P} < 20°$ and low to moderate loading), typical errors of this method are within ±15%.

G
CODE LISTING

The following pages contain the MATLAB code listing of the various modules to run the numerical simulation described in this thesis. The code is run by the main file shown in Figure G.1. The panel method programme can be seen in Figures G.2 to G.5. Note that the full code to generate the FASD input file has been slightly abbreviated, for a full description the reader is referred to FASD's user manual. The blade element model is in Figures G.6 to G.9. Finally, the slipstream vortex lattice method is presented in Figures G.10 to G.13.

```
D:\Documents\Uni\TU_Delft\Thesis\Program ...\MAIN.m        Page 1

%% The main file to run an over-the-wing propeller simulation
close all

disp('Starting propeller-wing simulation (ITERATION 1)');
iter = 1; tic; INPUT;      %Initialize iteration count, clock and load input
runFASD; runPropBEM; runPropSlip;  %First run to start iteration

% Read and store Wing+nacelle pressure data
[~,~,~, CpN, cl1, cd1, cm1] = getCp(1);

% Calculate residuals
rmsW = (sum(sum((Vwi(:, :, 4:end) - Vwi1).^2))...
    /length(Vwi)/size(Vwi, 2)).^0.5;
rmsP = (sum(sum((Vpi(:, :, 4:end) - Vpi1).^2))...
    /length(Vpi)/size(Vpi, 2)).^0.5;

% Iterate until residuals are within tolerance
while any(rmsW(end, :) > tol) || any(rmsP(end, :) > tol)

    % Store old induced velocities for convergence check
    Vwi1 = Vwi(:, :, 4:end);
    Vpi1 = Vpi(:, :, 4:end);

    iter = iter +1;          % Increase iteration counter
    disp(['ITERATION ', num2str(iter), ' beginning']);

    if iter > iter_max       % Stop iterating at max number of iterations
        disp('Maximum iteration counter exceeded');
        break
    else
        runFASD; runPropBEM; runPropSlip;    % New iteration

        % Calculate residuals
        rmsW = [rmsW; (sum(sum((Vwi(:, :, 4:end) - Vwi1).^2))...
            /length(Vwi)/size(Vwi, 2)).^0.5];
        rmsP = [rmsP; (sum(sum((Vpi(:, :, 4:end) - Vpi1).^2))...
            /length(Vpi)/size(Vpi, 2)).^0.5];
    end

    % Plot residuals
    subplot(2,1,2)
    plot(1:iter, rmsW(:,1), 1:iter, rmsW(:,2), 1:iter, rmsW(:,3),...
        1:iter, rmsP(:,1), 1:iter, rmsP(:,2), 1:iter, rmsP(:,3));
    pause(0.01)
end

disp('Propeller-wing simulation has converged (COMPLETE)');

% Read converged wing pressure data
[~, ~, ~, Cp, cl, cd, cm] = getCp(1);
```

Figure G.1: Code to run over-the-wing propeller simulations.

D:\Documents\Uni\TU_Delft\Thesis\Progr...\runFASD.m Page 1

```
%% This module runs the panel method FASD

fid = fopen('.\FASD\PropWing.geo', 'w');     % Write input file
ntp = round(2*yp/dp);                        % Spanwise panel spacing under prop

% Initialize or interpolate propeller-induced velocities at wing.
if iter == 1     % First iteration with nacelle or propeller

    % Initialize interpolated propeller-induced velocity matrix
    Vpii = zeros(length(foil), length(y_si), 6);

    % Store interpolated propeller-induced velocity coordinates
    for i = 1:length(y_si)
        Vpii(:,i,1:3) = [foil(:,1), y_si(i)*ones(length(foil), 1),...
            foil(:,2)];
    end
elseif iter > 1 % Later iterations

    % Clear hub and tip radii when not starting first iteration
    r = r(2:end-1);

    % Interpolate propeller-induced velocities to requested span positions
    for i = 4:6
        Vpii(:,:,i) = interp1(y_s, Vpi(:,:,i)', y_si, 'makima')';
    end
end

theta = 0:2*pi/n_theta:2*pi*(1-1/n_theta);  % list of azimuthal coordinates

% Find leading edge and divide airfoil into lower and uper surface
iLE = find(foil(:,1) == 0); [~, IA, ~] = unique(foil(:,1));
foilu = flip(foil(IA <= iLE, :));
foill = foil(iLE:end, :);

% Propeller disc center coordinates
co_p = [xp*cref + (R + d)*sin(a_p), 0,... %x, y
    interp1(foilu(:,1), foilu(:,2), xp*cref*cos(a_w)) + (R + d)*cos(a_p)]; %z

%% Write contents to the FASD input file (see FASD's manual for details)

% Configuration data
fprintf(fid, '%s\n',...
    '#1.1 The first two lines are general identification lines');
fprintf(fid, '%s\n','''This is a wing''');
fprintf(fid, '%s\n','#1.2 Further identification');
fprintf(fid, '%s\n','''in a propeller-wing simulation''');
fprintf(fid, '%s\n','#1.3 NPART   Configuration Id');
if iter == -1
    fprintf(fid, '\t\t%s\n','1      ''Wing''');
else
    fprintf(fid, '\t\t%s\n','2      ''Wing''');
end
fprintf(fid, '%s\n','#1.4 IREF');
```

Figure G.2: First page of the code to run the panel method.

```
D:\Documents\Uni\TU_Delft\Thesis\Progr...\runFASD.m        Page 2

fprintf(fid, '\t\t%s\n','1');
fprintf(fid, '%s\n', '#(1.5) Xmom      Ymom     Zmom     Cref     Aref');
fprintf(fid, '\t \t %i \t\t %i \t\t %i \t\t %f \t %f\n',...
    [0.25*cref*cos(a_w) 0 -0.25*cref*sin(a_w) cref Aref/1000]);

% Part data (wing)
fprintf(fid, '%s\n','#2.1 NSEGM    Part Id');
fprintf(fid, '\t\t%i\t\t%s\n',[5  '''Wing''']);
fprintf(fid, '%s\n','#2.2 IREFP    ITRAN');
fprintf(fid, '\t\t%i\t\t%i\n',[0 0]);

% Segment data (reference area under prop)
y_sc = y_si(y_si <= yp & y_si >= -yp);
fprintf(fid, '%s\n','#3.1 NSCUR      NSBRK      NSECT    Segment Id');
fprintf(fid, '\t\t%i\t\t%i\t\t%i\t\t%s\n',...
    [length(y_sc) 0 0    '''UnderProp''']);
fprintf(fid, '%s\n','#3.2 IREFS      ITRAN');
fprintf(fid, '\t\t%i\t\t%i\n',[0 0]);
fprintf(fid, '%s\n','#3.7 ISEGT      ISIDE');
fprintf(fid, '\t\t%i\t\t%i\n',[1 1]);
fprintf(fid, '%s\n','#3.8 IPRES      IFORC');
fprintf(fid, '\t\t%i\t\t%i\n',[0 1]);
fprintf(fid, '%s\n','#3.9   S=0        S=1        T=0        T=1');
fprintf(fid, '\t\t%i\t\t%i\t\t%i\t\t%i\n',[0 0 0 0]);
fprintf(fid, '%s\n','#3.10IWAKE      IEDG1      IEDGN');
fprintf(fid, '\t\t%i\t\t%i\t\t%i\n',[1 0 0]);
fprintf(fid, '%s\n','#3.11ICAMB      ITHKN      ISLST      IOUTF');
if iter < 2
    fprintf(fid, '\t\t%i\t\t%i\t\t%i\t\t%i\n',[0 0 0 0]);
else
    fprintf(fid, '\t\t%i\t\t%i\t\t%i\t\t%i\n',[0 0 1 0]);
end
fprintf(fid, '%s\n','#3.12NSPAN      ISPAR      ISDIS');
fprintf(fid, '\t\t%i\t\t%i\t\t%i\n',[length(foil)-1 1 0]);
fprintf(fid, '%s\n','#3.14NTPAN      ITPAR      ITDIS');
fprintf(fid, '\t\t%i\t\t%i\t\t%i\n',[length(y_sc) 1 0]);
fprintf(fid, '%s\n','#(3.16)NTRPN    ITRDS');
fprintf(fid, '\t\t%i\t\t%i\n',[ntp 1]);

%Curve data (under prop)
for i = 1:length(y_sc)
    fprintf(fid, '%s\n','#4.1 NPNTC ITRNC    ITYPC    IGENC');
    fprintf(fid, '\t\t%i\t\t%s\n',[length(foil) '0       0       0']);
    fprintf(fid, '%s\n','#(4.6a)        X            Y          Z');
    for j = 1:length(foil)
        fprintf(fid, '\t\t%f\t\t%f\t\t%f\n',[foil(j,1) y_sc(i) foil(j,2)]);
    end
    if iter > 1
        fprintf(fid, '%s\n','#(4.7a)       U            V          W       E');
        for j = 1:length(foil)
            ii = i + sum(y_si<-yp);
            fprintf(fid, '\t\t%g\t\t%g\t\t%g\t\t%g\n',...
                [Vpii(j,ii,4) Vpii(j,ii,5) Vpii(j,ii,6) ...
```

Figure G.3: Second page of the code to run the panel method.

D:\Documents\Uni\TU_Delft\Thesis\Progr...\runFASD.m Page 3

```
                sum(Vpii(j,ii,4:end).^2)]);
        end
    end
end

% Specification of the other segments is omitted for brevity,
% the interested reader is referred to the FASD manual

%% Run FASD and read inflow to propeller disc
cd FASD
system('fasd2.exe > NUL');
cd(fileparts(pwd))

% Find propeller disc inflow velocities
fid = fopen('.\FASD\PropWing.res'); % Open results file

% Go to inflow plane pressure lines
line = fgetl(fid);
while not(endsWith(line, 'PropPlane                       '))
    line = fgetl(fid);
end
line = fgetl(fid);
while not(endsWith(line, 'Cp'))
    line = fgetl(fid);
end
line = fgetl(fid);

% Read inflow plane velocities
Vwi = zeros(n_sec, n_theta, 6); % Initialize
for i = 1:n_sec
    for j = 1:n_theta
        Cpline = strsplit(line);
        Vwi(i, j, :) = [str2double(cell2mat(Cpline(5))),...
            str2double(cell2mat(Cpline(6))), ...
            str2double(cell2mat(Cpline(7))),...
            str2double(cell2mat(Cpline(10))) - 1, ...
            str2double(cell2mat(Cpline(11))),...
            str2double(cell2mat(Cpline(12)))];
        line = fgetl(fid);
    end
end

% Similarly for slipstream plane
line = fgetl(fid);
while not(endsWith(line, 'Cp'))
    line = fgetl(fid);
end
line = fgetl(fid);
Vwis = zeros(3*n_sec+1, round(d_s(end)/0.08)+1, 6); % Initialize
for j = 1:size(Vwis, 2)
    for i = 1:size(Vwis, 1)
        Cpline = strsplit(line);
        Vwis(i, j, :) = [str2double(cell2mat(Cpline(5))),...
```

Figure G.4: Third page of the code to run the panel method.

D:\Documents\Uni\TU_Delft\Thesis\Progr...\runFASD.m Page 4

```
            str2double(cell2mat(Cpline(6))), ...
            str2double(cell2mat(Cpline(7))),...
            str2double(cell2mat(Cpline(10))) - 1, ...
            str2double(cell2mat(Cpline(11))),...
            str2double(cell2mat(Cpline(12)))];
        line = fgetl(fid);
    end
end
fclose(fid);

disp('Finished panel simulation of wing (1/3)')
toc

% Plot propeller disk and sliptream plane velocities
figure
if iter > 0
    subplot(2,1,1)
    cquiv(Vwi)
    hold on
    cquiv(Vwis)
    axis equal
end
pause(0.01)

% Initialize previous-iteration velocity matrices for residuals at first iteration
if iter == 1
    Vwi1 = zeros(n_sec, n_theta, 3);
    Vpi1 = zeros(length(foil), length(y_s), 3);
end
```

Figure G.5: Fourth page of the code to run the panel method.

```
D:\Documents\Uni\TU_Delft\Thesis\Pr...\runPropBEM.m       Page 1

%% Module for the blade element method

%Initialize output
T = 0; P = 0; Q = 0; % Thrust/Power/Torque

% Preallocate unsteady solutions
T_u = zeros(1, length(theta)); Q_u = T_u; N_u = T_u; Y_u = T_u;

% Preallocate distributions for slipstream VLM and output
aa = zeros(length(theta), length(r)); G = aa; a_eff = aa; ub = aa;
Vin = aa; dCp = aa;

% Loop over azimuthal stations
for m = 1:length(theta)

    %Loop over each radial blade element
    for i = 1:n_sec
        beta = p0 + pb(i); %calculate local blade element setting angle

        % local blade element coordinate
        co_sec= [co_p(1) + sin(theta(m))*r(i)*sin(a_p),... %x
            co_p(2) + cos(theta(m))*r(i), ... %y
            co_p(3) + sin(theta(m))*r(i)*cos(a_p)]; %z

        %guess initial values of inflow and swirl factor
        a = 0.1;
        b = 0.01;

        finished = false; %set logical variable to control iteration

        %set iteration count and check flag
        count = 1;
        itercheck = 0;

        % Iterate until converged
        while (~finished)
            %axial blade element velocity (Va)
            V0 = U*((1 +...                   % Freestream
                + Vwi(i, m,4))*cos(a_p) ... %Wing-induced x-comp. projected onto
prop. axis
                - Vwi(i, m,6)*sin(a_p))*...%z-comp. projected onto prop. axis
                (1+a);                      % Axial induction
            %tangential blade element velocity (Vt)
            V2 = (2*pi*n*r(i)...                     %Prop. rotational velocity
                + U*((((1 + Vwi(i, m,4))*sin(a_p) ...%Wing-induced x-comp. projected
onto prop. plane
                + Vwi(i, m,6)*cos(a_p)) ...          %z-comp. projected onto prop.
plane
                *cos(theta(m))) ...                  %Projected onto blade
                - Vwi(i, m,5)*sin(theta(m))))*...    %y-component projected onto
blade
                (1-b);                               % Tangential induction factor
```

Figure G.6: First page of the code to run the blade element method.

D:\Documents\Uni\TU_Delft\Thesis\Pr...\runPropBEM.m Page 2

```
%Effective flow angle of attack
a_eff(m,i) = atan2(Vwi(i, m,6), 1+Vwi(i, m,4));

%flow and blade angle of attack
phi = atan2(V0,V2);
alpha = beta-phi;

%lift and drag coefficients
cl = interp1(polars(:,1)*pi/180, polars(:,2),...
    alpha, 'linear', 'extrap');
cd = interp1(polars(:,1)*pi/180, polars(:,3),...
    alpha, 'linear', 'extrap');

%Check if within blade polar
if alpha <= min(polars(:,1)*pi/180) ||...
        alpha >= max(polars(:,1)*pi/180)
    disp('Blade polar exceeded, lift and drag extrapolated')
end

% Dorfling 2016 compressibility corrections
Vlocal = sqrt(V0*V0+V2*V2);            %local velocity at blade
M = Vlocal/331.3/(1+Temp/273.15)^0.5;  % Mach no.
Mf = (1-M^2)^-0.5;                     % Mach number factor
cl = cl*(Mf + tc(i)/(1+tc(i))*...
    ((Mf*(Mf-1)) + 0.25*2.4*(Mf^2-1)^2)); % Corrected lift
MDD = kappa - tc(i) - cl/10;         % drag divergence Mach no.
if M >= MDD                        % Drag divergence corrections
    cl = cl*(1-M^2)/(1-MDD^2);
    cd = cd + 1.1*((M-MDD)/(1-MDD))^3;
end

% Check if M < 0.9 and display warning if so
if M > 0.9
    disp('Exceeded max. Mach number (0.9)')
end

% Inviscid lift coefficient
clpot = interp1(polars(:,1)*pi/180, polars(:,end),...
    alpha, 'linear', 'extrap');

%Prandtl blade end loss factors
if r(i) >= 0.75*R            %Close to tip
    f = max([B/2*(R-r(i))/r(i)/sin(phi), 0]);
elseif r(i) < 0.5*R          %Close to hub
    f = max([B/2*(r(i)-Rhub)/r(i)/sin(phi), 0]);
    cl = clroot + (cl-clroot)*(r(i)-Rhub)/(0.5*R-Rhub);
    cd = cdroot + (cd-cdroot)*(r(i)-Rhub)/(0.5*R-Rhub);
    clpot = clroot + (clpot-clroot)*(r(i)-Rhub)/(0.5*R-Rhub);
else
    f = Inf;
end
F = 2/pi*acos(exp(-f));      % Blade end loss factors
```

Figure G.7: Second page of the code to run the blade element method.

```
D:\Documents\Uni\TU_Delft\Thesis\Pr...\runPropBEM.m        Page 3

            %Correct drag and lift for 3D(Snel 1993)
            cl = cl + 3*(c(i)/r(i))^2*(clpot - cl);

            %Thrust grading
            DtDr = F*0.5*rho*Vlocal*Vlocal*B*c(i)*(cl*cos(phi)-cd*sin(phi));
            %Torque grading
            DqDr = F*0.5*rho*Vlocal*Vlocal*B*c(i)*r(i)*(cd*cos(phi)+cl*sin(phi));

            %Derive new inflow and swirl factors
            a1 = DtDr/(4.0*pi*r(i)*rho*U*U*(1+a));
            b1 = DqDr/(4.0*pi*r(i)*r(i)*r(i)*rho*U*(1+a)*2*pi*n);

            %stabilize iteration
            a1 = 0.5*(a+a1);
            b1 = 0.5*(b+b1);

            %check for convergence
            if (abs(a1-a)<1.0e-5)
                if (abs(b1-b)<1.0e-5)
                    finished = true;
                end
            end
            a = a1;
            b = b1;
            %increment iteration count
            count = count+1;
            %check to see if iteration stuck
            if (count>500)
                finished = true;
                itercheck = 1;
            end
        end

        % Unsteady loadings
        T_u(m) = T_u(m)+DtDr*dr(i);                         % Thrust
        Q_u(m) = Q_u(m)+DqDr*dr(i);                         % Torque
        N_u(m) = N_u(m)+DqDr*dr(i)/r(i)*cos(theta(m));     % Normal force
        Y_u(m) = Y_u(m)+DqDr*dr(i)/r(i)*sin(theta(m));     % Side force

        % Calculate pressure differential on blade element
        if i == 1
            r1 = Rhub; r2 = 0.5*(r(i)+r(i+1));
        elseif i == n_sec
            r1 = 0.5*(r(i)+r(i-1)); r2 = R;
        else
            r1 = 0.5*(r(i)+r(i-1)); r2 = 0.5*(r(i)+r(i+1));
        end
        ds = pi*(r2^2 -r1^2);
        dCp(m,i) = DtDr*dr(i)/ds/0.5/rho/U^2;

        % Blade circulation and axially induced velocities by prop for VLM
        G(m, i) = 0.5*Vlocal*c(i)*cl*F;
        aa(m, i) = a;
```

Figure G.8: Third page of the code to run the blade element method.

```
D:\Documents\Uni\TU_Delft\Thesis\Pr...\runPropBEM.m        Page 4

        Vin(m, i) = V0/(1+a);
        ub(m, i) = V2/r(i);
    end
end

% Calculate output coefficients
t = mean(T_u)/(rho*n^2*D^4);     % Thrust
q = mean(Q_u)/(rho*n^2*D^5);     % Torque
nf = mean(N_u)/(rho*n^2*D^4);    % Normal force
y = mean(Y_u)/(rho*n^2*D^4);     % Side force
p = 2*pi*q;                      % Power
eff = J*t/p;                     % Efficiency
Jeff = mean(mean(Vin))/n/D;      % Mean effective advance ratio

% Extrapolate to hub and tip
aa = [zeros(length(aa), 1), aa, zeros(length(aa), 1)];
Vin = [zeros(length(Vin), 1), Vin, zeros(length(Vin), 1)];
ub = [zeros(length(ub), 1), ub, zeros(length(ub), 1)];
G = [zeros(length(G), 1), G, zeros(length(G), 1)];
dCp = [zeros(size(dCp, 1), 1), dCp, zeros(size(dCp, 1), 1)];
for m = 1:length(theta)
    aa(m,1) = interp1(r, aa(m,2:end-1), Rhub, 'spline');
    aa(m,end) = interp1(r, aa(m,2:end-1), R, 'spline');
    Vin(m,1) = interp1(r, Vin(m,2:end-1), Rhub, 'spline');
    Vin(m,end) = interp1(r, Vin(m,2:end-1), R, 'spline');
    ub(m,1) = interp1(r, ub(m,2:end-1), Rhub, 'spline');
    ub(m,end) = interp1(r, ub(m,2:end-1), R, 'spline');
end
r = [Rhub, r, R];

disp('Finished BEM analysis (2/3)')
toc
```

Figure G.9: Fourth page of the code to run the blade element method.

D:\Documents\Uni\TU_Delft\Thesis\P...\runPropSlip.m Page 1

```
%% Module for the slipstream vortex lattice method

TCdy = 8/pi/J^2*t;  % De Young's thrust coeff.
se = 0.0356*B*mean(c)*cla/R; % Effective blade solidity
k_s = (a_p + mean(mean(a_eff)))*(...        % Developed slipstream deflection
    4.25*se/(1+2*se)*sin(p0 + 3*pi/180)*... %  angle (De Young, 1965)
    (1+TCdy)^0.5/4*(3+2*TCdy+(1+TCdy)^0.5)/(2+TCdy)^2 +...
    (1+TCdy-(1+TCdy)^0.5)/(2+TCdy));

% Slipstream centerline coordinates due to propeller inclination
co_s = [d_s' + co_p(1), zeros(length(d_s), 2)];

% Calculate slipstream path angles and deflection due to inclination
angles = k_s + (a_p - k_s)*(1 - d_s/D);
angles(d_s>D) = k_s;
defl = zeros(length(d_s), 1);
for i = 2:length(d_s)
    defl(i) = defl(i-1) - sin(angles(i)).*(d_s(2)-d_s(1));
end

% Move slipstream path
co_s(:,3) = co_s(:,3)+defl+co_p(3);

%% Compute slipstream radii and coordinates
dt = d_s*(1+sin(k_s))/U/(1+max(max(aa))*2);               % Time steps
co_sR = zeros(length(r), length(theta), 7,...    % Preallocate tip vortices
    length(d_s));

% Slipstream plane x,z-coordinates
Xs = (squeeze(Vwis(1,:,1:3))-co_p)...
    *[cos(-a_p) 0 -sin(-a_p); 0 1 0; sin(-a_p) 0 cos(-a_p)]; Xs = Xs(:,1)';
Zs = (squeeze(Vwis(:,1,1:3))-co_p)...
    *[cos(-a_p) 0 -sin(-a_p); 0 1 0; sin(-a_p) 0 cos(-a_p)]; Zs = Zs(:,3);

% Loop over all azimuthal and axial slipstream elements
for i = 1:length(theta)
    for j = 1:length(dt)

        % Determine top and bottom coordinates
        if j == 1 % At disc plane
            % Azimuthal position and circulation of the vortex point
            th = repmat(theta(i), 1, length(r));
            co_sR(:, i, 4, j) = B*G(i, :)/n_theta;

            % Angle of the centerline and blade element radius
            a = angles(j); R_s(:, i, j) = r;

            % Coordinate
            co_sR(:,i,1:3,j) = ...
                [zeros(length(r),1), r'.*cos(th'), r'.*sin(th')]*...
                [cos(a) 0 -sin(a); 0 1 0; sin(a) 0 cos(a)] + co_p;

        else % Add slipstream centerline and contraction vectors
```

Figure G.10: First page of the code to run the slipstream vortex lattice method.

D:\Documents\Uni\TU_Delft\Thesis\P...\runPropSlip.m Page 2

```
% Azimuthal position of the vortex point
th1 = th; % Previous azimuthal position
for k = 1:length(r) % For all radial elements


    co_sR(k, i, 4, j) = B*interp1([theta, 2*pi],...% Circulation
        [G(:, k); G(1, k)], mod(th1(k), 2*pi))/n_theta;
    ubc(k) = interp1([theta, 2*pi],...              % Swirl vel.
        [ub(:,k); ub(1, k)], mod(th1(k), 2*pi));
    Vinc(k) = interp1([theta, 2*pi],...             % Axial vel.
        [Vin(:,k); Vin(1, k)], mod(th1(k), 2*pi));
    aac(k) = interp1([theta, 2*pi],...      % Axial acc. factors
        [aa(:,k); aa(1, k)], mod(th1(k), 2*pi));
end
th = ubc*(dt(j)-dt(j-1)) + th1; % New azimuthal position

% Calculate undeformed sl. radius and s-factor (Rwigema 2010)
xx = co_sR(:,i,1,j-1);
s = aac.*(1 + xx./sqrt(xx.^2 + R^2))';
R_s(:, i, j) = r.*sqrt((1 + aac)./(1 + s));

% Current centerline angle, radii and axial velocities
a = angles(j); Rc = R_s(:, i, j);

% Calculate undeformed coordinates
co_sR(:,i,1:3,j) = ...
    squeeze(co_sR(:,i,1:3,j-1)) + ...% previous coordinates
    ((dt(j)-dt(j-1))*(...                   % Time-stepped
    [(Vinc.*(1+s))', zeros(length(r),2)] + ...% Centerline vec
    (R_s(:,i,j-1)-Rc).*...                  % Contraction vec
    [zeros(length(th),1), cos(th'), sin(th')]) + ...
    r'.*...                                 % Swirl vec
    [zeros(length(th),1), cos(th')-cos(th1'), sin(th')-sin(th1')])*...
    [cos(a) 0 -sin(a); 0 1 0;...
    sin(a) 0 cos(a)];       % Rotated through centerline angle

co_sR2 = (squeeze(co_sR(:,i,1:3,j))-co_p)*...
    [cos(-a_p) 0 -sin(-a_p); 0 1 0; sin(-a_p) 0 cos(-a_p)];

% Add wing-induced movement
co_sR(:,i,1:3,j) = ...
    squeeze(co_sR(:,i,1:3,j))...            % Previous coord.
    + U*(dt(j)-dt(j-1))*...                  % Time-stepped
    [interp2(Xs, Zs, Vwis(:,:,4),...    % Interpolate slippath
    co_sR2(:,1), co_sR2(:,3)),...       % velocities to point
    zeros(length(r), 1),...
    interp2(Xs, Zs, Vwis(:,:,6),...
    co_sR2(:,1), co_sR2(:,3))];

% Check if slipstream is not 'crossing' wing, if it is, increase
for k = 1:length(r)
    if co_sR(k,i,1,j) < foil(end,1)
```

Figure G.11: Second page of the code to run the slipstream vortex lattice method.

D:\Documents\Uni\TU_Delft\Thesis\P...\runPropSlip.m   Page 3

```
                    if co_sR(k,i,3,j) < interp1(foilu(:,1), foilu(:,2),...
                            co_sR(k,i,1,j), 'spline')
                        co_sR(k,i,3,j) = interp1(foilu(:,1), foilu(:,2),...
                            co_sR(k,i,1,j), 'spline');
                    end
                end
            end
        end
    end
end
co_sR = permute(co_sR, [1 2 4 3]);  % Change order
clear co_sB               % Clear in case still stored from other simulation

% Calculate the vortex segment control points and direction vectors
co_sR(2:end-2,:,:,1:3) = ...                % Helical vortex control points
    0.5*(co_sR(3:end-1,:,:,1:3)+co_sR(2:end-2,:,:,1:3));
co_sR(:,:,1:end-1,5:7) =...                 % ... and direction vectors
    co_sR(:,:,2:end,1:3) - co_sR(:,:,1:end-1,1:3);
co_sR(end,:,:,4) =...                       % Remove superfluous helical vortices
    co_sR(end-1,:,:,4); co_sR(end-1, :, :, :) = []; co_sR(:, :, end, :) = [];
co_sB(:,:,:,1:3) =...                       % Radial vortex control points
    0.5*co_sR(1:end-1,:,:,1:3)+0.5*co_sR(2:end,:,:,1:3);
co_sB(:,:,:,5:7) =...                       % ... and direction vectors
    co_sR(2:end,:,:,1:3)-co_sR(1:end-1,:,:,1:3);
co_sR(:,:,:,1:3) =...                       % Move to mid-segment
    co_sR(:,:,:,1:3) + 0.5*co_sR(:,:,:,5:7);

% Compute vortex segment strengths (normalized to counteract stretching)
co_sB(:,:,1,4) = co_sR(2:end,:,1,4);                % Bound vortices on blade
co_sB(:,:,end,4) = -co_sR(2:end,:,end-1,4).*... % Starting vortices
    sqrt(sum(co_sB(:,:,1, 5:7).^2, 4))./sqrt(sum(co_sB(:,:,end, 5:7).^2, 4));
co_sB(:,:,2:end,4) =...                             % Other radial vortices
    (co_sR(2:end, :, 2:end, 4)-co_sR(2:end, :, 1:end-1, 4)).*...
    sqrt(sum(co_sB(:,:,1, 5:7).^2, 4))./sqrt(sum(co_sB(:,:,2:end, 5:7).^2, 4));
co_sR(1,:,:,4) = - co_sB(1,:,:,4);                  % Hub helical vortices
co_sR(end,:,:,4) = co_sB(end,:,:,4);                % Tip helical vortices
co_sR(2:end-1,:,:,4) =...                           % Other helical vortices
    co_sB(1:end-1,:,:,4) - co_sB(2:end,:,:,4);

% Helical vortices are overlaying and need to be summed
for j = 2:size(co_sR, 3)
    co_sR(:,:,j,4) = co_sR(:,:,j,4) + co_sR(:,:,j-1,4);
end

% Calculate slipstream-induced velocities at requested points
if iter == 1
    Vpi = zeros(length(foil), length(y_s), 6);
    for i = 1:length(y_s)
        Vpi(:,i,1:3) = [foil(:,1), y_s(i)*ones(length(foil), 1), foil(:,2)];
    end
end

Vpi = VpiCalc(Vpi, co_sR, co_sB, Rvor); % Calculate prop-induced velocities
```

Figure G.12: Third page of the code to run the slipstream vortex lattice method.

D:\Documents\Uni\TU_Delft\Thesis\P...\runPropSlip.m Page 4

```
Vpi(:,:,4:end) = Vpi(:,:,4:end)/U; % Normalize by freestream velocity

disp('Finished slipstream calculation (3/3)')
toc

if iter == 0
    figure
end
hold on
cquiv(Vpi(:, 2:end-1, :))

%% Calculates propeller-induced velocities at requested points
function Vpi = VpiCalc(Vpi, co_sR, co_sB)
for i = 1:size(Vpi,1)     % Loop over airfoil coordinates
    for j = 1:size(Vpi,2) % Loop over spanwise stations
        p_c = [Vpi(i, j,1); Vpi(i,j, 2); Vpi(i,j, 3)];

        for m = 1:size(co_sR, 2)          % Loop around azimuthal stations
            for o = 1:size(co_sR, 1)      % Loop around radial stations
                for l = 1:size(co_sR, 3) % Loop around axial stations
                    % Compute contribution of the tip vortex
                    rvec = p_c...         % r-vector from the vortex to Pq
                        - [co_sR(o,m,l,1); co_sR(o,m,l,2); co_sR(o,m,l,3)];
                    rr = sqrt(sum(rvec.^2));       % r-vector length
                    Vpi(i,j,4:end) = ...           % Biot-Savart
                        [Vpi(i,j,4); Vpi(i,j,5); Vpi(i,j,end)] + ...
                        co_sR(o, m, l, 4)/4/pi*...
                        cross([co_sR(o,m,l,5); co_sR(o,m,l,6);...
                        co_sR(o,m,l,7)], rvec) ...
                        /rr^3;

                    % Compute contribution of the radial vortex
                    if not(o == size(co_sR, 1))
                        rvec = p_c...
                            - [co_sB(o,m,l,1); co_sB(o,m,l,2); co_sB(o,m,l,3)];
                        rr = sqrt(sum(rvec.^2));
                        Vpi(i,j,4:end) =...% Biot-Savart
                            [Vpi(i,j,4); Vpi(i,j,5); Vpi(i,j,end)] + ...
                            co_sB(o, m, l, 4)/4/pi*...
                            cross([co_sB(o,m,l,5); co_sB(o,m,l,6); ...
                            co_sB(o,m,l,7)], rvec) ...
                            /rr^3;
                    end
                end
            end
        end
    end
end
end
```

Figure G.13: Fourth page of the code to run the slipstream vortex lattice method.